LBL-11513 c.2

Lawrence Berkeley Laboratory
UNIVERSITY OF CALIFORNIA

Physics, Computer Science & Mathematics Division

INCLUSIVE D MESON PRODUCTION WITH THE MARK II DETECTOR AT SPEAR

Mark Wayne Coles
(Ph.D. thesis)

September 1980

RECEIVED
LAWRENCE
BERKELEY LABORATORY

NOV 6 1980

LIBRARY AND
DOCUMENTS SECTION

TWO-WEEK LOAN COPY

This is a Library Circulating Copy which may be borrowed for two weeks. For a personal retention copy, call Tech. Info. Division, Ext. 6782.

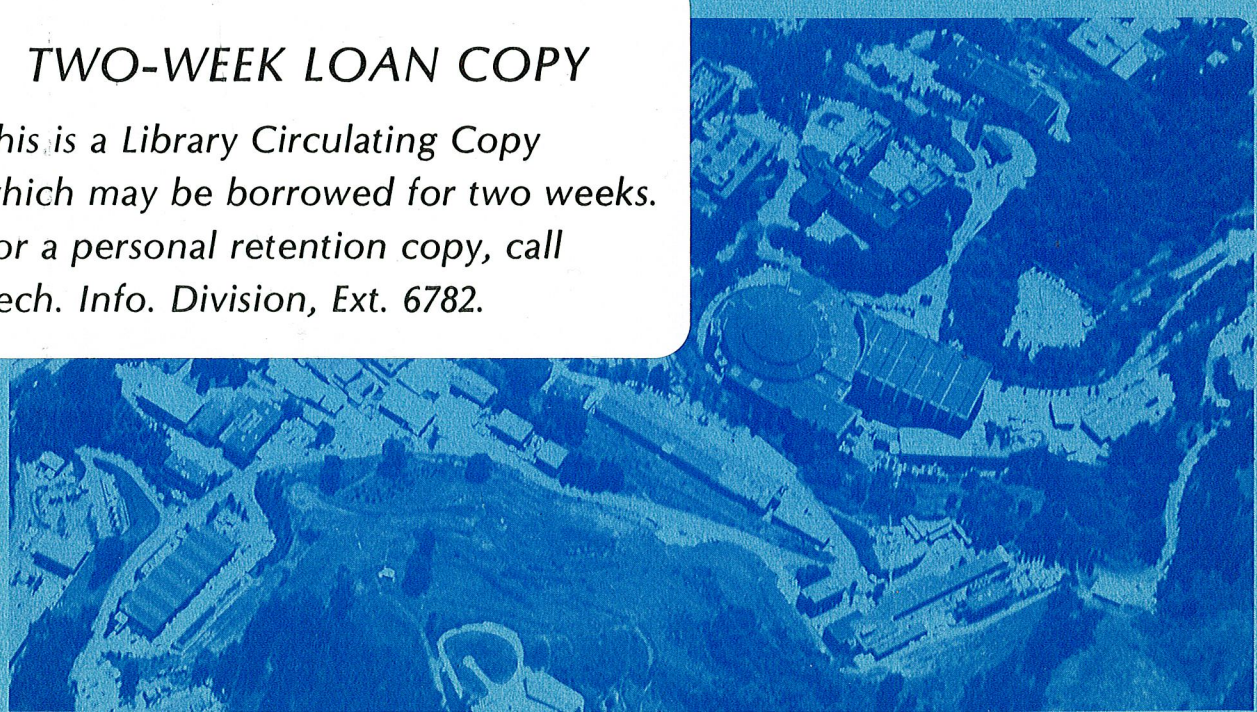

Prepared for the U.S. Department of Energy under Contract W-7405-ENG-48

LBL-11513 c.2

LBL-11513

INCLUSIVE D MESON PRODUCTION WITH THE MARK II DETECTOR AT SPEAR

Mark Wayne Coles

Ph.D. thesis

Physics Division
Lawrence Berkeley Laboratory
University of California
Berkeley, CA 94720

September 1980

Prepared for the U.S. Department of Energy under Contract
W-7405-ENG-48

ABSTRACT

Neutral and charged D meson production cross sections were measured at center of mass energies between 3.9 GeV and 7.4 GeV. The quantity R_D $(=[\sigma_{D^+ + D^-} + \sigma_{D^0 + \bar{D}^0}]/2\sigma_{\mu^+\mu^-})$ is equal to 2 at 4 GeV and 4.4 GeV and about equal to 1 elsewhere. $R_D + 2.5$ approximately equals R $(\sigma_{hadrons}/\sigma_{\mu^+\mu^-})$ at all energies.

The exclusive cross sections for e^+e^- annihilation into $D\bar{D}$, $D^*\bar{D}$, and $D^*\bar{D}^*$ were measured at center of mass energies between 3.9 GeV and 4.3 GeV. $\sigma_{D^*\bar{D}^*}$ decreases with increasing center of mass energy from 6.6±1.3 nb near 4 GeV to 3.6±.9 nb near 4.3 GeV. $\sigma_{D^*\bar{D}}$ also decreases from 4.2±.9 nb to 1.8±.6 nb over the same energy region. $\sigma_{D\bar{D}}$ is less than 0.5±.3 nb at all energies.

The branching fractions for D^{*+} and D^* decay were measured. $B_{D^{*0}\to D^0\pi^0} = 0.5 \pm .09$, $B_{D^{*+}\to D^0\pi^+} = 0.44 \pm .10$, and $B_{D^{*+}\to D^+\pi^0} = 0.31 \pm .07$.

At 5.2 GeV, the D meson differential cross section is well described by phase space for $e^+e^- \to D\bar{D}\pi\pi$ or $D^*\bar{D}^*\pi\pi$. $Sd\sigma/dz$ was parameterized as $A(1-z)^n$ with $n = 0.9\pm.4$. Quasi-two-body production accounts for less than 20% of the total D cross section.

No evidence was found for associated charmed baryon-D meson production. An upper limit of 0.4 nb (90% confidence level) was determined for associated production.

I wish to acknowledge the Mark II collaboration who made this thesis possible. In particular, Dr. George Gidal deserves special thanks for his many useful suggestions and for his encouragement. Also I wish to thank my advisor, Professor Willy Chinowsky, for allowing me to be a part of the Mark II and also for the feedom to pursue other academic interests in addition to physics.

Thanks also to Professor Gilbert Shapiro and Dr. Ernest Koenigsberg for their speedy yet careful reading of this thesis; and to Jeanne Miller for a great deal of assistance in preparing this manuscript.

My parents deserve much credit for the completion of this work. Without their support and encouragement throughout a seemingly endless college career, I might never have finished.

Finally, and most importantly, I thank my wife Sherri. With her help, graduate school, which could have been one of the worst experiences of my life, was made one of the best.

TABLE OF CONTENTS

Page

1. A Theoretical Overview of Charm..... 1

2. The Mark II Detector..... 2

   Appendix 2A. The BTRAKR Traking Strategy..... 39

   Appendix 2B. Derivation of the Formulae Used by BTRAKR..... 42

3. The Ratio of D Meson Production to Muon Pair Production in e^+e^- Annihilation as a Function of Center of Mass Energy..... 52

4. D Meson Production in the Resonance Region..... 72

5. D Production at a Center of Mass Energy of 5.2 GeV.....108

6. Summary and Conclusions.....134

References.....137

Chapter 1 A Theoretical Overview of Charm

This chapter is intended to remind the reader of some of the salient points concerning charm production. Only those features of the charm model which are relevant to an understanding of the data analysis in this thesis are discussed. For more extensive reviews, the reader is referred to Applequist, Lane, and Barnett[1] for theoretical aspects of charm, and to the recent review of Goldhaber and Wiss[2] for the experimental details.

The quark model, first proposed by Gell-Mann and independently by Zweig in 1964, explained the existence of all hadronic matter observed up to that time as combinations of three kinds of quarks; u, d, and s. Experimentally, there was no need for additional kinds of quarks (or flavors), and it was only when Bjorken and Glashow[3] proposed the charmed quark (c) as a way of explaining the absence of strangeness changing neutral currents and the smallness of the K_L-K_S mass difference that the concept of charm was born.

The discovery of the psi family in 1974, the "November Revolution" of elementary particle physics, proved that charm, and even the quark model itself, were more than just the mathematical tricks of some clever theorist. The observed narrowness of the hadronic widths of the ψ, ψ', and χ states, in agreement with the predictions of the Okubo-Zweig-Iizuka suppression hypothesis,[4] gave strong indications that charm was at hand.

The Glashow-Iliopoulos-Maiani (GIM) model[5] puts charm into the weak hadronic current in such a way as to force the strangeness

changing neutral current to vanish, to lowest order in G in the limit of SU(4) symmetry, that is, in the limit that the u, d, and s quark masses are identical to the c quark mass. Explicitly, the weak hadronic current is

$$J^{\mu}_{\text{hadronic}} = \bar{u}\gamma^{\mu}d' + \bar{c}\gamma^{\mu}s' \tag{1.1}$$

where $d' = d\cos\theta + s\sin\theta$, $s' = s\cos\theta - d\sin\theta$, and θ is the Cabibbo angle with $\sin^2\theta = 0.05$. Because the K_L-K_S mass difference is well known, the GIM model gives a prescription in broken SU(4) for the charmed quark mass of approximately 2 GeV. Thus charmed mesons composed of a charmed quark and a non-charmed anti-quark should have a mass close to 2 GeV also if the binding energy of the $q\bar{q}$ pair is small relative to the mass of the two constituent quarks.

The hadronic weak interaction is written in the form

$$H^{\text{weak}}_{\text{hadronic}} = \frac{G}{\sqrt{2}} J^{\mu} J^{+}_{\mu}$$

where J^{μ} is as in equation 1.1. This has the important practical consequence that one should look for K mesons in the final state as a means of detecting the existence of charmed quark decays. The characteristic signature of the charmed quark decay has been described in detail (and with considerable prescience) by Galliard, Lee, and Rosner.[6] They noted that charmed mesons composed of either $c\bar{u}(D^0)$ or $c\bar{d}(D^+)$, or the charge conjugate states $u\bar{c}$ and $d\bar{c}$, could be observed as narrow peaks in the invariant mass combinations $K^{\mp}\pi^{\pm}$

or $K^{\mp}\pi^{+}\pi^{+}$. The quark diagrams for these decays are illustrated in figures 1.1a and 1.1b.

Direct observation of D meson decays was first reported in 1976 when the SLAC-LBL Mark I collaboration observed the decays: $D \rightarrow K^{\mp}\pi^{+}$, $D \rightarrow K^{\mp}\pi^{+}\pi^{+}\pi^{\mp}$, and $D^{+} \rightarrow K^{\mp}\pi^{+}\pi^{+}$.[7] This same collaboration also observed the existence of the D^{*+} and D^{*0} directly, through the pionic decay of the D^{*+} into a D^{0}, and as a peak in the effective recoil mass spectrum opposite a detected D[8]. The Mark I collaboration also determined that the D* decays through photon emission at a rate competitive with the pion emission mode due to the smallness of the D*-D mass difference[7].

The spin and parity of the D and D* were determined to be consistent with the assignments 0^{-} and 1^{-} respectively[9]. This assignment was confirmed by the Lead Glass Wall experiment[10].

The information regarding D and D* masses and allowed decay modes is summarized in figure 1.2. Of particular interest is the fact that the decay $D^{*0} \rightarrow D^{+}\pi^{-}$ is kinematically forbidden and that the decay $D^{*0} \rightarrow D^{0}\gamma$ occurs at a rate comparable to the pionic D^{*0} decay rate. The number superposed over each decay line in the figure shows the mass difference (in MeV/c^{2}) between the D* and its decay products.

The production of both psi and D mesons has led theorists to formulate a mechanism for the production of $c\bar{q}$ (with $\bar{q} = \bar{u}$, $\bar{d}$, or $\bar{s}$) states in terms of a flavor independent interaction which causes the transition from the state $|\, c\bar{c} >$ to the state $|\, c\bar{q}, q\bar{c} >$. The assumption of flavor independence is a particularly powerful one. As first

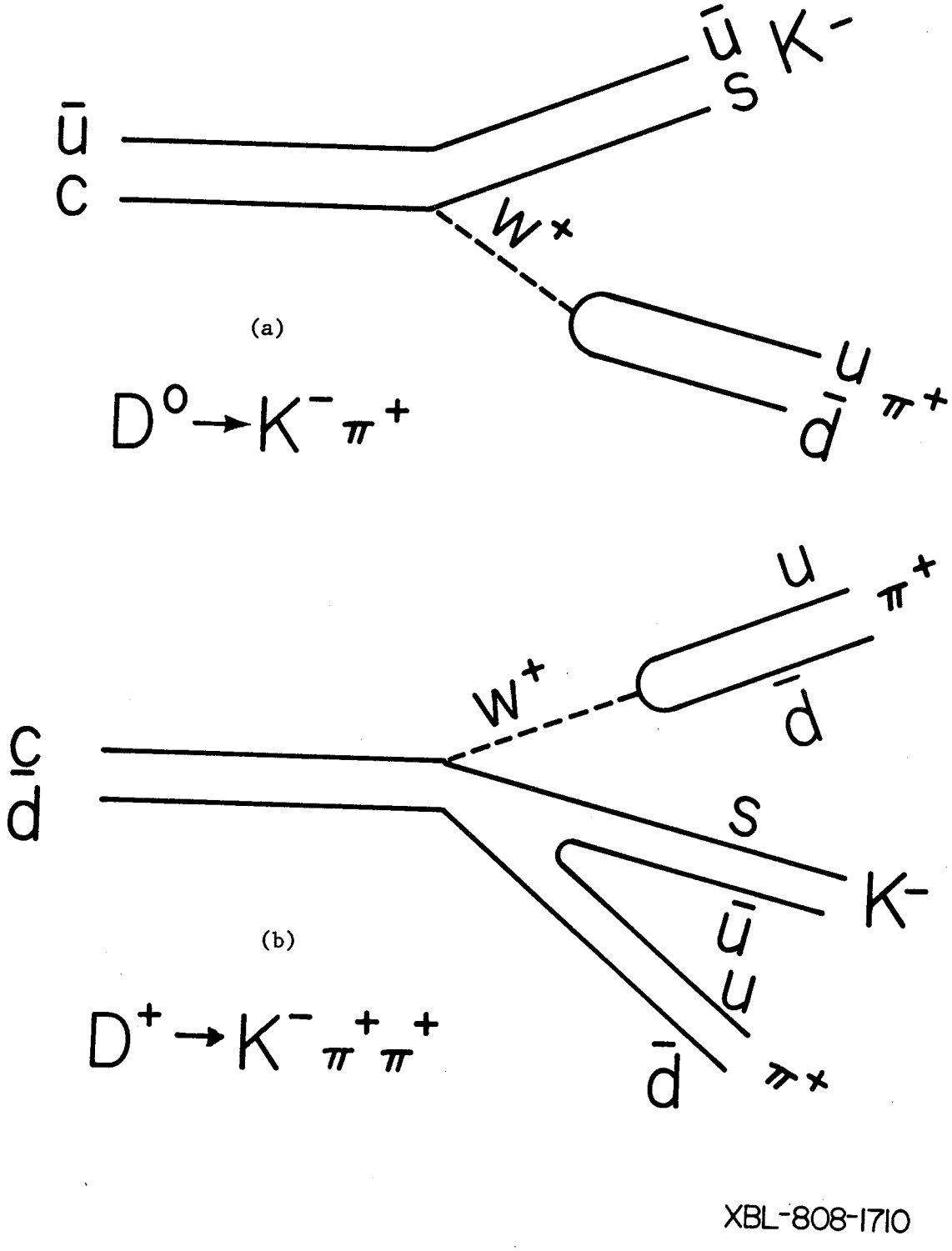

figure 1.1

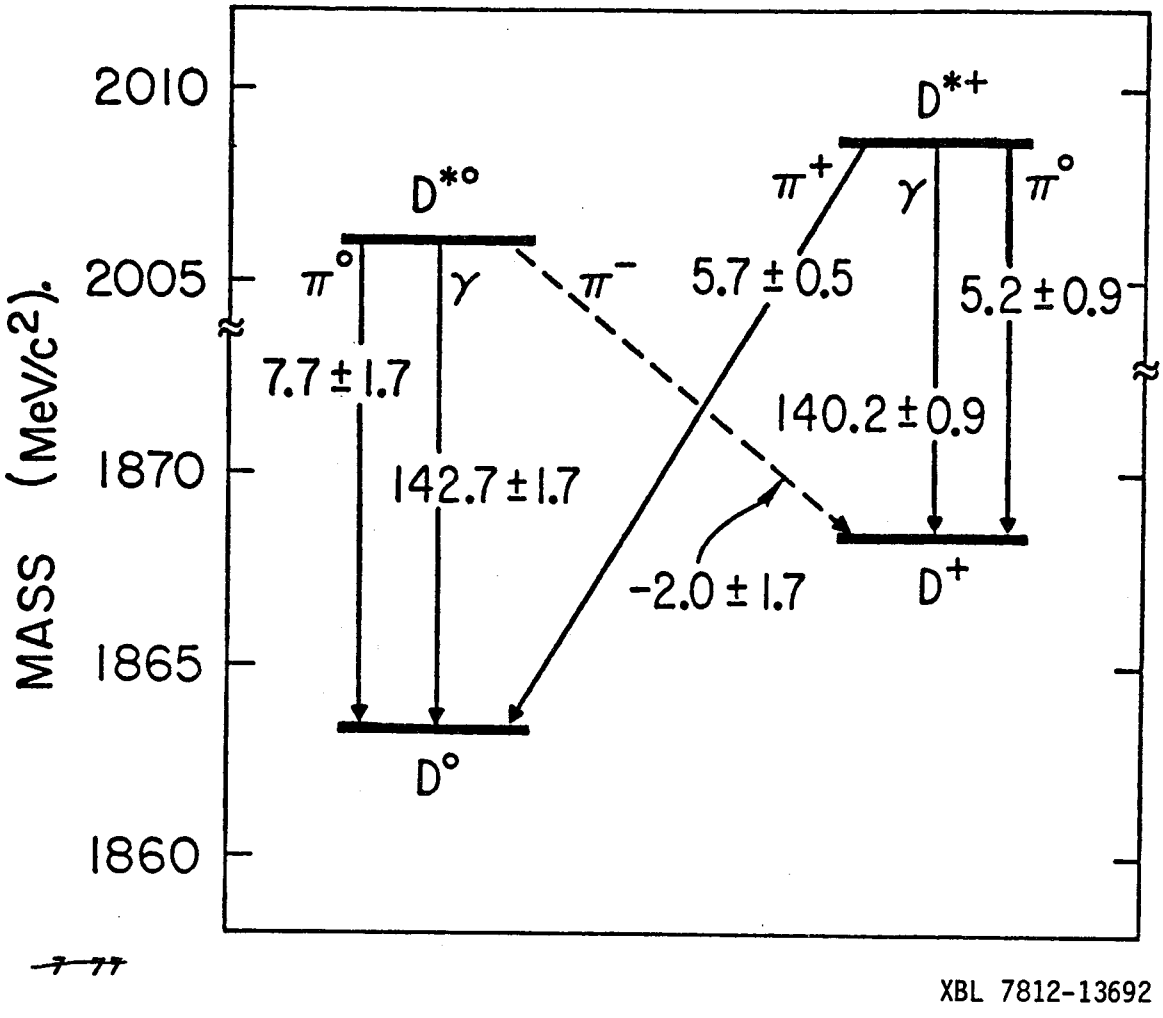

figure 1.2

The numbers shown are mass differences in MeV/c^2 of the D^*'s and their decay products.

recognized by Applequist and Politzer[11], the heavy $Q\bar{Q}$ states (with Q = c or b) of the psi and upsilon families are non-relativistic systems and present a strong interaction analogy to positronium. Thus, one can formulate an interaction which incorporates the property of quark confinement and test its validity by solving the Schroedinger equation to calculate the energy levels of the discrete bound states of the psi family. Since this potential is flavor independent, the interaction should also describe the amplitude

$$< c\bar{q}, \bar{c}q \mid H_{interaction} \mid c\bar{c} >.$$

In particular, this amplitude should describe the structure observed in R ($=\sigma_{hadrons}/\sigma_{\mu^+\mu^-}$) near a center of mass energy of 4 GeV and also the peculiar fact that $D^* \bar{D}^*$ production is vastly more common than $D \bar{D}$ production so close to kinematic threshold.[12] This theory will be discussed in more detail in chapter 4.

It is the study of the amplitude given above that is the topic of this work, the production mechanism of D mesons. To accomplish this, D's must be detected at various momenta and at a variety of center of mass energies. How this is accomplished is described in chapter 2.

Chapter 2. The Mark II Detector

Description of the Detector Components

The Mark II detector (see figure 2.1) is an apparatus designed to detect the products of the interaction of high energy electrons and positrons. The detector's various components are able to detect a variety of elementary particles useful in the analysis of e^+e^- interactions over a center of mass energy region extending from 3 GeV to above 30 GeV. Charged particles are detected and identified using the time of flight (TOF) counters, the drift chambers, and the solenoidal magnetic field, while photons and electrons are uniquely identified with the aid of the liquid argon shower counters (LA). The various sub-systems are described in more detail in the following sections with regard to their contribution to the data analysis described in this thesis.

2.1 The Pipe Counter

Immediately outside the beam pipe and concentric to it are two cylinders of scintillator with inner radii of 11 and 12.5 cm. These signals are part of the primary trigger requirement and cover about 96% of 4 π steradians. The pipe counter reduces the number of events caused by cosmic rays by insuring that at least one charged track in the event came within 11 cm. of the interaction region. At least one charged particle must traverse both cylinders if the event is to trigger.

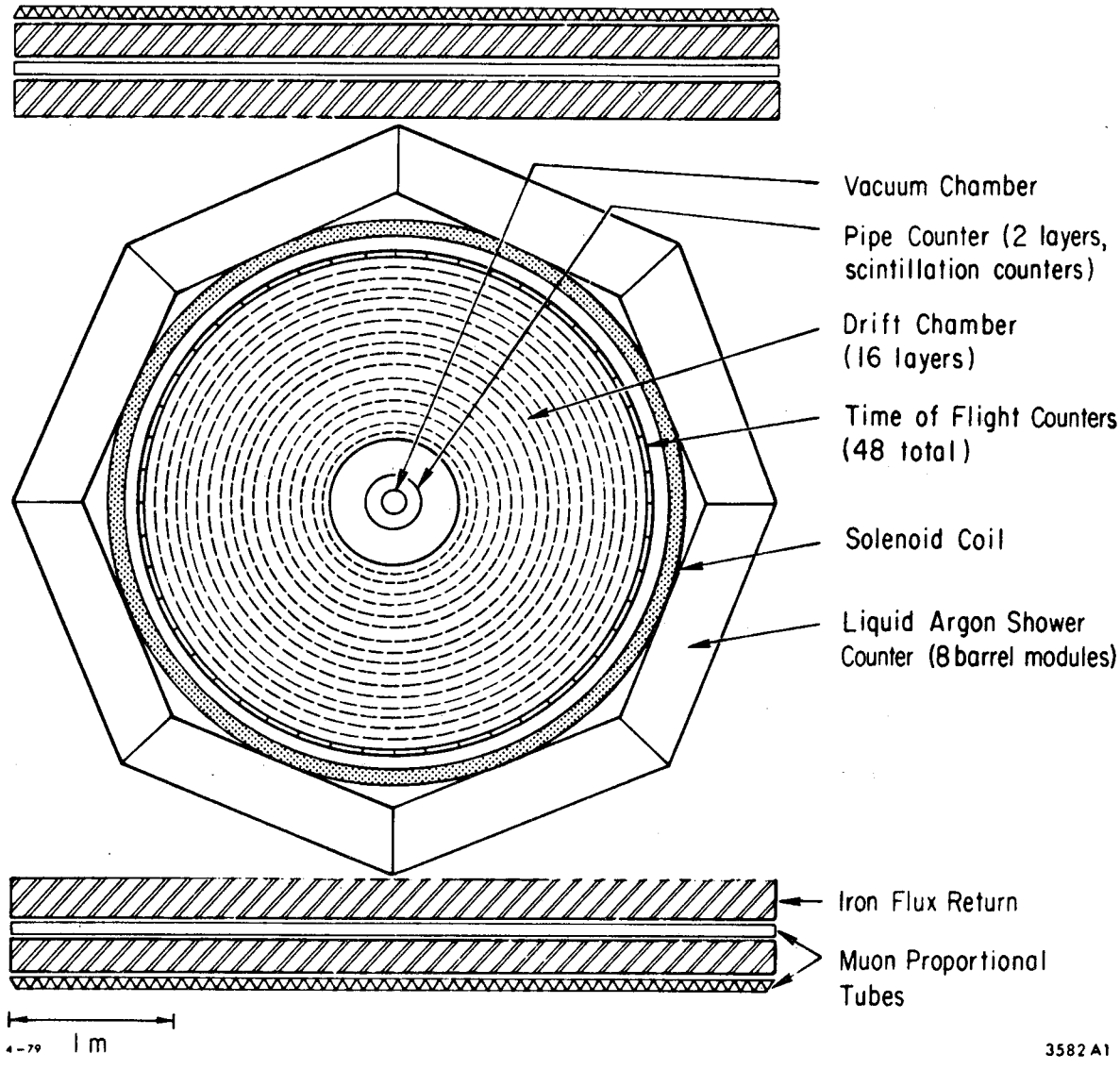
Vacuum Chamber
Pipe Counter (2 layers, scintillation counters)
Drift Chamber (16 layers)
Time of Flight Counters (48 total)
Solenoid Coil
Liquid Argon Shower Counter (8 barrel modules)
Iron Flux Return
Muon Proportional Tubes
1 m
4-79
3582 A1

figure 2.1

2.2 The Drift Chamber System[13]

Charged particles are tracked over approximately 85% of 4 π in solid angle by 16 concentric layers of drift chamber cells. Six of the layers have sense wires which run parallel to the beam direction whole the other ten layers have a three degree twist of one end relative to the other about the beam axis. Taken together, these layers yield x, y, and z (because of the twisted layers) information about all charged particles which traverse the drift chamber. The individual parameters of the various drift chamber layers are given in table 2.1

2.3 The Time of Flight System

The time of flight system consists of 48 scintillator counters. The 48 counters together form a cylinder 137 inches long and 120 inches in diameter corresponding to a solid angle coverage of 75% of 4 π steradians. Particle identification is done by determining the mass of a particle using the expression:

$$M = \frac{P}{c}\sqrt{\frac{1}{\beta 2}-1}$$

Therefore

$$M^2 = \frac{2p^2 t\Delta t}{L^2}$$

where p is the particle momentum determined by the drift chambers, L

Layer Index	Radius (mm)	Active Length (mm)	Stereo Angle (degrees)	Number of Cells
6	413.6	1984.1	0	144
7	482.6	2222.9	+3.12	168
8	551.5	2461.7	-2.90	192
9	620.4	2700.5	0	216
10	689.4	2786.4	+2.90	240
11	758.3	2786.4	-2.90	264
12	827.2	2641.6	0	144
13	896.2	"	+3.07	156
14	965.1	"	-3.07	168
15	1034.0	"	0	180
16	11.3.0	"	+3.07	192
17	1171.9	"	-3.07	204
18	1240.8	"	0	216
19	1309.8	"	+3.07	228
20	1378.7	"	-3.07	240
21	1447.7	"	0	252

Table 2.1

is the flight path length, βc is the particle's velocity, and Δt is the time resolution of the TOF system. This resolution was about 300 picoseconds for hadrons. The resolution was determined by calculating the expected TOF for particles whose TOF mass was close to that of the pion and far from the K meson mass. The distribution of expected times minus actual times was well described by a Gaussian distribution with a sigma of 300 picoseconds. The resolution allows the separation of pions and kaons by 1 sigma in the TOF mass resolution for particles with momenta less than 1.35 GeV/c. Similarly, kaons and protons can be distinguished from one another by at least one sigma in TOF mass as long as the momentum of the kaon or proton is less than 2 GeV/c. Electrons can also be separated from pions for momenta less than 0.3 GeV/c.

2.4 The Lead-Liquid Argon Shower Counters[14]

Surrounding the magnet coil are eight lead-liquid argon shower counters, each consisting of interleaved layers of 2 mm. thick lead strips (1.36 radiation lengths) and 3 mm. of liquid argon. Alternate planes of lead are divided into strips running in the ϕ, θ, and U (45 degrees to θ and ϕ) directions. This makes possible the spatial localization of showers. Altogether each module has 14 radiation lengths of material and the eight modules cover 69% of 4π in solid angle.

The lead strips collect the charge created by the traversal of a charged particle and this total charge is scaled to obtain the energy of the incident particle which initiated the shower. The calibration

to determine this scaling of charge versus energy is done by observing the pulse height created by non-radiative Bhabha events. The energy is then scaled to the momentum determined from the drift chamber tracking minus a correction for energy loss in the coil and leakage out the back of the module.[15]

2.5 The Trigger Logic System

The Mark II utilizes a two level trigger logic system. The primary trigger requires:

1. the crossing of the electron and positron beams in the interaction region,
2. a signal in both layers of one half of the pipe counter,
3. hits on a subset of the 16 drift chamber layers (usually 4 of the layers),
4. and under particularly noisy running conditions where many spurious hits occur in the drift chambers the TOF is also required to have at least one hit.

The coincidence of all these requirements produced a primary trigger rate of roughly 1 kHz.

If the primary trigger condition was satisfied, a secondary trigger was implemented (See ref. 16 for a more detailed description). Twenty four parallel processors, dubbed "curvature modules", search the paraxial drift chamber layers for hit wires. Each curvature module isolates tracks with a different range in rigidity by masking off a particular region of the drift chamber (see figure 2.2). All 24 modules have a particular orientation at one time. A

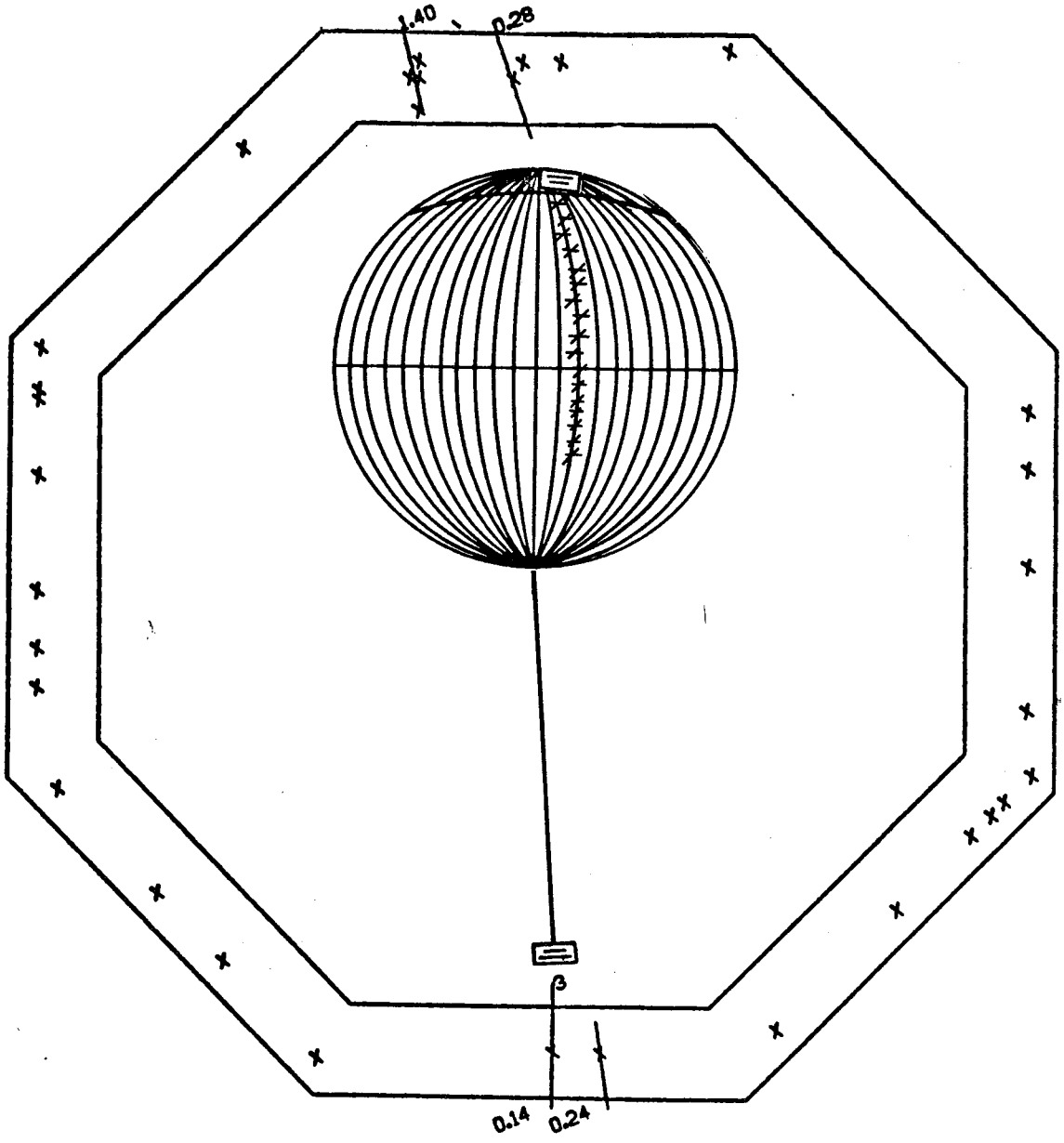

XBL 808-10936

figure 2.2

track is defined in trigger logic when a mask contains hits on four of the six paraxial drift chamber layers. If such a condition is found for any of the curvature modules, a type "A" track is counted by the track counter. After the search is completed, all 24 curvature modules are simultaneously rotated by $2\pi/252$ and the process is repeated.

In addition to type "A" tracks, type "B" tracks are also defined. The intention of "B" type trigger logic is to trigger the detector on tracks which are produced with $|\cos(\theta)| > 0.85$. Such tracks traverse only a few of the inner drift chamber layers before emerging from the drift chamber region. A "B" curvature module searches a masked region approximately 12 drift chamber cells wide and five layers thick. A "B" track is defined in the trigger logic as a hit on any three of the inner five layers. The time for these curvature modules to search the entire drift chamber is about 30 microseconds.

A secondary trigger occurs if any of the following conditions are met:

1. more than one "A" track is found,
2. at least one "A" track and at least one "B" track are found,
3. two "B" tracks are found approximately opposite in azimuthal angle (called a "back to back" trigger).

Since the drift chambers are at least 97% efficient on a cell by cell basis, the secondary trigger efficiency is greater than 0.999.

Figures 2.3a, 2.3b, and 2.3c show computer reconstructions of

A > 1

A,B > 0

"back to back"

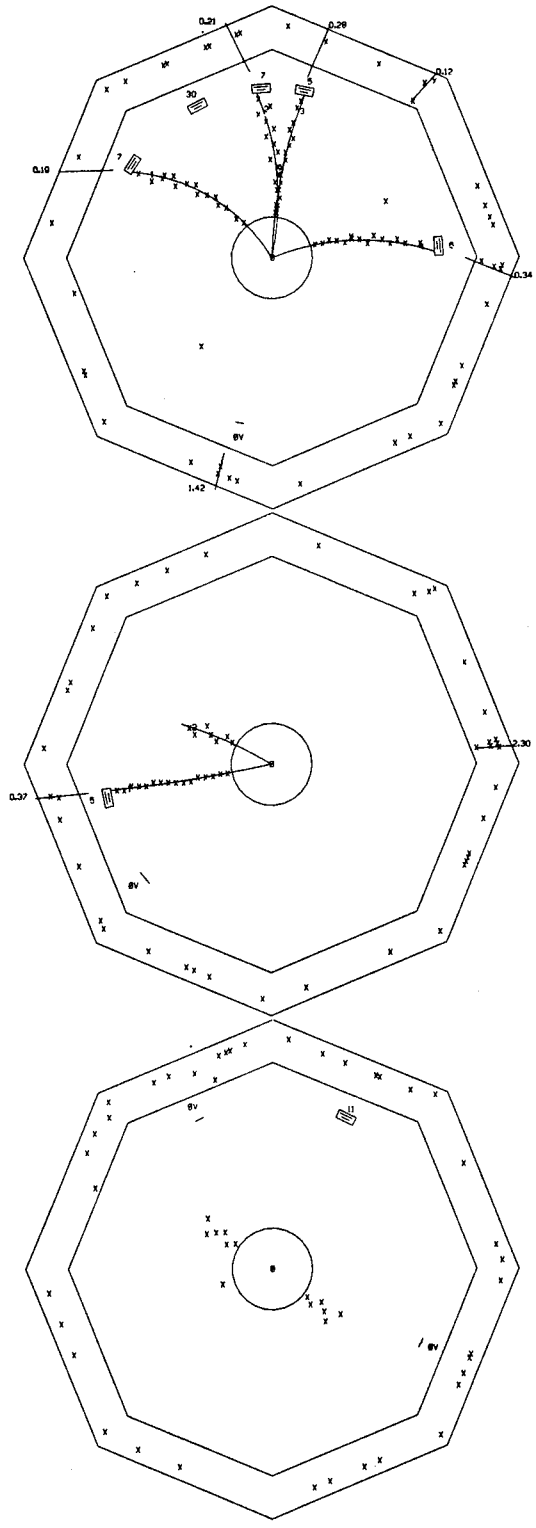

XBL 808-10904

figure 2.3

events which satisfy the three different secondary trigger possibilities described.

2.6 Charged Particle Trajectory Reconstruction

Charged particle trajectories are obtained by using the information from the drift chambers. Each time a charged particle passes through a drift chamber cell, the time lapse between the primary trigger and the arrival of the first ion at the sense wire of the cell is digitized by a time to digital converter (TDC). Tracking involves associating traversed drift chamber cells together to form a track. This computerized game of "connect the dots" is complicated by the fact that a space point is not determined by recording only which cell was traversed and the drift time to the sense wire from the distance of closest approach. All that is known is that a particular cell was traversed by some particle and that it took a certain amount of time for the ions created by the charged particle in the drift chamber gas to drift to the sense wire. The strategy for tracking must therefore include a means of associating particular cells together to make a reasonable track and it must also include a formulation of the relationship between drift time and drift distance. The ambiguity over which direction the ions came from must then be resolved to obtain a precise spatial location for the distance of closest approach to the sense wire. The set of space points (one point for each drift cell traversed by the particle) can then be fit to a theoretical expression for the equation of motion of a

charged particle in a nearly uniform magnetic field.

The tracking in the Mark II is accomplished by a three tier package of computer programs. The first tier is a relatively crude tracking program which attempts to find tracks during the data taking. This is useful for determining the performance of the Mark II detector during data acquisition. For instance, once a track is found and fit, knowledge of its trajectory makes it possible to determine each point it traversed within the detector. Efficiencies and malfunctioning components can be found by calculating the path of the particle in all components (drift cells, the TOF system, liquid argon channels, and the muon system) the particle is predicted to have passed through, and then examining these components to see if a signal is actually there. At this lowest level a constant drift velocity is assumed for the ions in the drift chamber gas. This assumption yields a spatial resolution of about 500 microns within each cell. The trigger logic curvature modules define which cells are to be associated in a track. It is the fact that pattern recognition is done very fast by the curvature modules that allows this program to run concurrently with data taking. At a more sophisticated level, the physics of the non-uniformity of the electric field in the cell and the presence of the solenoidal magnetic field produced by the coil must be taken into account in resolving the spatial ambiguity.[17] The final tier of tracking is the cleanup program which attempts to reconstruct tracks that have a large dip angle (angle out of the x-y plane) and therefore cross only a few drift chamber layers before exiting the drift chamber. To compensate for the dearth of

drift chamber information, the locations of showers in the proportional chamber endcap, the liquid argon endcap, and the location of the interaction region are matched with drift chamber points that the lower tiers of tracking failed to associate with tracks.

2.7 TLTRKR

TLTRKR is the trigger level tracking routine. It is heavily dependent on the secondary trigger logic for its pattern recognition ability. Figure 2.4 illustrates the terminology of the trigger system. The clock time defines an orientation in space for the 24 curvature modules as a group. Each individual curvature module position is referred to as a road.

The road's relation to the direction defined by the clock time is given by a delay and a width. The delay is given as the number of cells to be subtracted from the center line of the aggregate curvature modules to obtain one boundary of the road and the width is the number of cells to be added to the delay to obtain the cell which is at the other boundary of the road. Delays and widths are defined only for the paraxial layers and the delays and widths are a function of the layer number. If any road contains hit drift chamber cells on four of the six layers the track counter records the clock time and the numbers of the roads which satisfy this requirement of four out of six hit layers. Inherent in this procedure are the problems of "stutter" and "chatter". Stutter happens when a real track causes more than one trigger logic track to be recorded. Chatter happens when more than one road in the same trigger logic track is caused by

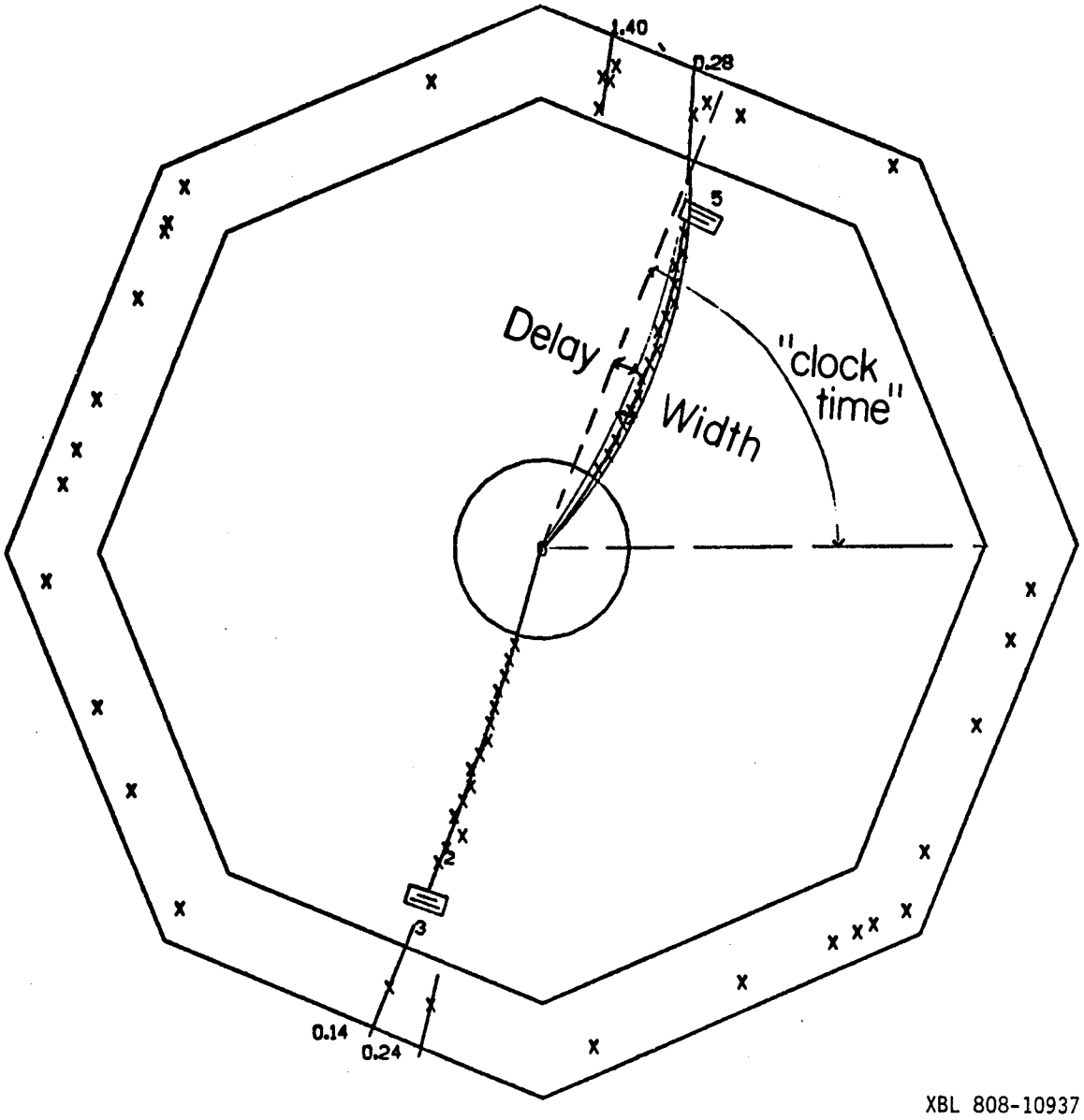

XBL 808-10937

figure 2.4

the same real track.

The procedure for overcoming these problems is twofold. First, the inclination of the local plane tangent to the drift chamber layer at the site of the hit cell is estimated from the curvature of the road with which the cell is associated. This reduces the ambiguity resolution to a one dimensional problem. Three of the paraxial drift chamber cells are then chosen out of the four to six struck cells within the road; the outermost, the innermost, and one in between. The eight possible circles which fit through the possible ambiguity resolutions are formed. The remaining one to three cells are then tested to see which choice of ambiguity most closely fits one of the eight hypothesized trajectories. The choice which has the best fit is taken to give the correct ambiguity resolution. Should the best fit fall outside a chi-square cut for goodness of fit, the original combination of three cells is discarded and a different choice of cells is tried. If the fit is acceptable, the cells which make up the track are then compared to those which lie on other roads of the same track and to those which lie on adjacent trigger logic tracks. If any cells are in common, they are deleted from the list of cells associated with the other roads. In this fashion the tracks are unscrambled from one another. The key is to have at least one track which is reasonably well separated from nearby ones so that its cells can be reliably identified among the ones belonging to the other tracks if they are in a common road at any point. In practice, TLTRKR fits about 80% of all tracks, being limited by topologies where several tracks cross. If the circle fit is successful, the

parameters of the track are used to interpolate its trajectory through the stereo layers, searching for the drift cell on each stereo layer which is closest to the interpolated trajectory. The collection of stereo points is then fit (i.e. the left-right ambiguities are resolved) to obtain the initial dip angle of the track at the interaction point.

2.8 TRAKR

At a more sophisticated level, the physics of the non-uniform electric and magnetic fields present in the drift chamber cells must be taken into account. TRAKR uses the TLTRKR fit results as a first approximation to a five parameter helix (see refs. 17 and 18 for more details on how the fit is actually done). Since the helix fit requires five parameters, the requirement is made that any track fit have at least seven associated cells so that drift chamber ambiguities can be reliably resolved. This limits the solid angle coverage of TRAKR to 85% of 4 π steradians.

2.9 BTRAKR

The charged tracks which exit the drift chamber into either endcap are generically referred to as "B" tracks, owing to the fact that the B trigger of the secondary trigger logic is designed specifically to find such tracks. The B tracks are not fit by TLTRKR and TRAKR because they typically have so few cells associated with them. TRAKR requires at least seven cells in order to do a fit, while TLTRKR requires a minimum of four paraxial cells and four stereo cells (a

more restrictive requirement on solid angle coverage as the stereo and paraxial layers are interleaved - see table 2.1).

To compensate for the scarcity of cells on B tracks, BTRAKR uses the location of the energy deposited in the endcap by the particle upon its exit from the drift chamber. Requiring proportional endcap chamber or liquid argon endcap chamber (see sections 2.11 and 2.12) information as well as drift chamber cells has an added benefit in pattern recognition; since all A tracks also produce B triggers, an A track which remained unfit by TRAKR could masquerade as a B track, were it not for the requirement of an associated signal in the endcap. A further benefit comes from knowing the production point of the charged particle as well as the drift chamber data. The x,y, and z coordinates of the interaction point and the errors on these coordinates are also used in the fit.

If TRAKR has succeeded in fitting the A tracks in the event so that a primary vertex can be found, BTRAKR can do even better as the interaction point and its associated errors are thus more precisely known.

Combining the drift chamber, shower counter, and vertex information allows BTRAKR to find tracks with just three associated drift chamber cells, thus extending the solid angle coverage of charged tracks to 92% of 4 π steradians.

The tracking efficiency of BTRAKR (determined by monte carlo simulation) was better than 99% for tracks for which it was possible to reconstruct the location of the energy deposited by the particle as it passed through the proportional chamber endcap or liquid argon

chamber endcap. Under actual running conditions the liquid argon chamber was not nearly as efficient as predicted by monte carlo estimates. This inefficiency was due to the spurious electronic noise which plagued the endcap. This noise made it harder to reconstruct the energy deposition of a minimum ionizing particle as it traversed the chamber because the amount deposited was so close to the background level. To a lesser extent this problem also caused an inefficiency in the detection of electrons. This caused the BTRAKR tracking efficiency to be about 92% for electrons and about 65% for minimum ionizing particles. The efficiency was determined by observing the decay:

$$\psi' \longrightarrow \pi^+\pi^-$$

followed by

$$\psi \longrightarrow e^+e^- \text{ or } \mu^+\mu^-.$$

The ψ' was identified by observing the effective mass recoiling against two oppositely charged pions which were both A tracks. If the recoil mass was within 100 MeV/c^2 of the ψ mass a charged track was searched for in the proportional chamber endcap. If the observed pulse height was greater than 300 MeV and the momentum measured by BTRAKR was close to one half the ψ mass the event was called $\psi \longrightarrow e^+e^-$. If the momentum was still half the ψ mass but the pulse height was less than 300 MeV the event was called $\psi \longrightarrow \mu^+\mu^-$. The efficiency was determined by counting how many charged tracks were

found in the liquid argon endcap when an electron was tracked in the proportional chamber endcap to determine the efficiency for electron tracking. Since three of the four tracks in the event were detected, it was possible to project where the electron should strike the endcap. Cuts were made so that only events which projected more than two strip widths from the edge of the endcap were used. This eliminated losses due to momentum measurement errors, multiple scattering, and signal leakage out the sides of the module. The same procedure was carried out with muons to determine the minimum ionizing particle tracking efficiency.

An example of an event reconstructed by the joint efforts of BTRAKR and TRAKR is shown in figure 2.5. Here both pions were tracked by TRAKR and give a missing mass roughly equal to the mass. The electrons were reconstructed by BTRAKR and have an invariant mass approximately equal to the mass also. The N and S in the figure indicate the locations of the reconstructed showers in the proportional and liquid argon endcaps respectively.

The momentum resolution of BTRAKR is a function of the polar angle θ. As $|\cos(\theta)|$ decreases the track crosses more drift chamber layers and the fit correspondingly increases in accuracy. A set of tracks was obtained where both TRAKR and BTRAKR were made to fit the same track. The resolutions shown in table 2.2 compare the results of the BTRAKR fit to the TRAKR fit in the variables P_T (the momentum of the particle in the x-y plane), $\cos(\theta)$, and ϕ. This is the true BTRAKR resolution only insofar as correlated errors between the two fit methods can be disregarded. To reduce the correlated errors as

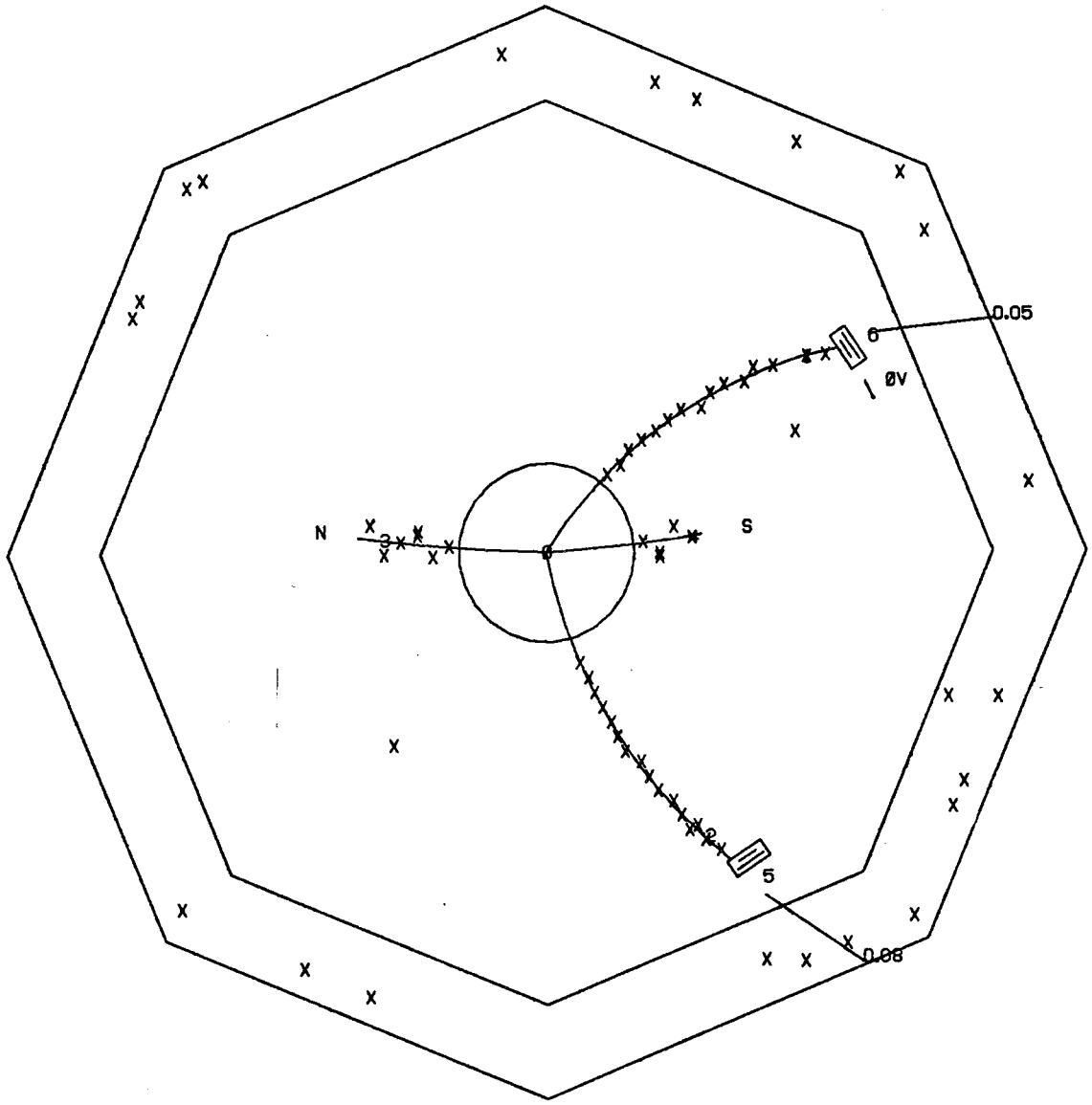

XBL 808-10938

figure 2.5

Comparison of track parameters for tracks fit by both TRAKR and BTRAKR

TRAKR single track fit compared to BTRAKR fit using beam crossing point

$\cos\theta$	$\frac{\sigma_{P_\perp}}{P_\perp^2}$ (%)	$\sigma_{\cos\theta}$ $\times 10^{-3}$	σ_ϕ mrad	
-.9 to -.8	15	10	10	proportional chamber endcap
-.8 to -.7	9	10	10	
.7 to .8	18	10	13	liquid argon chamber endcap
.8 to .9	25	10	22	

TRAKR vertex constrained track compared to BTRAKR fit using interaction point

$\cos\theta$	$\frac{\sigma_{P_\perp}}{P_\perp^2}$ (%)	$\sigma_{\cos\theta}$ $\times 10^{-3}$	σ_ϕ mrad	
-.9 to -.8	7	6	4	proportional chamber endcap
-.8 to -.7	3	6	3	
.7 to .8	15	6	11	liquid argon chamber endcap
.8 to .9	23	6	16	

Table 2.2

much as possible, only the tracks found by TRAKR which fit to a primary vertex were compared to the BTRAKR result for the same tracks. The results of this requirement are also shown in table 2.2. The improvement in resolution is obvious. Further details of the BTRAKR fitting procedure are given in the appendices to this chapter.

2.9 Determination of the Primary Vertex

In an event containing two or more tracks, a vertex point is reconstructed by finding a space point which minimizes the distance of closest approach for all charged tracks in the event. Only tracks with single track fits giving a distance of closest approach to the origin of less than 15 cm. are included in this procedure. Any track adding more than 100 to the chi-square of this fit is removed from consideration and the process is repeated. The process continues removing tracks until a successful fit is found or until the supply of tracks is exhausted. A more restrictive set of cuts is then imposed. All single tracks are examined to see if they form vees, such as in K_s decay, Λ decay, and gamma conversion. These tracks are fit to a secondary vertex and removed from further consideration in determining the primary vertex. Additional cuts are then imposed that the radial distance of closest approach be less than 1.5 cm. and that the distance of closest approach in z to z = 0 be less than 15 cm. for all tracks. The tracks surviving this cut are then vertex constrained.

2.10 Vertex Constrained Track Fits

Once the vertex has been determined, this additional space point can be added to the points given by the drift chamber to improve the overall momentum resolution. The charged particle rms momentum resolution becomes:

$$dP/P = [(.005P)^2 + (.015)^2]^{1/2}$$

where P is measured in GeV/c. The first term comes from the measurement error of the drift distances and the second term is from the multiple scattering of the particle as it crosses the beam pipe, pipe counter, Lexan, and drift chamber gas (equal proportions of argon and ethane).

2.11 The Liquid Argon Endcap

The liquid argon endcap was intended to provide the ability to detect photons and to distinguish electrons from minimum ionizing particles over that region of solid angle close to the beam pipe (7% of 4π). Spatial localization of showers was provided by six layers of lead strips with interleaved layers of liquid argon. The strip layout is shown in table 2.3. The combined thickness of the lead, liquid argon, and the vacuum box containing the entire module was 15 radiation lengths.

2.12 The Proportional Endcap

The proportional chamber endcap was designed in the same spirit as the liquid argon endcap but with less money. A layer of lead (2.5

Plane	Coordinate	Angle subtended (Degrees)	Number of channels per module
1	θ TRIGGER GAP	.5 - .9	64
2	ϕ	2.5	128
3	ϕ		
4	$e^{+\phi}$	2.5	135
5	$e^{-\phi}$	2.5	135
6	$e^{+\phi}$		
7	$e^{-\phi}$		
8	$e^{+\phi}$		
9	$e^{-\phi}$		
10	ϕ		
11	ϕ		
12	ϕ	5	64
13	ϕ		
14	ϕ		
15	ϕ		
17	ϕ	5	64
18	ϕ		
19	ϕ		
20	ϕ		
			590

ϕ strips run along constant ϕ (radially)

θ strips run along constant θ (concentric to the beam)

$e^{\pm\phi}$ are left and right spirals

Table 2.3

radiation lengths) preceded a signal layer (wire anodes surrounded by conducting strips painted onto G-10). The first signal layer had these conducting strips running radially outward from the beam line and in concentric circles to the beam line, while the second signal layer had strips running in left and right logarithmic spirals (as in the liquid argon endcap). The proportional chamber endcap covered 7% of 4 π solid angle and had a total thickness of 5 radiation lengths. This gave the proportional chamber an energy resolution of approximately $30\%/\sqrt{E}$ with E the energy of the incident electron or photon in GeV.

2.13 Event Selection

Events where D meson production occurred were identified through the decays:

$$D^0 \text{ or } \bar{D}^0 \rightarrow k^{\mp}\pi^{+}$$

$$D^0 \text{ or } \bar{D}^0 \rightarrow k^{\mp}\pi^{\pm}\pi^{\mp}\pi^{\pm}$$

$$D^{\pm} \rightarrow k^{\mp}\pi^{\pm}\pi^{\pm}$$

This required that charged kaons and pions be distinguishable from one another through the use of the TOF information. To reduce background events, it was also useful to separate, as much as possible, candidate kaons and pions coming from D decay from those charged tracks produced by background sources (such as beam-gas interactions) and also from those charged tracks produced by other non-charm

physics.

The first selection made on all tracks was that their closest approach to the origin in z be within 10 cm. Figure 2.6(a) shows the z distribution shows the distance of closest approach to z = 0 of all tracks. It is apparent that a 10 cm. cut should not exclude any of the charm events. Similarly, a selection on the radial distance of closest approach to the beam axis was made, with the requirement here being that R (the radial distance) be less than 1 cm. The distribution of R for all tracks and for all event primary vertices is shown in figures 2.7(a) and 2.7(b). These cuts in R and z cut down the background from uninteresting processes such as beam-gas and beam-pipe wall interactions while removing a negligible fraction of the charm production events.

All tracks passing this selection cut were required to have $|\cos(\theta)| < 0.75$, where θ is the angle the particle's momentum vector makes with the beam axis at the production vertex. The reason for this selection was that charged particle detection was not uniformly efficient over all of the solid angle encompassed by the detector. Beyond $|\cos(\theta)| = 0.85$ there was not enough drift chamber information available to construct trajectories with satisfactory momentum resolution, and between $|\cos(\theta)| = 0.75$ and $|\cos(\theta)| = 0.85$ the detection efficiency was a steeply falling function of $|\cos(\theta)|$. Figure 2.8 shows the distribution $dN/d\{\cos(\theta)\}$ for all events containing three or more charged tracks taken from a sample of data at 5.2 GeV center of mass energy. The effects of the detection efficiency are clearly evident. The requirement that $|\cos(\theta)| < 0.75$ allows one to make the

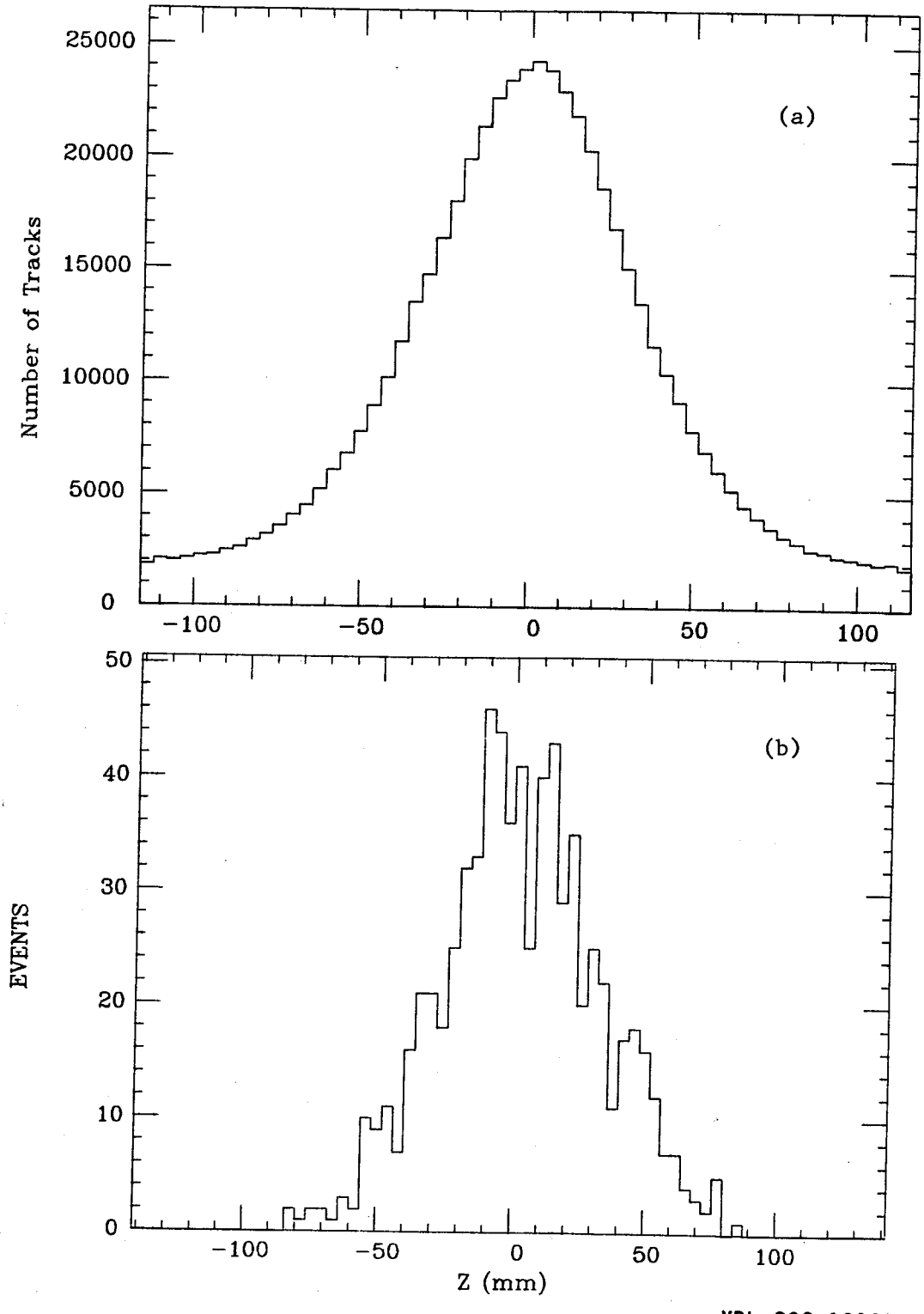

XBL 808-10900

figure 2.6
(a)- Z distribution of all charged tracks.
(b)- Z distribution of all events.

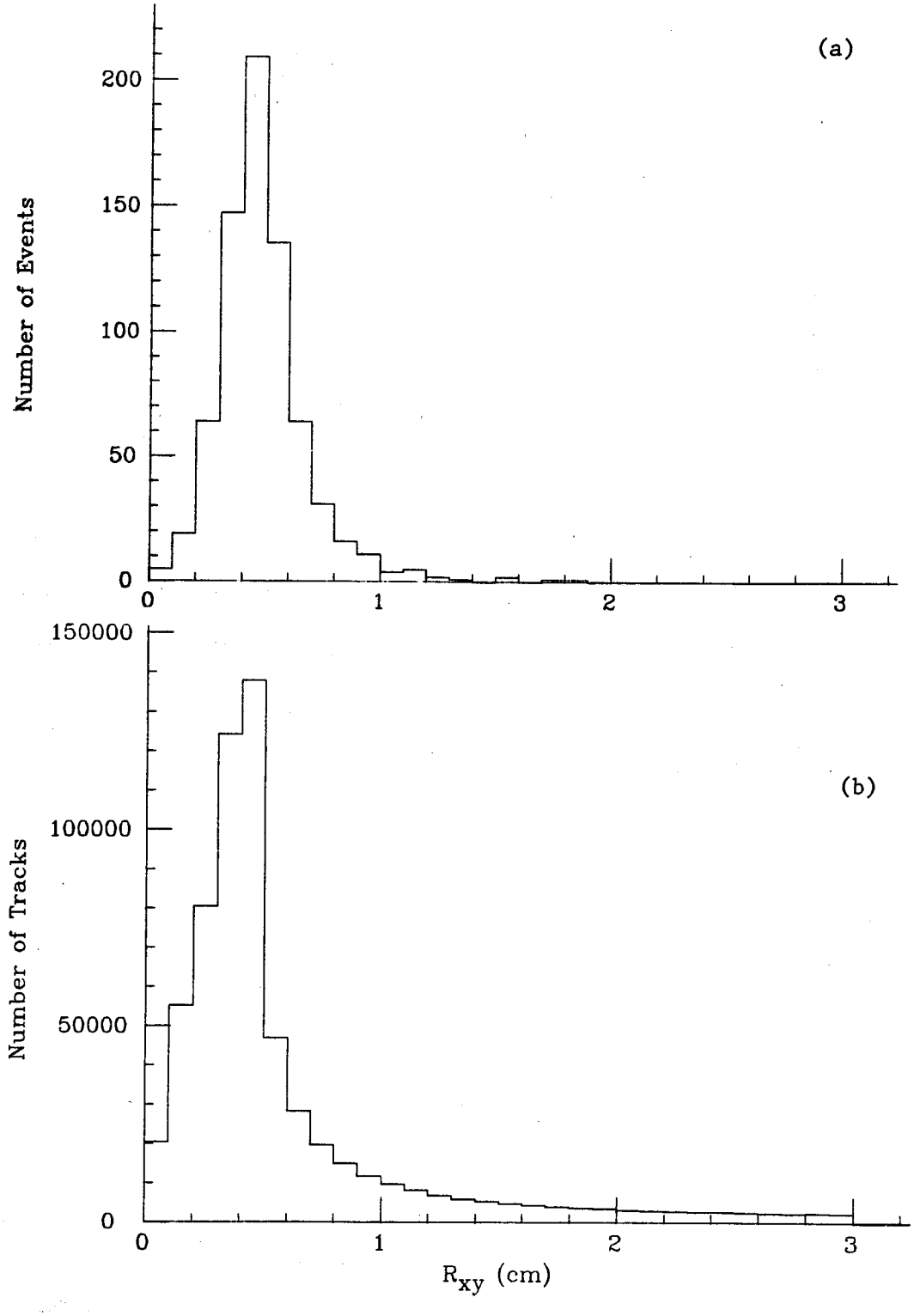

XBL 808-10899

figure 2.7

(a)- distribution of event vertices about the beam.
(b)- closest approach of all charged tracks to the beam.

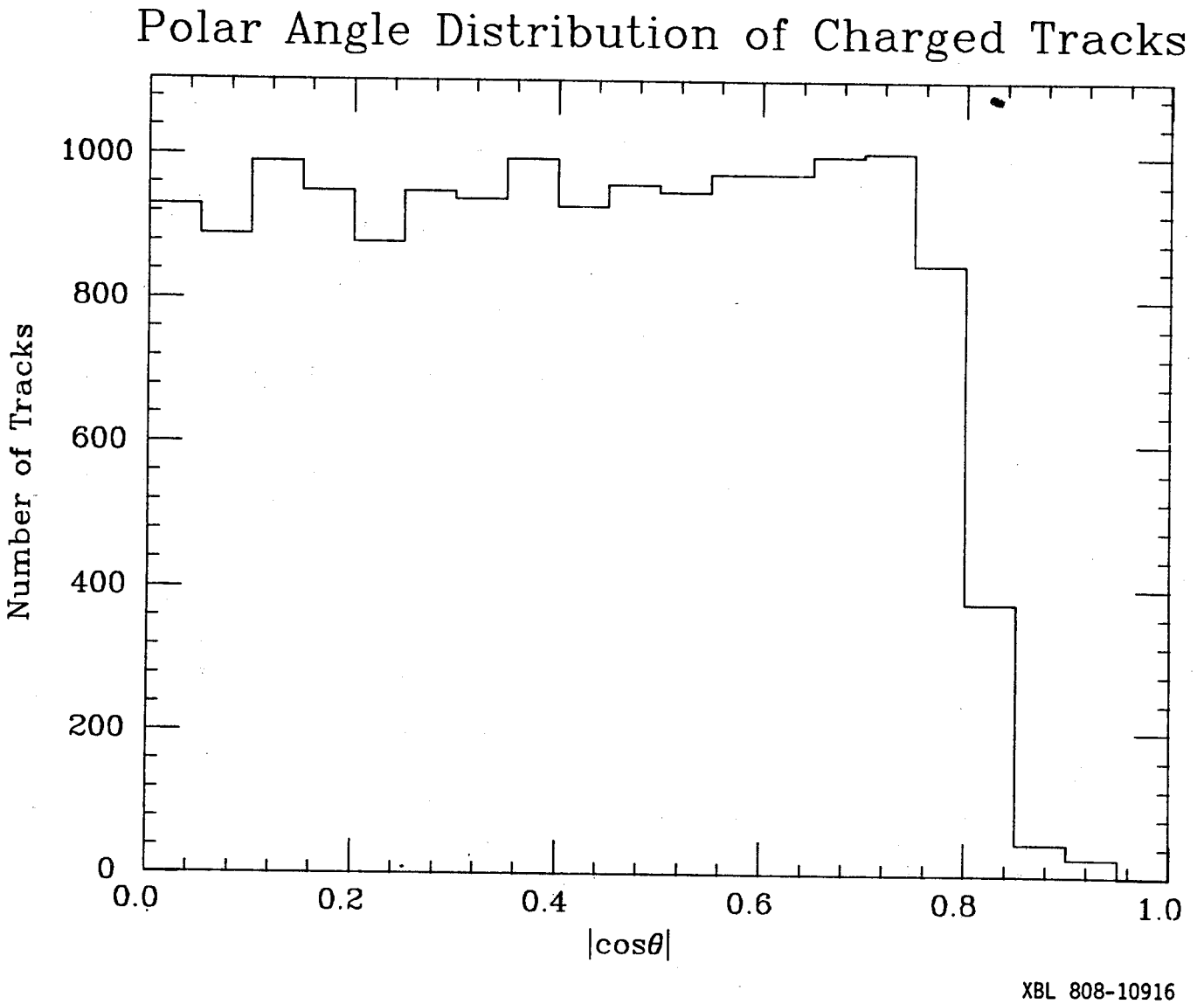
Polar Angle Distribution of Charged Tracks
Number of Tracks
1000
800
600
400
200
0
0.0
0.2
0.4
0.6
0.8
1.0
|cosθ|
XBL 808-10916

figure 2.8

simplifying assumption that the detection efficiency is uniform over the remaining solid angle.

The liquid argon modules made it possible to distinguish minimum ionizing particles from electrons as long as the momentum of the particle under examination was greater then 300 MeV/c. Details of the separation process are described in ref. 15. Below a momentum of 300 MeV/c, electrons were separated from pions using the TOF system. Figure 2.9 shows the distribution of electron TOF weights W_e , where

$$W_e = \frac{\exp -(t_{measured} - \langle t_e \rangle)^2/2\sigma^2}{\exp -(t_{measured} - \langle t_e \rangle)^2/2\sigma^2 + \exp -(t_{measured} - \langle t_\pi \rangle)^2/2\sigma^2}$$

and $\langle t_e \rangle$ is the expected time under the hypothesis that the particle is an electron. Any tracks with $W_e > 0.8$ were excluded from further consideration. The use of these cuts removed electrons produced in the semi-leptonic decays of D mesons, and thus reduced the combinatoric background in forming the invariant mass combinations $K^{\mp}\pi^{\pm}$, $K^{\mp}\pi^{+}\pi^{+}$, and $K^{\mp}\pi^{+}\pi^{\mp}\pi^{+}$. (Charged D mesons decay semi-leptonically to electrons $17\pm6.4\%$ of the time and neutral D mesons decay semi-leptonically to electrons $6\pm4\%$ of the time[17]. Since two D mesons are produced in each event the semi-leptonic decay of one D meson adds combinatoric background to the $K^{\mp}\pi^{+}$, $K^{\mp}\pi^{+}\pi^{+}$, and $K^{\mp}\pi^{+}\pi^{\mp}\pi^{+}$ mass combinations of the other D. Additional electrons were produced as Dalitz pairs and from photon conversions.

Above a momentum of 600 MeV/c, muons were separated from pions using the muon counters as vetoes. If a charged track pointed into

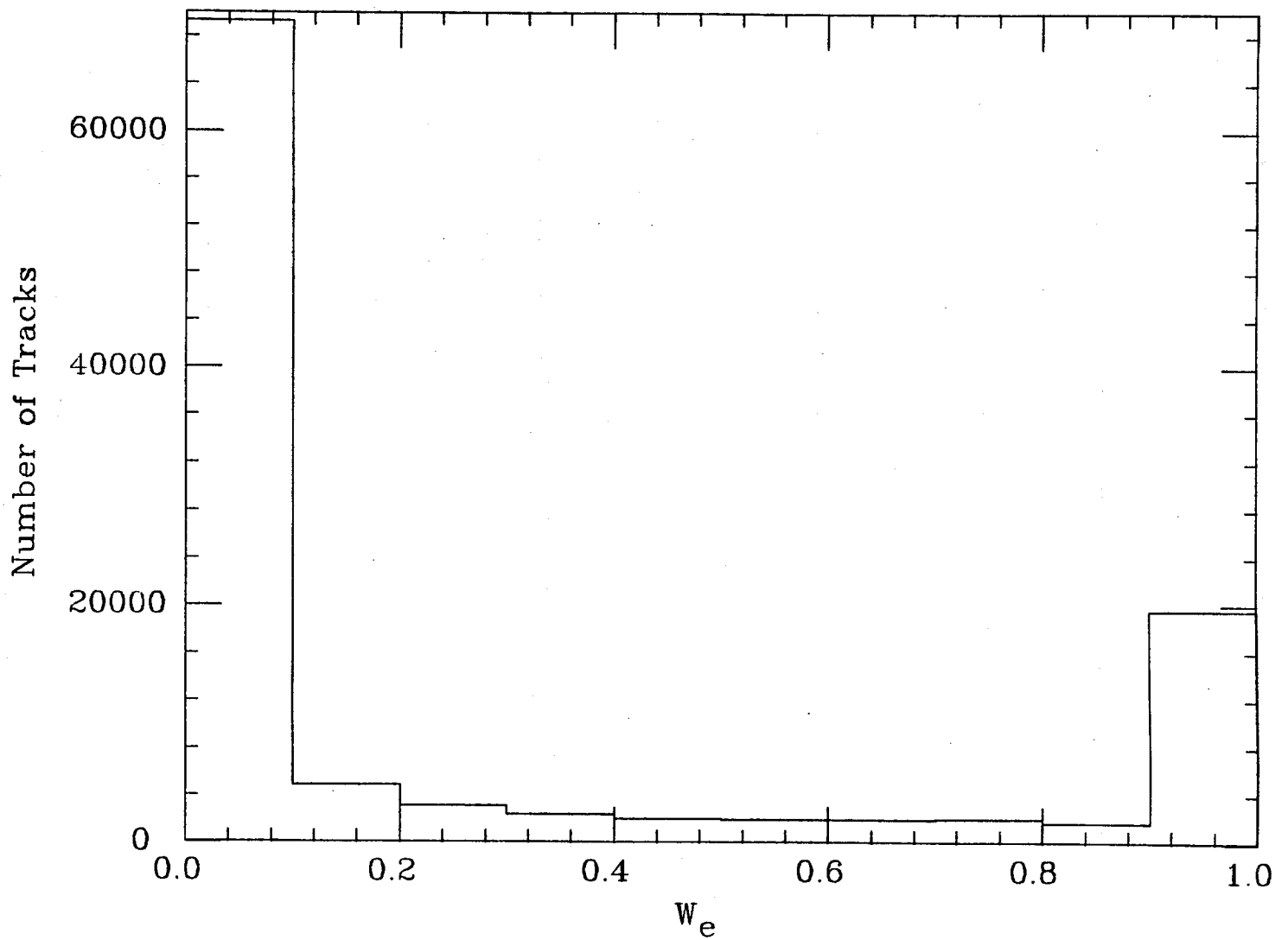

XBL 808-10915

figure 2.9

the muon system and a signal was detected on a proportional tube near the trajectory of the track, the track was identified as a muon and removed from further consideration in the analysis. This reduced the combinatoric background in making invariant mass combinations. In flight decay of particles which produced muons was a source of some inefficiency in K meson detection. While the loss of pions was small due to their long decay length (beta x gamma x 7.8 meters), the K meson loss was nearly 25% for K's produced in the decay $D^0 \rightarrow K^-\pi^+$ near center of mass energies close to 4 GeV. These losses were corrected for by a monte carlo which simulated in flight decays of pions and kaons and therefore made possible an estimate of the true detection efficiency of these particles.

The remaining subset of tracks was classified using the TOF system. Any tracks which had no TOF information (usually because of missing a TOF scintillator counter, hitting a dead scintillator, or hitting the same scintillator as another track) were arbitrarily labeled pions. The hadron TOF weights were defined in much the same way as W_e. Explicitly, the weight to be called a particle of type i is

$$W_i = \frac{\exp -(t_{measured} - \langle t_i \rangle)^2/2\sigma^2}{\sum_{j=\pi,K,p} \exp -(t_{measured} - \langle t_j \rangle)^2/2\sigma^2}$$

Tracks with $W_K > 0.5$ were called kaons, those with $W_p > 0.9$ were called protons or anti-protons, and the remaining tracks were called pions. The protons and anti-protons were then removed from the

remainder of the analysis. Figures 2.10(a), 2.10(b), and 2.10(c) show the TOF weights for the pion, kaon, and proton hypotheses at 5.2 GeV center of mass energy. These distributions were typical of all the data used in this analysis and show that the pions, K mesons, and protons (or anti-protons) identified by TOF have relatively little background from mis-identification within their individual populations.

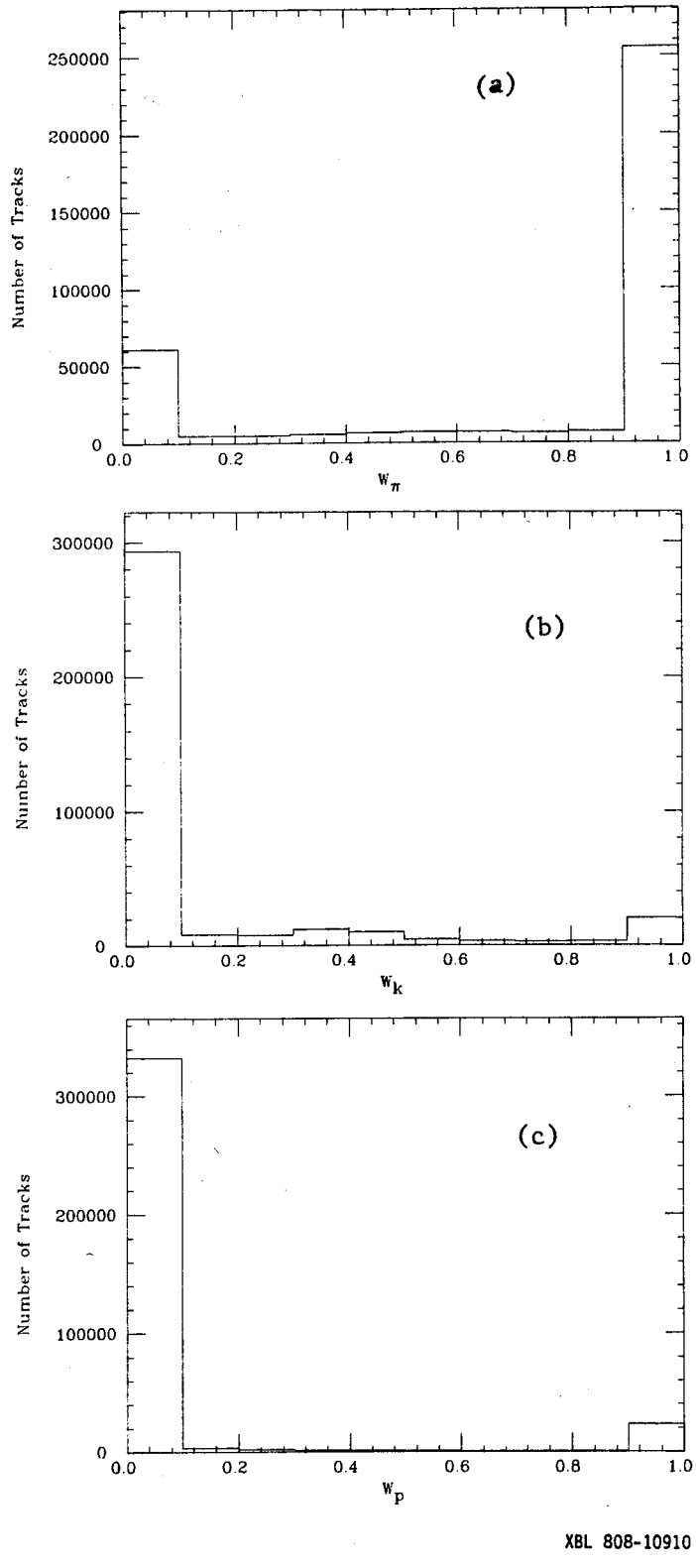

figure 2.10
(a)- pion hypothesis
(b)- kaon hypothesis
(c)- proton hypothesis

Appendix 2A The BTRAKR Tracking Strategy

BTRAKR uses three types of information to construct a track; drift chamber drift distances, the position of the event vertex (or the location of the beam beam crossing point if it was not possible to construct a vertex using type A tracks), and the location of any energy deposited in the proportional chamber and shower chamber endcaps. The goal of the tracking strategy is to unite these three data types into a trajectory consistent with the motion of a charged particle through a nearly uniform magnetic field. The problem is complicated because the charged tracks which go into the endcap typically traverse only a few of the innermost drift chamber layers because of the large dip angles these particles have when produced. Also, the endcap liquid argon shower counter was prone to noise pulses (spurious electronic noise) which simulated the detection of minimum ionizing particles. Thus, a few strategically placed noise hits in the drift chamber and either shower counter might appear to simulate the trajectory of a real charged track.

The track finding begins by choosing a drift chamber point on layer one or four which lies within the range of ϕ indicated by a road firing in B track trigger logic. (Some data was taken before the B track trigger logic was completed, and for this data any drift chamber cell on layer one or four was chosen). The endcaps were then searched to see if there was a shower within $\pi/8$ of the chosen drift chamber cell. If there were no endcap hits BTRAKR gave up at this point and went on to the next event. If no shower counter hits were

within $\pi/8$, a new drift chamber cell from layer one or layer four was chosen and the selection process was repeated.

If a shower was found, a search area was defined in software. One boundary of this search area was defined by the circle connecting the vertex (or beam crossing) position, the x and y coordinates of the drift chamber cell chosen which correspond to a negative ambiguity resolution in ϕ of the drift distance, and the negative (in ϕ) side of the endcap shower. The other boundary of this search area was determined by using the vertex (or beam crossing) point, the positive ambiguity resolution of the drift distance in the drift chamber cell, and the positive (in ϕ) side of the endcap shower. At this point the dip angle was calculated from the difference in z of the vertex (or beam crossing) position and the location of the endcap plane.

This search area and its associated dip angle now specify a very narrow area within the drift chamber to be searched for additional drift chamber hits. The dip angle is necessary for the search process since the region searched is populated mostly by stereo wires which do not give pure x and y coordinates unless one has knowledge of the dip angle. The ϕ angle of any struck sense wire can be written as

$$\phi \text{ (at } z=0) = \phi_0 + \frac{rk}{2} + \alpha \tan\lambda + \delta \qquad \text{(see appendix 2B.1)}$$

where ϕ_0 is the initial ϕ direction of the track, r is the radius of the drift chamber layer at z=0, k is the curvature in the xy plane of

the particle, α is the twist of the layer, λ is the dip angle of the track (the complement of polar angle), and δ is the drift distance divided by r. Thus knowing $\tan(\lambda)$ allows one to put stereo layers on an equal footing with paraxial layers as far as usefulness in pattern recognition. If at least least two additional hit drift cells are found in the search region, the drift chamber, endcap, and vertex (or beam crossing) points are all fit to a function which describes the trajectory of a charged particle within a nearly uniform solenoidal magnetic field. If the chi-square of the fit falls outside an acceptability cut, the track is rejected. Otherwise the track is taken to be a real track rather than just noise and the parameters of the fit are saved for further analysis.

It is possible to allow BTRAKR to work with only two drift chamber points, but when this is done the ability of the program to reject noise tracks became unacceptably poor for this category of tracks. With the requirement of three drift chamber points, hand scanning of real and monte carlo data found a tracking inefficiency of less than 1%, and no evidence of fake tracks.

Appendix 2B. Derivation of the Formulae Used by BTRAKR

Figure 2B.1 illustrates the nomenclature used in these derivations. The coordinate system used is the same as that described in chapter 1 for the detector in general. The z axis coincides with the detector's symmetry axis, and the x axis points towards the center of the SPEAR ring. The following variables are useful:

ϕ_1 = ϕ of a drift chamber sense wire at the detector's south end

ϕ_2 = ϕ of a drift chamber sense wire at the detector's north end

r = radius of drift chamber layer containing the sense wire

ρ = radius of curvature of a charged particle's trajectory $\equiv 1/K$

T_0 = azimuthal direction of charged particle at interaction point

T = azimuthal angle of charged particle at radius r

λ = dip angle of charged particle at radius r (angle measured out of the xy plane)

δ = drift distance = distance of closest approach of a charged track to the sense wire

ϕ_c = ϕ at xy plane of sense wire

L = length of drift chamber wire.

For a circle passing through the origin:

$$r = 2\rho \sin(T - T_0).$$

If $r/2\rho << 1$, $r/2\rho \simeq T - T_0$.

But $T = \phi_c + \varepsilon$

where $\phi_c = \dfrac{\phi_1 + \phi_2}{2}$

$$\varepsilon = (\phi_1 - \phi_c)\frac{Z}{L/2}$$

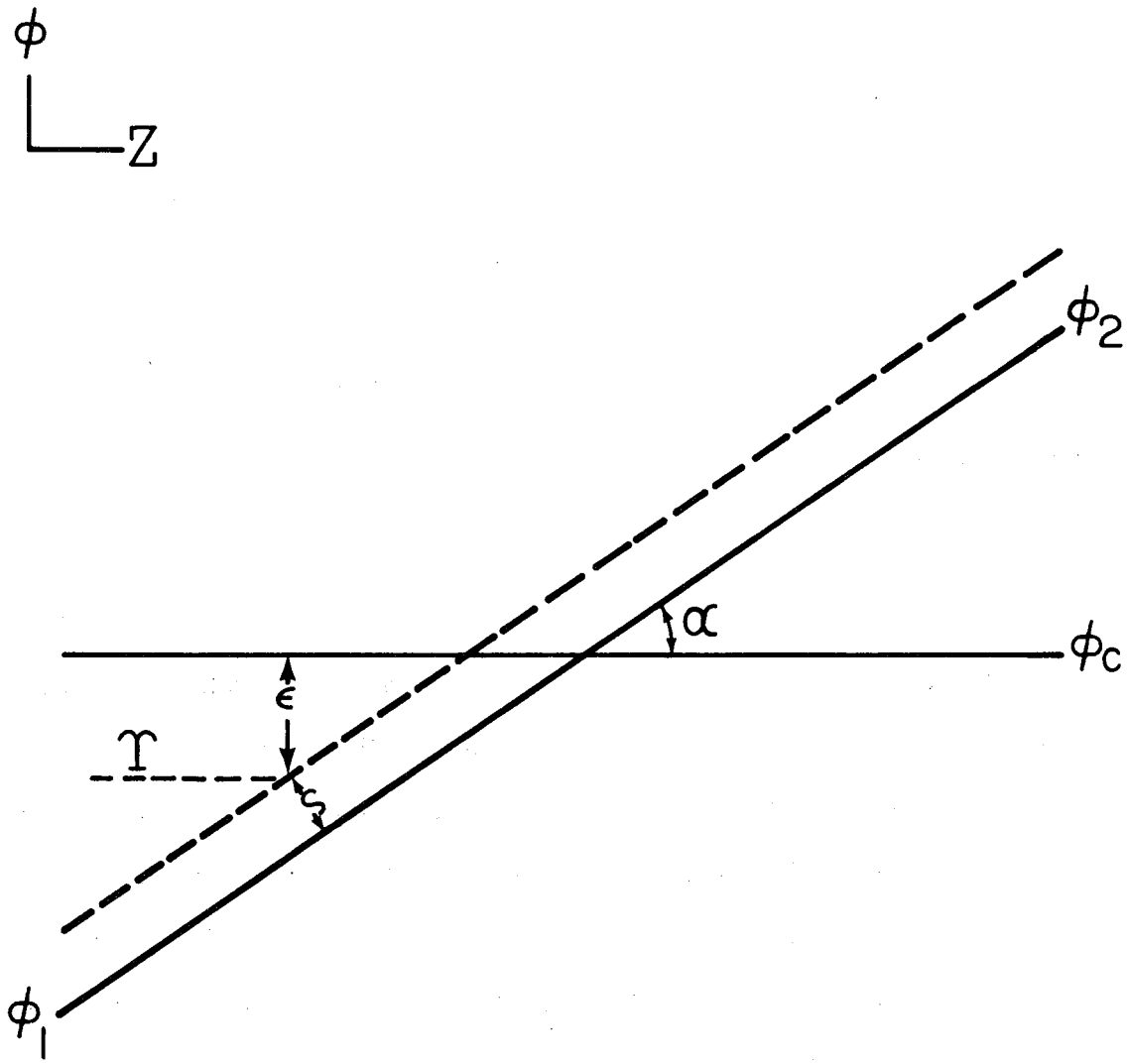

XBL-807-1668

figure 2B.1

Therefore $\varepsilon = \left(\frac{\phi_1 - \phi_2}{2}\right) \times \frac{2Z}{L}$.

So $\phi_0 + \frac{rk}{2} = \phi_c + \left(\frac{\phi_1 - \phi_2}{2}\right)\frac{2Z}{L}$.

Using $\alpha = (\phi_2 - \phi_1)\frac{r}{L}$

and $\tan\lambda = \frac{Z}{r}$

$$\phi_c \pm \delta = \phi_0 + \frac{rK}{2} + \alpha\tan\lambda \ .$$

Letting $\theta = \pm 1$

$$\phi_c = \phi_0 + \frac{rK}{2} + \alpha\tan\lambda + \theta\delta \ . \qquad (2B.1)$$

Equation 2B.1 is the basic equation used by BTRAKR. It is modified somewhat to take into account the following factors:

(1) The signal produced by the collection of charge in the drift chamber has a finite propagation velocity along the wire.

(2) The distance of closest approach of a charged particle to the sense wire does not in general lie in the plane tangent to the drift chamber layer at the sense wire.

(3) Because the stereo wires are straight lines (neglecting gravity induced sag, which is a very small effect) the distance of stereo wire to the Z axis is Z dependent.

(4) The magnetic field of the detector is not uniform, although nearly so.

(5) The interaction point of the electron and positron is in general not precisely at the detector origin.

These corrections are taken into account in the following sections.

2B.1 The Correction for the Finite Propagation Velocity of the Signal Along the Sense Wire

The following menagerie of variables is required:

ϕ_M = phi value obtained by taking the ϕ of the wire at the x-y plane of the detector (ϕ_c) and adding or subtracting the drift distance.

T_M = measured drift time

t_p = propagation time of signal along the signal wire

t_d = drift time

ξ = variable to account for the fashion in which the sense wires are read out. The first 8 are read out on the +Z end and the next 8 are read out at the -Z end.

ξ = -1, layers 1-8

+1, layers 9-16

v_d = drift velocity

v_p = propagation velocity.

With that taken care of, the following relations follow:

$$t_p = \frac{\frac{L}{2} \pm Z}{v_p} = \frac{\frac{L}{2} + \xi Z}{v_p}$$

$$\phi_c = \frac{rk}{2} + \phi_0 + \alpha\tan\lambda + \frac{\theta v_d}{r}\left(T_M - \frac{\frac{L}{2} + \xi Z}{v_p}\right).$$

But $Z = r\tan\lambda$.

$$\phi_c = \frac{rk}{2} + \phi_0 + \alpha\tan\lambda + \frac{\theta v_d}{r}\left(T_M - \frac{\frac{6}{2} + \xi r\tan\lambda}{v_p}\right). \qquad (2B.2)$$

2B.2 Correction for the Fact that the Distance of Closest Approach is Not in the Plane of the Drift Chamber Layer

See figures 2 and 3 for details of the variable definitions. Since Δ is the apparent drift distance in the xy plane

$$\Delta = \frac{\delta}{\cos\theta}$$

where θ is as defined in figure 3.

$$|\vec{r} \times \vec{R}_0| = rR_0\sin(\frac{\pi}{2} - \theta) \equiv rR_0\cos\theta = rR_0/\mu.$$

But $R_L^2 = 2R^2(1 - \cos\nu)$

$$\cos\nu = \cos(\pi - 2\theta) = \cos 2\theta$$

$$\cos\theta = \left[1 - \frac{R_L^2}{4R^2}\right]^{1/2} \equiv \frac{1}{\mu} .$$

Adding in this correction gives

$$\phi_c = \frac{rK}{2} + \phi_0 + \alpha\tan\lambda + \frac{\theta v_d}{r}\left(T_M - \frac{\frac{L}{2} + \xi r\tan\lambda}{v_p}\right)\mu .$$

2B.3 Correction for Non-Constant Radial Position of Stereo Wires

Fortunately for the reader, fewer variables can be introduced at this time.

Let X_N = X position of sense wire at north end of drift chamber. (This is the same as ϕ_2 is section 2B.1).

X_S = X position of the sense wire at the south end of the drift chamber ($=X_1$ from 2B.1)

$\Delta X \equiv X_2 - X_1$

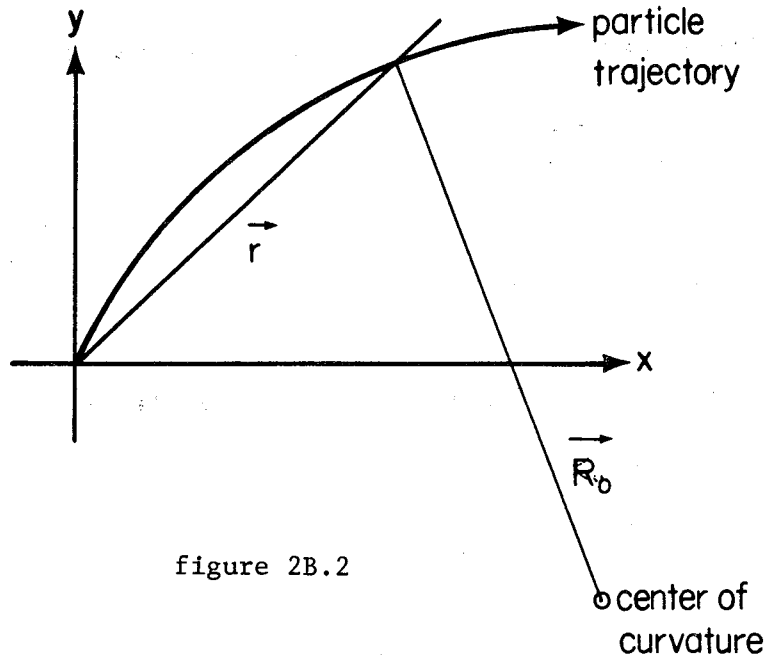

figure 2B.2

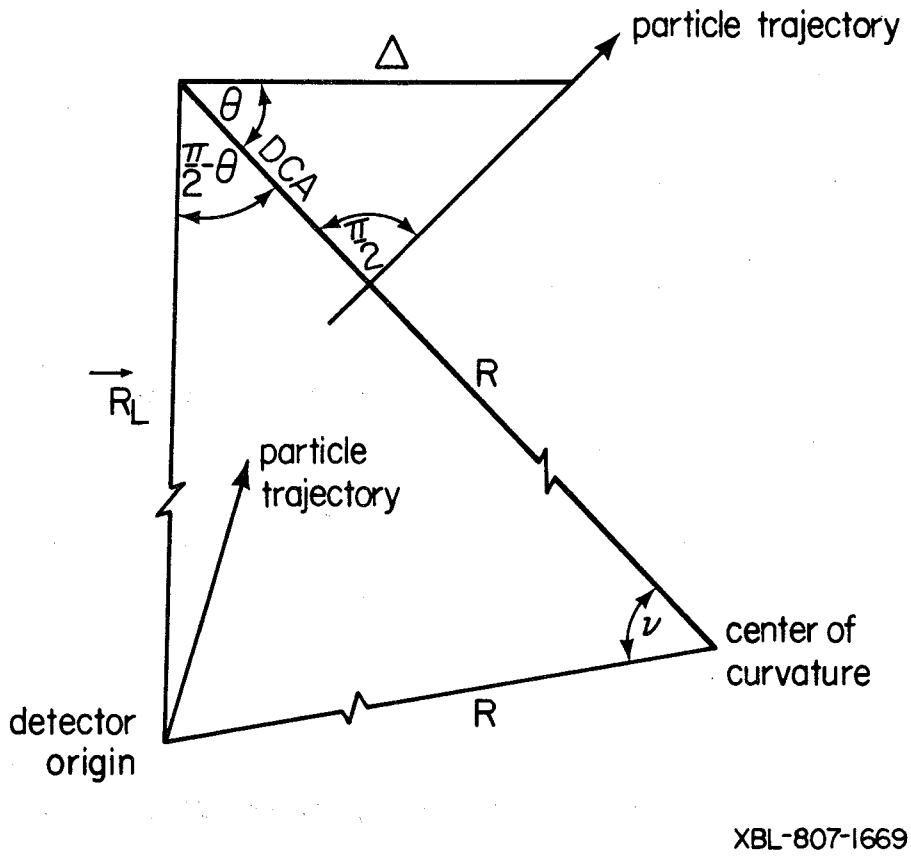

figure 2B.3

$\Delta Y \equiv Y_2 - Y_1$ with Y defined in analogy with X.

The X and Y positions of the sense wire can now be specified as functions of Z:

$$X = X_1 + \Delta X \left(\frac{\frac{L}{2} - Z}{L} \right)$$

$$Y = Y_1 + \Delta Y \left(\frac{\frac{L}{2} - Z}{L} \right).$$

The radial distance of the sense wire from the x-y plane is then given (after some algebra) as

$$R(Z) = \sqrt{X(Z)^2 + y(Z)^2}$$

$$= R_0 \left| 1 - \frac{(\Delta\phi)^2}{2} \left(\frac{1}{4} - \frac{Z^2}{L^2} \right) \right|$$

where $\Delta\phi$ is defined by:

$$1 - \cos(\phi_2 - \phi_1) \simeq \frac{(\Delta\phi)^2}{2}$$

and $R_0 \equiv \sqrt{X_1^2 + Y_1^2} = \sqrt{X_2^2 + Y_2^2}$.

This expression for R(Z) can now be used to modify equation (2B.2) given below for convenience

$$\phi_c = \frac{rK}{2} + \phi_0 + \alpha \tan\lambda + \frac{\theta v_d}{r} \left(T_M - \frac{\frac{L}{2} + \xi r \tan\lambda}{v_p} \right) \mu \quad .$$

Replacing r by $R \left\{ 1 - \frac{(\Delta\phi)^2}{2} \left(\frac{1}{4} - \frac{Z^2}{L^2} \right) \right\}$

and Z by $R \left(1 - \frac{(\Delta\phi)^2}{8} \right) \tan\lambda$, the following expression is obtained (to order $(\Delta\phi)^2$):

$$\phi_c = \left\{R \quad 1 - \frac{(\Delta\phi)^2}{2}\left(\frac{1}{4} - \frac{R^2\tan^2\lambda}{L^2}\right)\right\} \frac{K}{2} + \phi_0$$

$$+ \alpha\tan\lambda + \frac{\theta v_d}{R}\mu\left\{T_M - \frac{\frac{L}{2} + \xi R\tan\lambda \quad 1 - \left(\frac{(\Delta\phi)^2}{8}\right)}{v_p}\right\}. \qquad (2B.4)$$

2B.4 Magnetic Field Variation Correction

The magnetic field within the drift chamber is nearly uniformly in the Z direction. Any variation in the field and its effect on the track parameters can therefore be treated as a first order expansion in a small quantity. As in figure 2B.4, ϕ_i is the direction of a track in ϕ at layer i.

Thus $\quad \phi_{i+1} = \phi_i + \frac{(r_{i+1} - r_i)}{2} K_{i+1}$

where K_{i+1} is the curvature at layer i + 1.

The following relationship comes in handy:

$$P_\perp = .03B_i\rho_i \qquad (2B.4)$$

where $P_\perp$ is the transverse momentum of the particle to the field direction (a constant),

B_i is the magnitude of the magnetic field at layer i,

and $\quad \rho_i = 1/K_i$.

Also $\quad P_\perp = .03B_0\rho_0 \qquad (2B.5)$

where B_0 is the nominal uniform field and

$\rho_0 \equiv 1/K$ is the associated radius of curvature.

Equating 2B.4 and 2B.5

$$K_i = \frac{B_i}{B_0} K$$

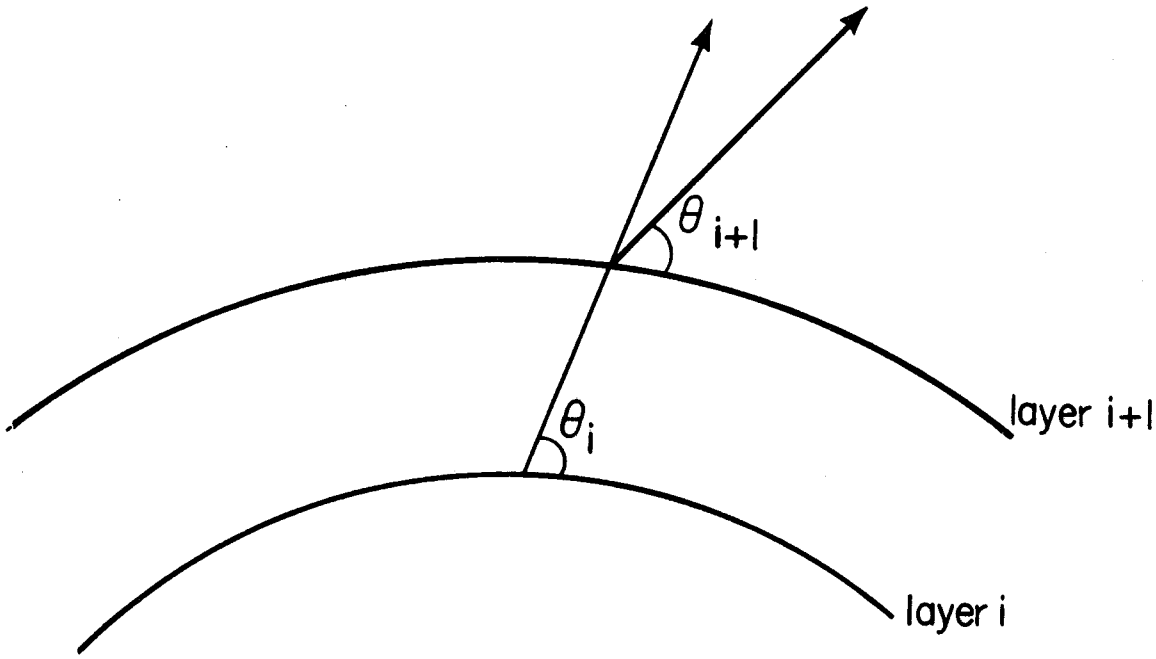

XBL-807-1667

figure 2B.4

and $\phi_{i+1} = \phi_i + \left(\frac{r_{i+1} - r_i}{2}\right)\frac{B_{i+1}}{B_0} K$

Since $\phi_1 = \phi_0 + \frac{r_i}{2}\frac{B_1}{B_0} K$

and $\phi_2 = \phi_1 + \frac{r_2 - r_1}{3}\frac{B_2}{B_0} K$

the expression for arbitrary layer n can be written as

$$\phi_n = \phi_0 + \frac{K}{2}\sum_{i=1}^{n} (r_i - r_{i-1})\frac{B_i}{B_0} . \qquad (2B.6)$$

In the limit of a uniform field (2B. 6) reduces to the by now familiar expression

$$\phi_n = \phi_0 + \frac{K}{2} r_n .$$

The net effect of this approximation is to replace r at layer n by

$$\sum_{i=1}^{n} (r_i - r_{i-m})\frac{B_i}{B_0} = r .$$

Chapter 3 The Ratio of D Meson Production to Muon Pair Production in e^+e^- Annihilation as a Function of Center of Mass Energy

3.1 Determination of a Model Independent D Meson Detection Efficiency

The production of D mesons in e^+e^- annihilation produces a final state consisting of 2 D's plus perhaps some number of other particles. It has been previously observed[19] that the production is entirely quasi-two-body below a center of mass energy of about 4.4 GeV, and at higher center of mass energies that it is consistent with the production of either two D's or two D*'s plus a "few" pions[20] The momentum distribution of produced D's in the resonance region (roughly 3.9 GeV to 4.4 GeV) is therefore markedly different from the momentum distribution of D's at higher center of mass energies. In the resonance region, where D production is quasi-two-body, the D's should all be approximately monochromatic. This is true even if the D is a result of a D* decay since the D*- D mass difference is so small. At higher center of mass energies, where D production is multi-body, the D mesons are produced in a continuous momentum spectrum.

These differences must be accounted for in determining the efficiency for detection of a D in a particular decay mode. For instance, if the probability of detecting a D^0 (in this chapter the reference to any specific charge state of a particle refers to the charge conjugate state as well) in the decay mode $K^-\pi^+$ decreases with

increasing D momentum, slow D's will contribute more to the observed $K^-\pi^+$ invariant mass peak than will fast D's when the production mode is multi-body. The goal here is to calculate a production model independent detection efficiency which is a function of the D momentum.

To determine the momentum dependence of the detection efficiency for $D^0 \rightarrow K^- \pi^+$ in a model independent fashion, monochromatic D^0's were generated at a variety of momenta in an isotropic angular distribution using a monte carlo and allowed to decay to a K^- and a π^+. Also, the K meson and the pion were allowed to decay via their standard branching ratios and lifetimes. The $K^-\pi^+$ invariant mass distribution was then fit (using a chi-square minimization technique) to a Gaussian distribution to determine the number of D^0's detected. The ratio of the number detected to the number produced is shown in figure 3.1a where the D^0's were produced isotropically. The width of the $K^-\pi^+$ invariant mass distribution is shown in figure 3.1b. A similar procedure was performed with D^+'s decaying to $K^-\pi^+\pi^+$. The $K^-\pi^+\pi^+$ invariant mass distribution was then fit to determine the detection efficiency and mass distribution width as a function of the D momentum. These results are shown in figures 3.2a and 3.2b.

The detection efficiency for $K^-\pi^+$ decreases much more rapidly with momentum than does that for $K^-\pi^+\pi^+$. This occurs for two reasons. The fact that both efficiencies decrease is a consequence of the finite resolution of the Mark II TOF system. K mesons produced in D decays have an increasing probability of being ambiguously identified as the K momentum increases. All tracks which satisfy the

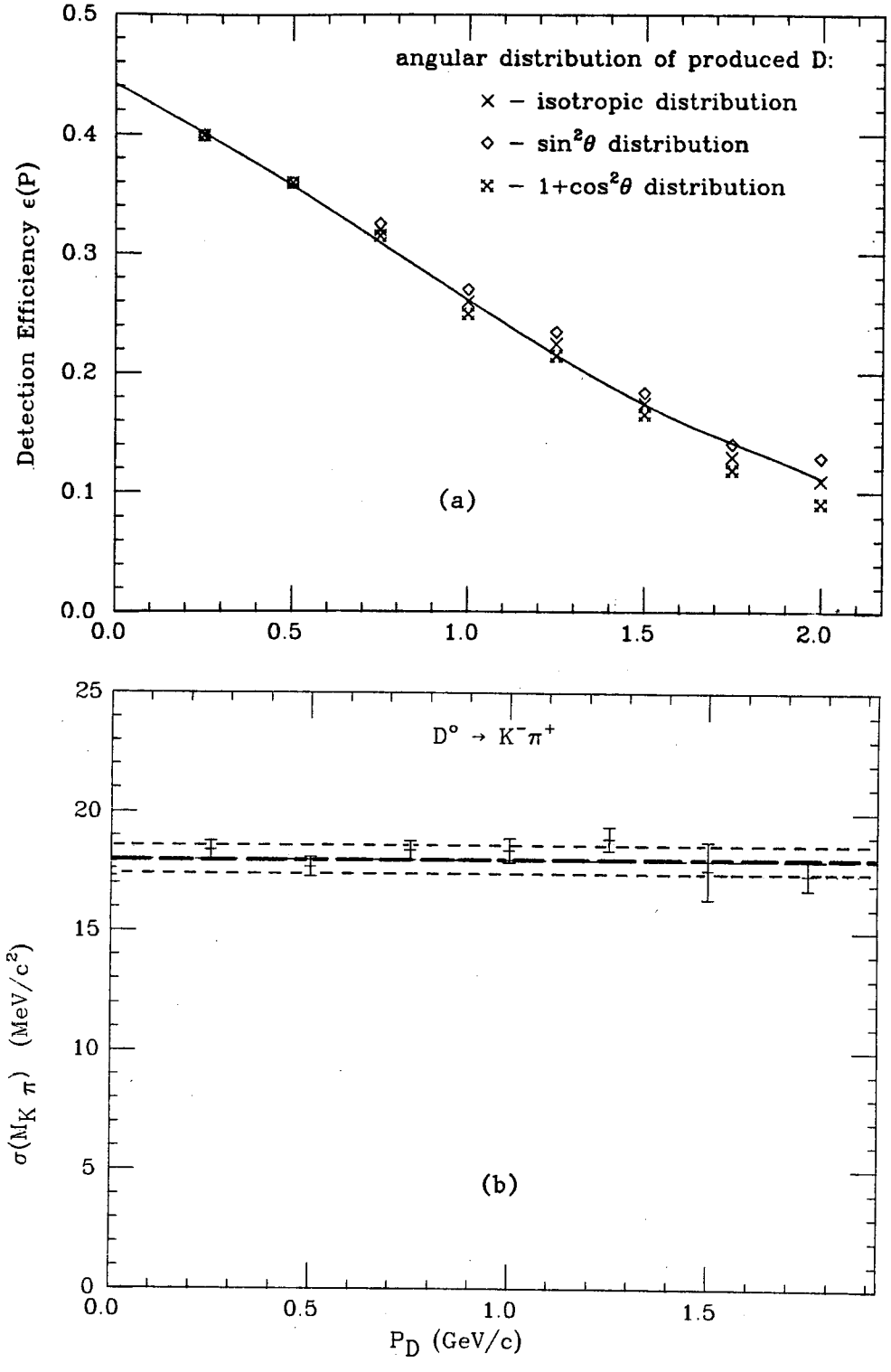

XBL 808-10908

figure 3.1
(a)- D^0 detection efficiency
(b)- width of $K^{\pm}\pi^{\mp}$ mass distribution.

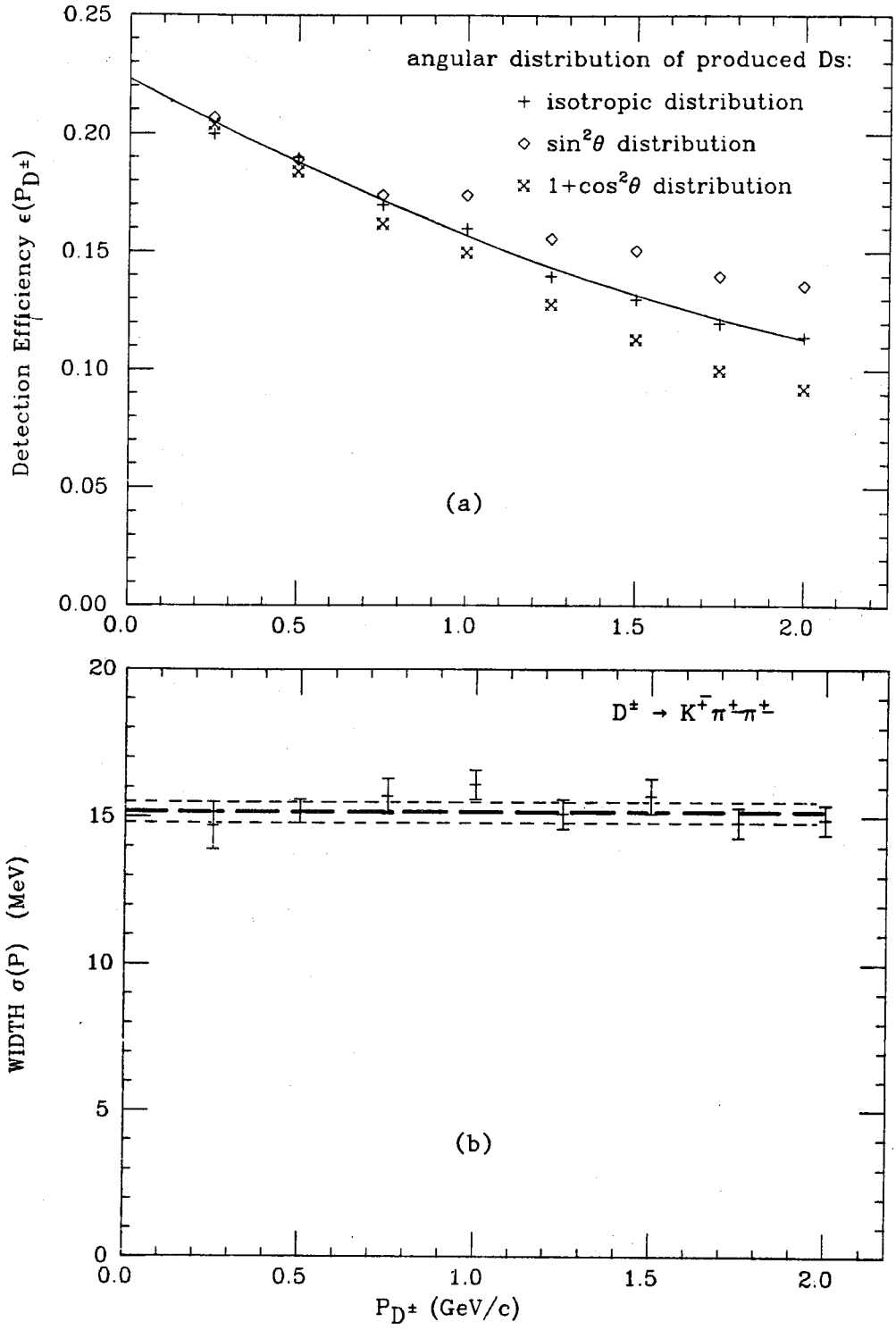

XBL 808-10898

figure 3.2
(a)- $D^{\pm}$ detection efficiency
(b)- width of $K^{\mp}\pi^{\pm}\pi^{\pm}$ mass distribution.

cuts on radial and z distance of closest approach and were not identified as electrons (by the liquid argon system for momenta above 300 MeV/c and by the TOF below 300 MeV/c) or muons (by the muon detector) were called pions. Exceptions were made only if the TOF weight to be called a K meson is greater than 0.5 or if the TOF weight to be called a proton or anti-proton exceeded 0.9. Thus many fast K mesons are misidentified as pions. This is a relatively safe selection rule on particle type because, above the resonance region, the production cross section of charged K mesons is only about one fourth of the pion production cross section[21] and the proton production cross section is only about one sixth of the pion cross section[22] The other reason the D^0 efficiency decreases more rapidly than does the D^+ efficiency is also a consequence of the two body D^0 decay. If the TOF resolution were infinitely good, the detection efficiency of a D would be limited by the solid angle coverage of the detector or by the cuts on solid angle made in the analysis of the data (in this case the solid angle used is 70% of 4 pi). For a decaying D^0 at rest, if the K^- is detected, the π^+ must also be detected because of the symmetry of the detector. If the D is moving, the K^- and π^+ need no longer be back to back tracks in the lab frame, thus allowing either the K^- or the π^+ to be missed. These are the effects responsible for the strong dependence of the detection efficiency for $D^0 \longrightarrow K^- \pi^+$ on the D momentum.

The effects of angular distribution in D production on the detection efficiency were also simulated by the monte carlo. Figures 3.1a and 3.2a (for neutral and charged D production respectively)

show the extreme cases of an angular distribution of the form

$$dN/d(\cos\theta) = 1 + a \cos^2\theta$$

with a equal to +1 and -1. A D momentum of 1.25 GeV/c corresponds to $D\bar{D}$ production at a center of mass energy of 4.5 GeV. These distributions change the detection efficiency from its value for isotropic production by less than 15% in the case of neutral D's decaying in the $K^- \pi^+$ mode, and by less than 20% for charged D's decaying in the $K^- \pi^+ \pi^+$ mode at this momentum. This is because the D is still moving fairly slowly (beta=0.56) so that the isotropic decay of the D into a K meson and one or two pions in its rest frame is still relatively isotropic in the lab frame. The error made in assuming a detection efficiency based on an isotropic angular distribution of produced D's above 1.25 GeV/c turned out not to be so serious. Fortunately, at center of mass energies above 4.5 GeV, most of the D production was found to occur at low momenta where the dependence of the detection efficiency on the angular distribution is small. In every center of mass energy region, however, the difference between the isotropic distribution detection efficiency and the detection efficiency determined for a $\sin^2\theta$ angular distribution was used in calculating the uncertainty on the total number of D's produced.

The number of D^0's produced at a particular center of mass energy was determined by taking all events with oppositely charged K mesons and pions and histogramming in two dimensions the sum of the pi and K meson momenta versus the $K\pi$ invariant mass. The invariant mass distribution of all events with a momentum sum in a particular

range was then fit to a Gaussian distribution plus a quadratic background, where the center of the Gaussian was fixed at the D^0 mass and the width was fixed using the results of monte carlo simulation (as shown in figure 3.1b for neutral D's and 3.2b for charged D's). The fitting function's width was allowed to vary by plus or minus one standard deviation from the monte carlo estimate for the distribution's width. This is the band enclosed by the parallel dotted lines shown in figures 3.1b and 3.2b for neutral and charged D's respectively). The number of events producing a D^0 of a given momentum was determined by dividing the number of events in the Gaussian by the detection efficiency corresponding to that particular momentum bin. The sum of all these produced events divided by the integrated luminosity of the data sample gave the product of the inclusive D^0 cross section and branching ratio at that particular energy. Another possible source of error in this product, in addition to the one brought about by assuming an isotropic production distribution, is the variation of the detection efficiency over the range of each individual momentum bin. This error was estimated as the difference in detection efficiency at the high edge and low edge of the momentum bin divided by $\sqrt{12}$. An identical analysis was performed using the decay of a charged D into a charged K meson and two charged pions. Examples of these fits are shown in chapter 5, figures 5.4 and 5.5.

To obtain the cross sections alone, rather than the products of cross section and branching ratio, the branching ratios determined by the Mark II collaboration for $D^0 \rightarrow K^- \pi^+$ and $D^+ \rightarrow k^- \pi^+ \pi^+$ were used[17] These values, obtained from studies of the psi(3770) decay,

are

decay mode	branching ratio
$D^0 \rightarrow K^-\pi^+$	$.028 \pm .006$
$D^+ \rightarrow K^-\pi^+\pi^+$	$.052 \pm .011$

The error on the measurement of these branching ratios produces a systematic error in the charged and neutral production cross sections of roughly 20%.

3.2 Results: R_D

Following the technique described, the production cross section for neutral and charged D's was investigated as a function of center of mass energy. The quantity R_D is formulated in analogy to R, the ratio of the hadron to muon pair cross section, as

$$\frac{\sigma_0 + \sigma_+}{2\sigma_{\mu\mu}}$$

where σ_0 is the inclusive neutral D cross section and σ_+ is the inclusive charged D cross section. The factor of two accounts for the fact that charmed particles are produced in pairs in e^+e^- annihilation.

The results of this combined analysis are given in table 3.1 and figure 3.3. Figure 3.4 compares the structure of R (as measured by the Mark II) and the structure of R_D. The same features which are visible in R at a center of mass energy just above 4 GeV are also

Number of D's Detected

Energy	Lum (nb^{-1})	$D^{\pm}$	D^0	$\sigma_{\pm}$ (nb)	σ_0 (nb)	R_D
3.88-4.02	374	18±9	23±6	4.8±2.5	5.9±1.5	1.0±.3
4.02-4.15	906	41±12	152±15	4.7±1.3	16.2±1.7	2.0±.2
4.16	1248	42±12	128±14	3.6±1.1	10.6±0.2	1.4±.2
4.15-4.20	342	17±7	45±8	5.3±2.3	14.0±2.5	1.9±.3
4.20-4.30	672	25±9	40±10	4.6±1.2	6.6±1.5	1.2±.2
4.30-4.40	221	26±8	19±9	13.0±4.1	10.5±4.5	2.5±.7
4.40-4.42	1315	54±16	160±18	4.6±1.4	13.7±1.7	2.1±.2
4.50-4.85	1565	65±17	65±15	4.6±1.2	4.9±1.1	1.2±.2
4.85-5.20	1655	57±18	74±17	4.3±1.3	6.4±1.5	1.5±.3
5.20	5110	118±33	241±31	2.9±0.8	6.6±0.9	1.5±.2
5.20-6.0	753	$8\pm^{12}_{4}$	30±10	$1.6\pm^{1.8}_{.8}$	6.5±1.9	$1.4\pm^{.5}_{.4}$
6.50-6.70	3650	44±16	54±17	1.9±0.6	2.6±0.8	1.1±.2
7.4	932	$11\pm^{8}_{6}$	$2\pm^{7}_{2}$	$1.6\pm^{1.1}_{.9}$	$0.3\pm^{1.0}_{0.3}$	$0.6\pm^{.5}_{.3}$

Table 3.1

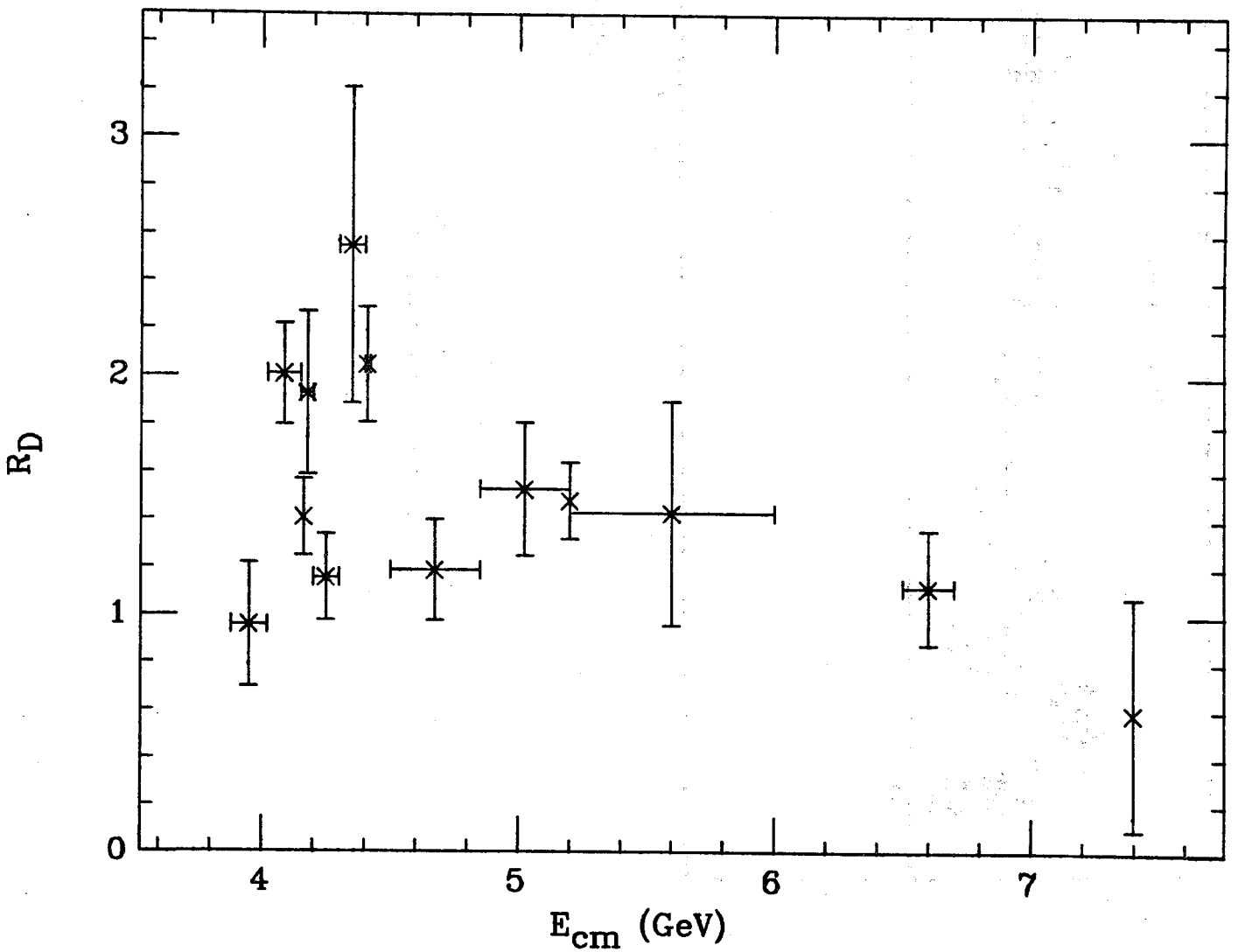

XBL 808-10914

figure 3.3

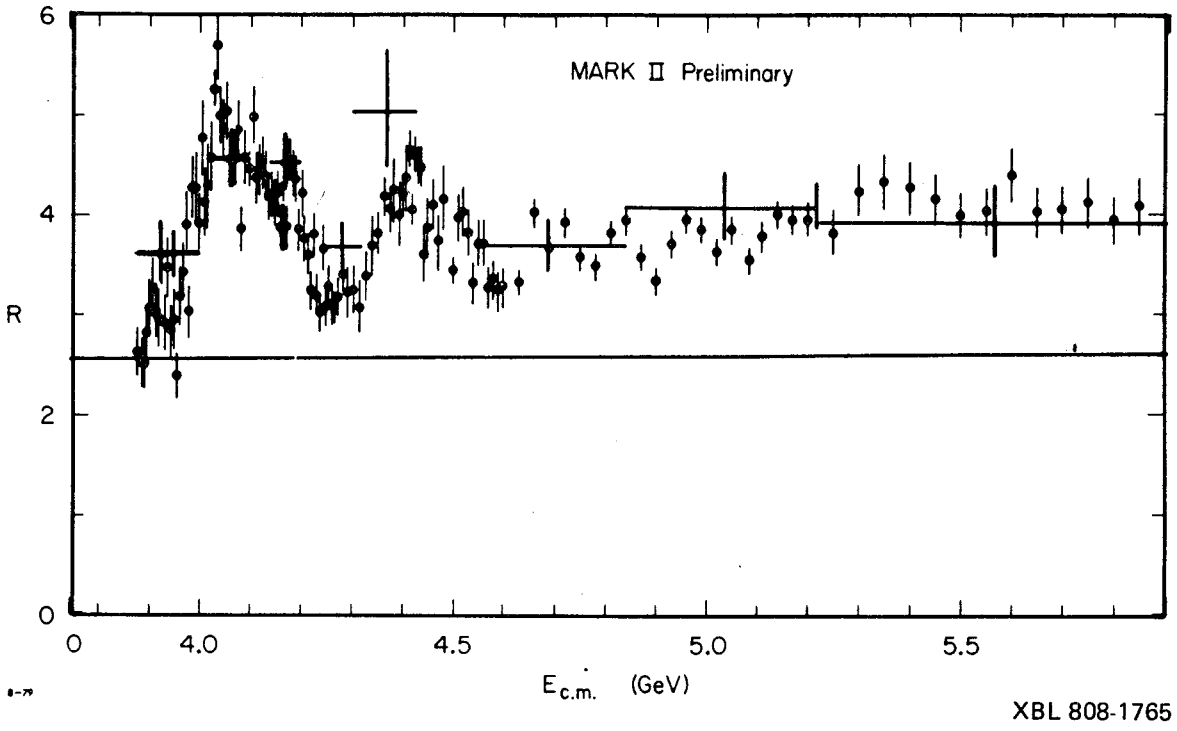

figure 3.4

2.5 units have been added to R_D (the approximate value of R below 3 GeV).

present in R_D.[23] for instance, the increases in R near 4.0 and 4.4 GeV, separated by a dip in R near 4.3 GeV, are also features of R_D. (The agreement between the two is quite good. As shown, R_D agrees well with the directly measured R). One should bear in mind the roughly 20% systematic errors on R_D (due to the uncertainty in the D decay branching ratios) which are not shown on the plot. Can R_D explain the total observed variation in R? Near 4 GeV there is room for the fugitive F, while above 5 GeV charmed baryon production can be accommodated, particularly in light of the 20% systematic errors on R_D24. Figures 3.5a and 3.5b make similar comparisons, showing R_D overplotted with the R measurements of the PLUTO[25] and DASP[26] detectors. Figure 3.6a makes a similar comparison between R_D and R_c (where R_c is the total increase in R due to charm production measured by the DELCO collaboration.[27]) The agreement is again good between the prominent features of R_c and the corresponding values of R_D. (One must conclude that the behavior of R_D explains the features of the energy dependence of R). The Mark II data for R_D are also in good agreement with the results of the Lead Glass Wall experiment[21] Their results are compared to the Mark II measurement in figure 3.6b.

A number of attempts have been made at explaining the structure observed in R_D[28] by considering a quark-antiquark interaction of the form V(r) where r is the relative separation of the quark antiquark pair. This potential is hypothesized to be responsible for the relative masses of the members of the psi family and also the source of the structure in R_D observed near 4 GeV. The most ambitious calculations within this framework have been performed by Eichten et al.,[29]

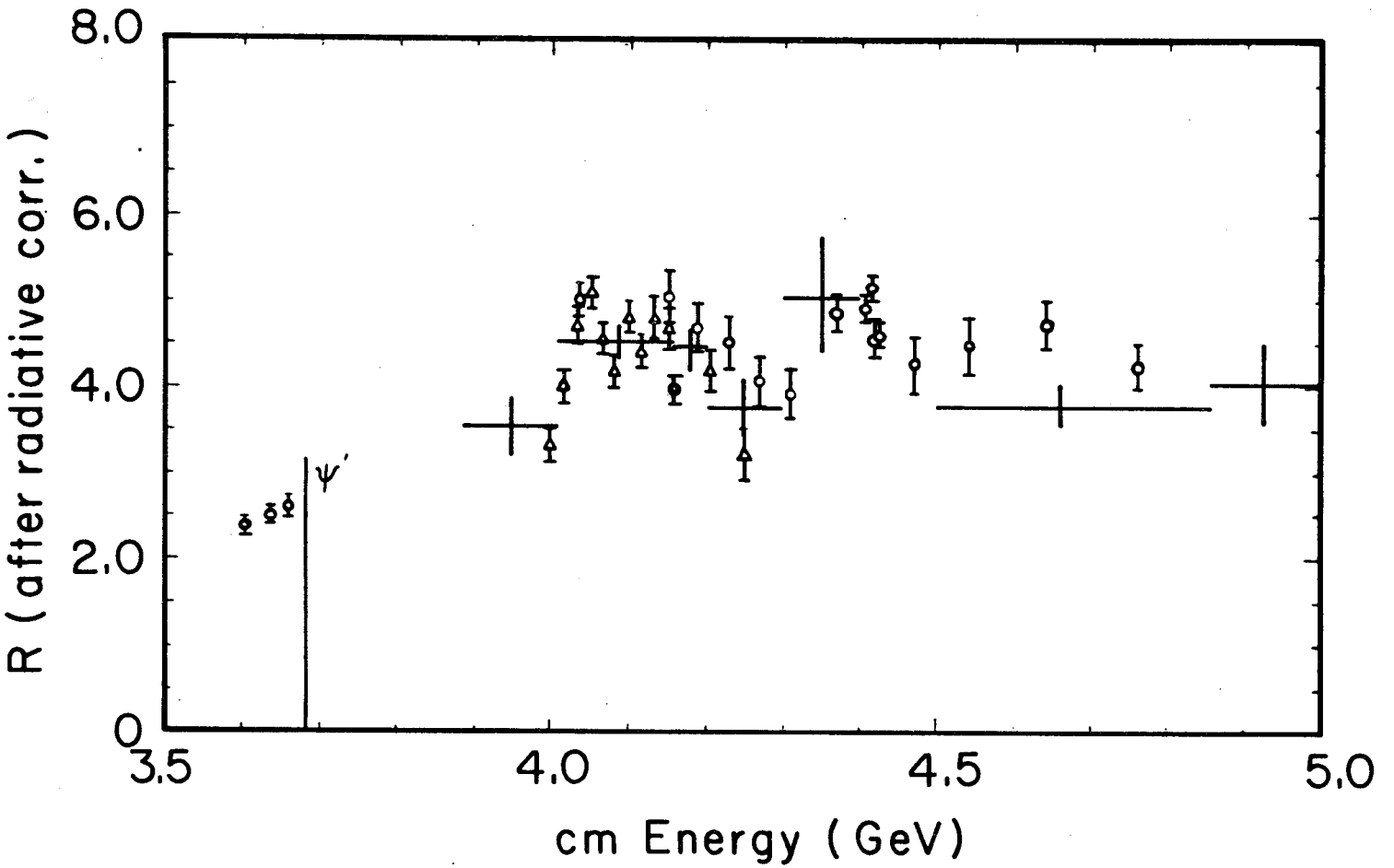

XBL 808-1759

figure 3.5a

The ratio $R = \sigma_{had}/\sigma_{\mu\mu}$ (allowing for radiative corrections) vs CMS energy.

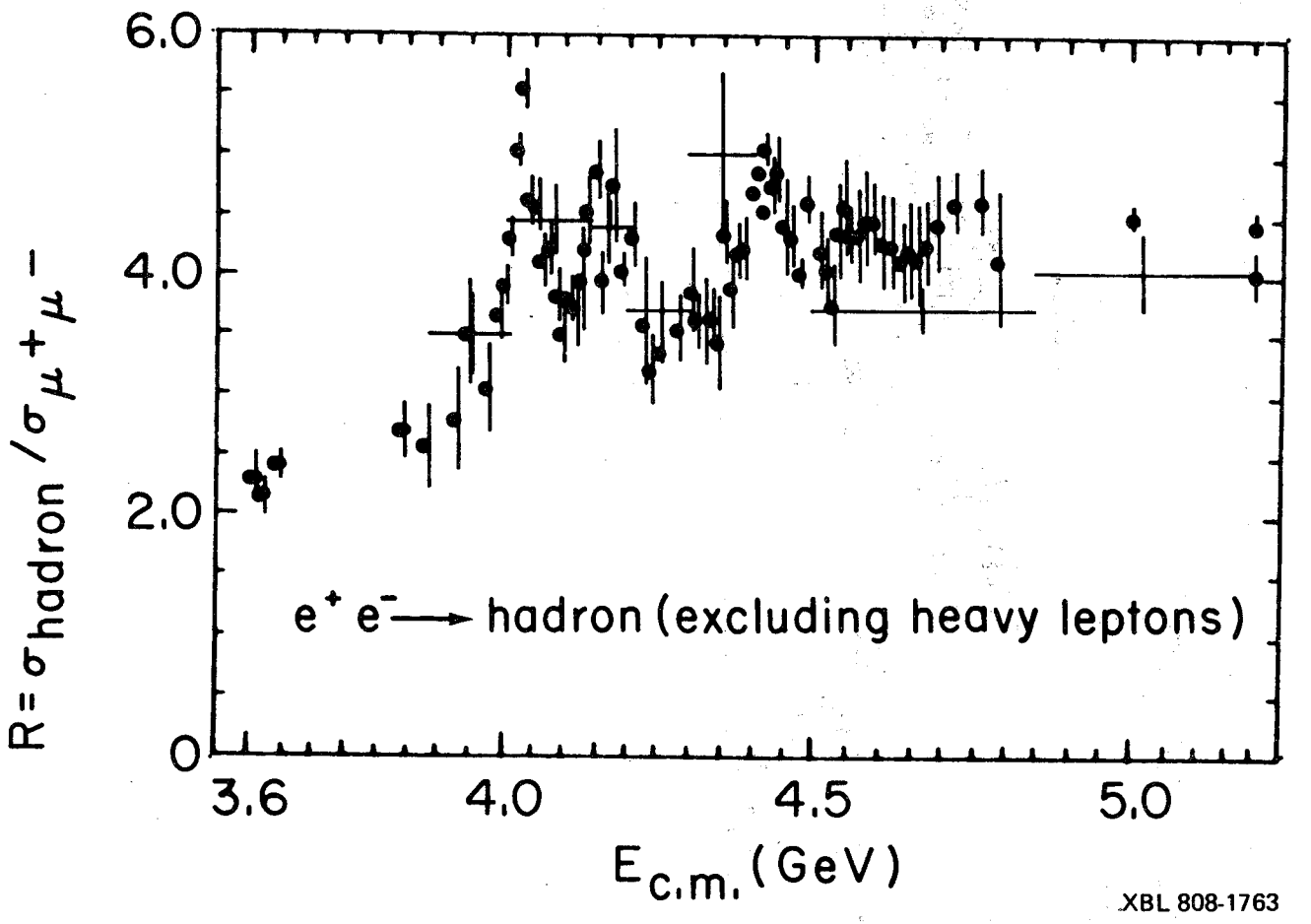
6.0
4.0
2.0
0
3.6
4.0
4.5
5.0
$R = \sigma_{hadron} / \sigma_{\mu^+\mu^-}$
$E_{c.m.}$ (GeV)
$e^+ e^- \longrightarrow$ hadron (excluding heavy leptons)
XBL 808-1763

figure 3.5b

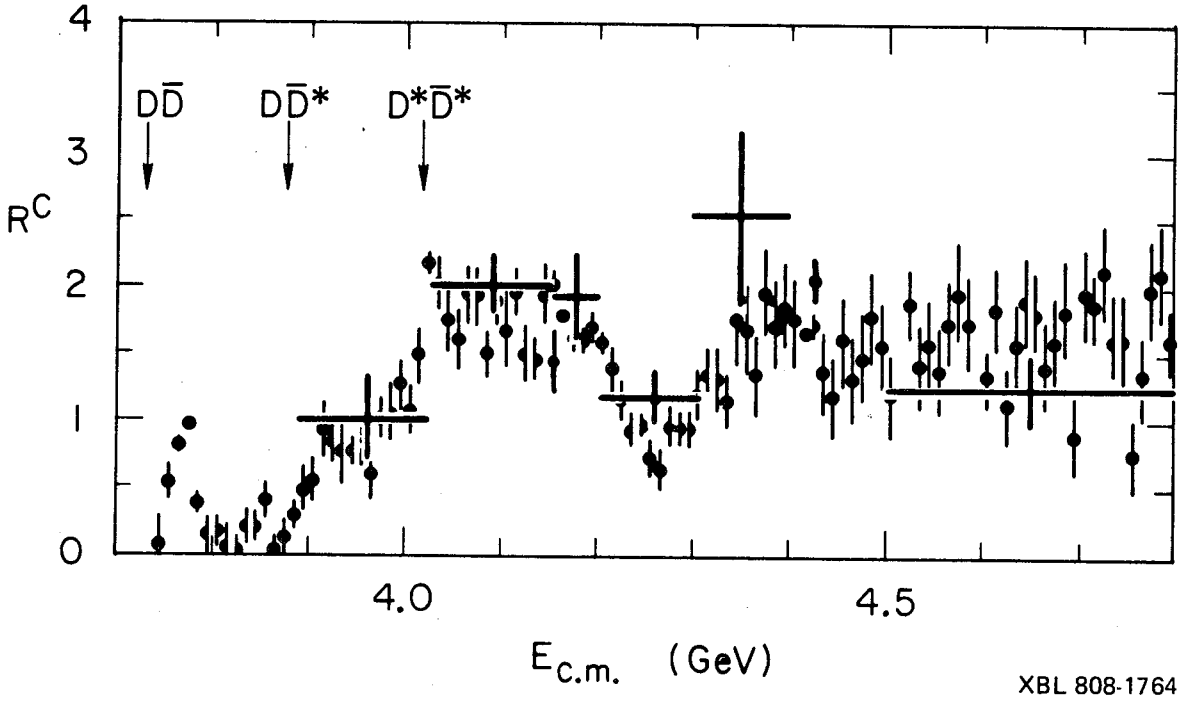

figure 3.6a

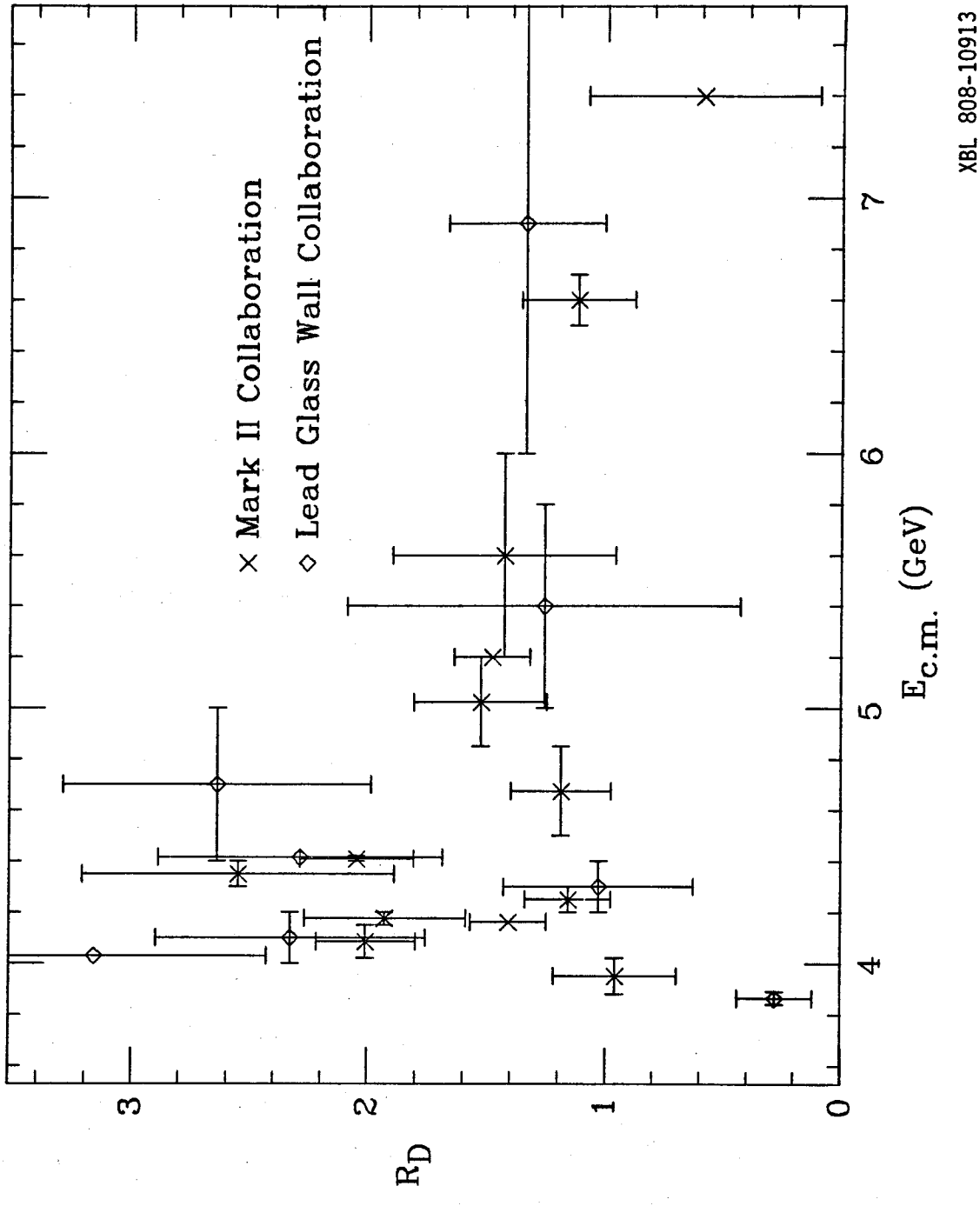

XBL 808-10913

figure 3.6(b)

who consider a potential of the form[30]

$$V(r) = -k/r + r/a^2$$

The potential has a coulomb term as well as a linear term, the latter responsible for the confinement of the quark within the hadron. The potential is not derivable from a more general QCD approach but rather is an attempt to phenomenologically parameterize a feasible form of the interaction.

Since the potential describes quark binding, it should describe the spectrum of masses occurring within the the psi family. Solving the Schroedinger equation with V(r) and adjusting k, a, and m_c (m_c is the charmed quark mass) to fit this spectrum specifies the potential numerically. In this regard the approach has had striking success in predicting the mass of the psi(3772) using the masses of the psi, psi′, and chi states as input.[31]

Above the threshold for charm production, this potential should describe the process shown in figure 3.7. Only $c\bar{c}$ coupling to the photon is considered in this model. (This is hypothesized to be the dominant production mechanism for charm at center of mass energies in the few GeV range.[32] Any charm production from the sea is neglected. (The allowed decay products are the D* and D since $s\bar{s}$ production from the sea is assumed to be very small relative to $u\bar{u}$ and $d\bar{d}$ production). The prediction of this model for ΔR is shown in figure 3.8 as a function of center of mass energy, superposed with the Mark II results (the figure is figure 13 of Eichten et al., ref. 29). The

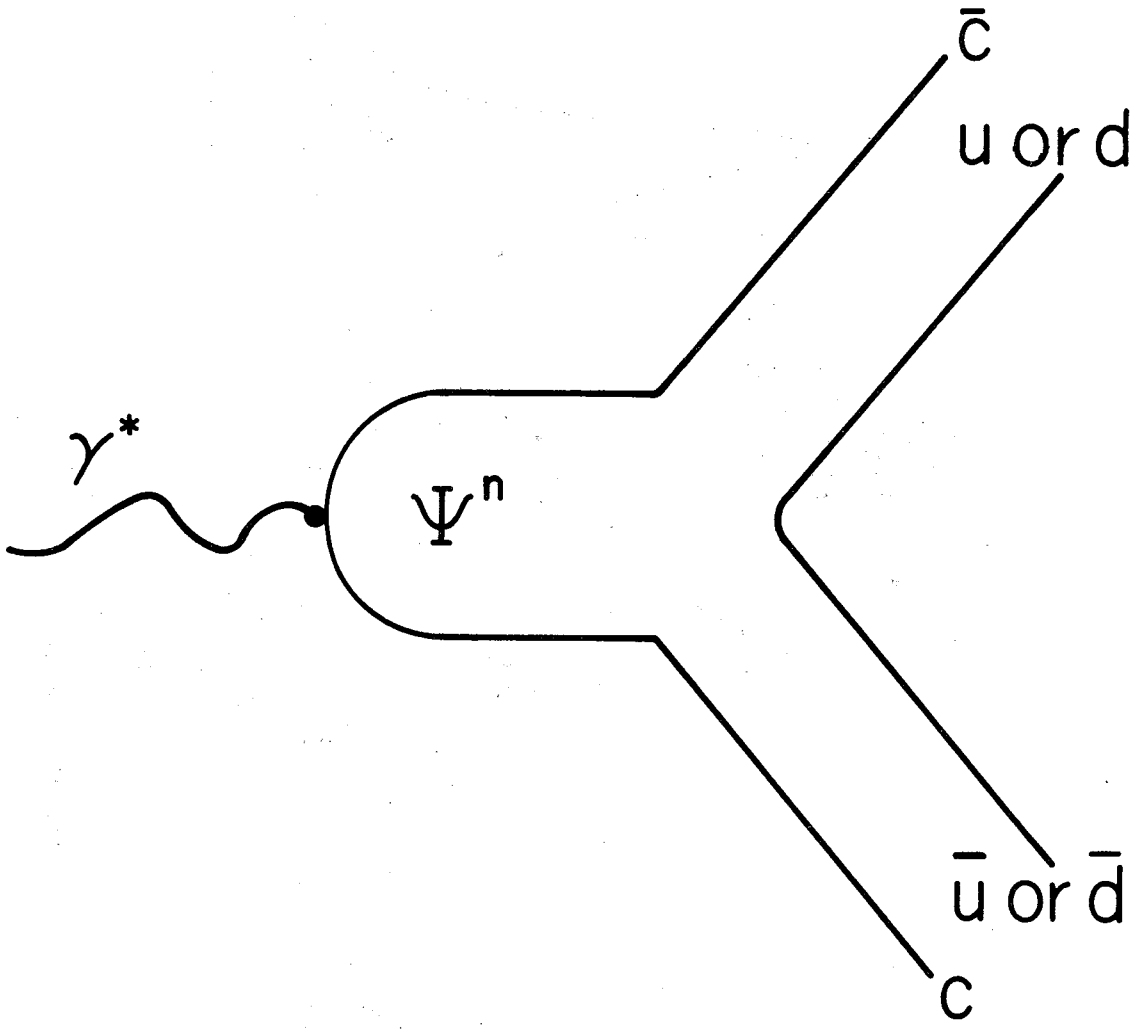

XBL-807-1689

figure 3.7

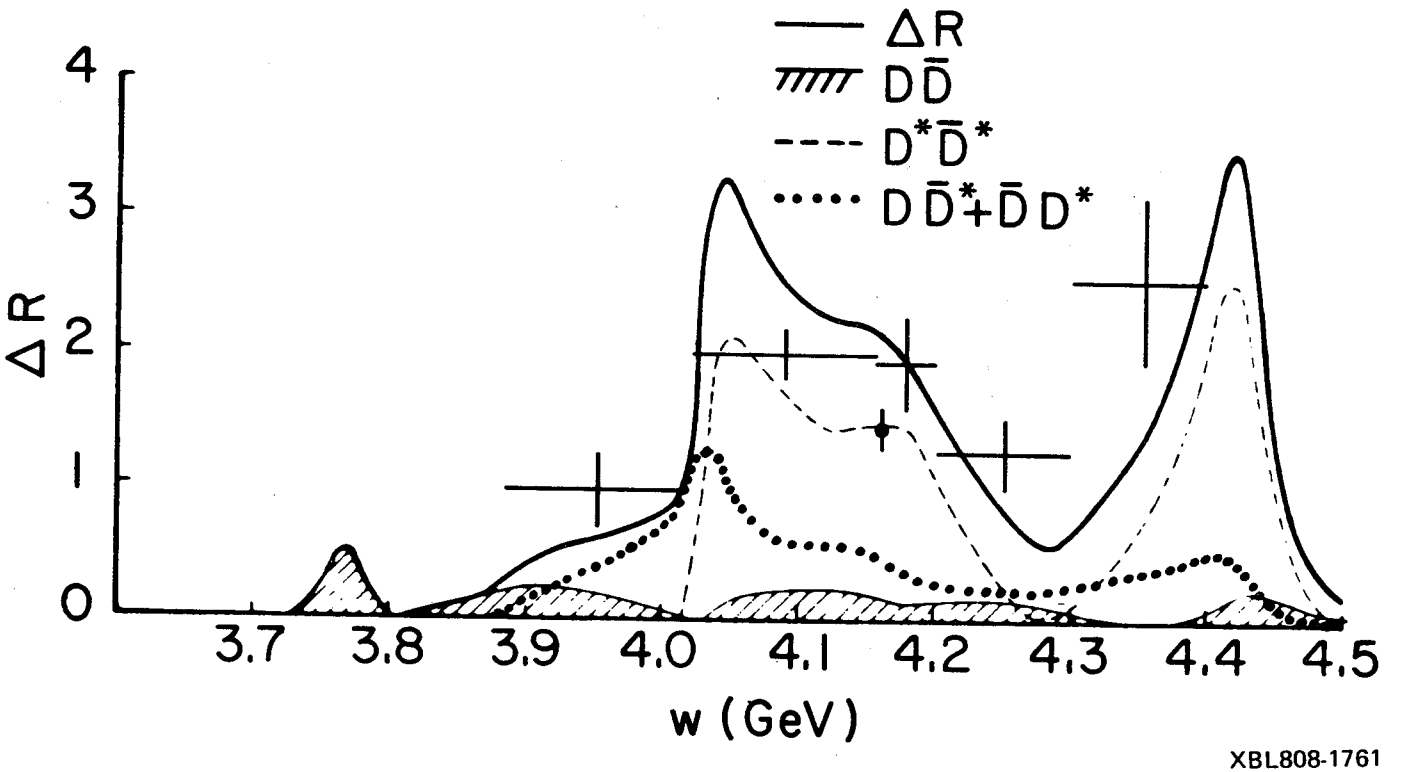

figure 3.8

R_D (Mark II) compared to a potential model: $v(r) = \frac{-k}{r} + \frac{r}{a^2}$

qualitative features of the prediction are in reasonable agreement with the observed data and the relative magnitudes of the prediction and the data are generally consistent, although the model predicts values of R_D at 4.0 and 4.4 GeV which are higher than those observed. Additional aspects of this model will be discussed in chapter 4.

3.3 The Ratio of Charged to Neutral D Production as a Function of Center of Mass Energy

Another feature of the potential model formalism is that it provides a prediction for the relative ratios of the reactions:

(1) $e^+e^- \rightarrow D\bar{D}$

(2) $e^+e^- \rightarrow D^*\bar{D}$ or $D\bar{D}^*$

(3) $e^+e^- \rightarrow D^*\bar{D}^*$

in the center of mass energy region from charm threshold to 4.3 GeV. The relative ratios of these reactions are calculated to be dependent on the center of mass energy. In fact, one of the principle reasons for formulating such models was in an attempt to explain why charm production was so nearly all $D^*\ \bar{D}^*$ at 4.03 GeV center of mass energy, a surprising result so close to threshold[12] If the relative ratios of the above reactions do change with center of mass energy, then there must be a change in the ratio of charged to neutral D production. This change should occur because the D^{*+} decays roughly 60% of the time into a D^0, while a D^{*0} never decays into a D^+. Therefore the ratio of charged to neutral D production should increase in regions

of center of mass energy where reaction (3) is suppressed.

Figure 3.9 shows this ratio. The statistical error is unfortunately quite large, but is consistent with a constant ratio. For comparison, similar results from the Lead Glass Wall collaboration[33] are also shown in the figure. The large statistical error of these results necessitates the formulation of a more sophisticated technique for deducing the relative ratios and center of mass energy dependence of reactions (1), (2), and (3). The development of this technique is the subject of the next chapter.

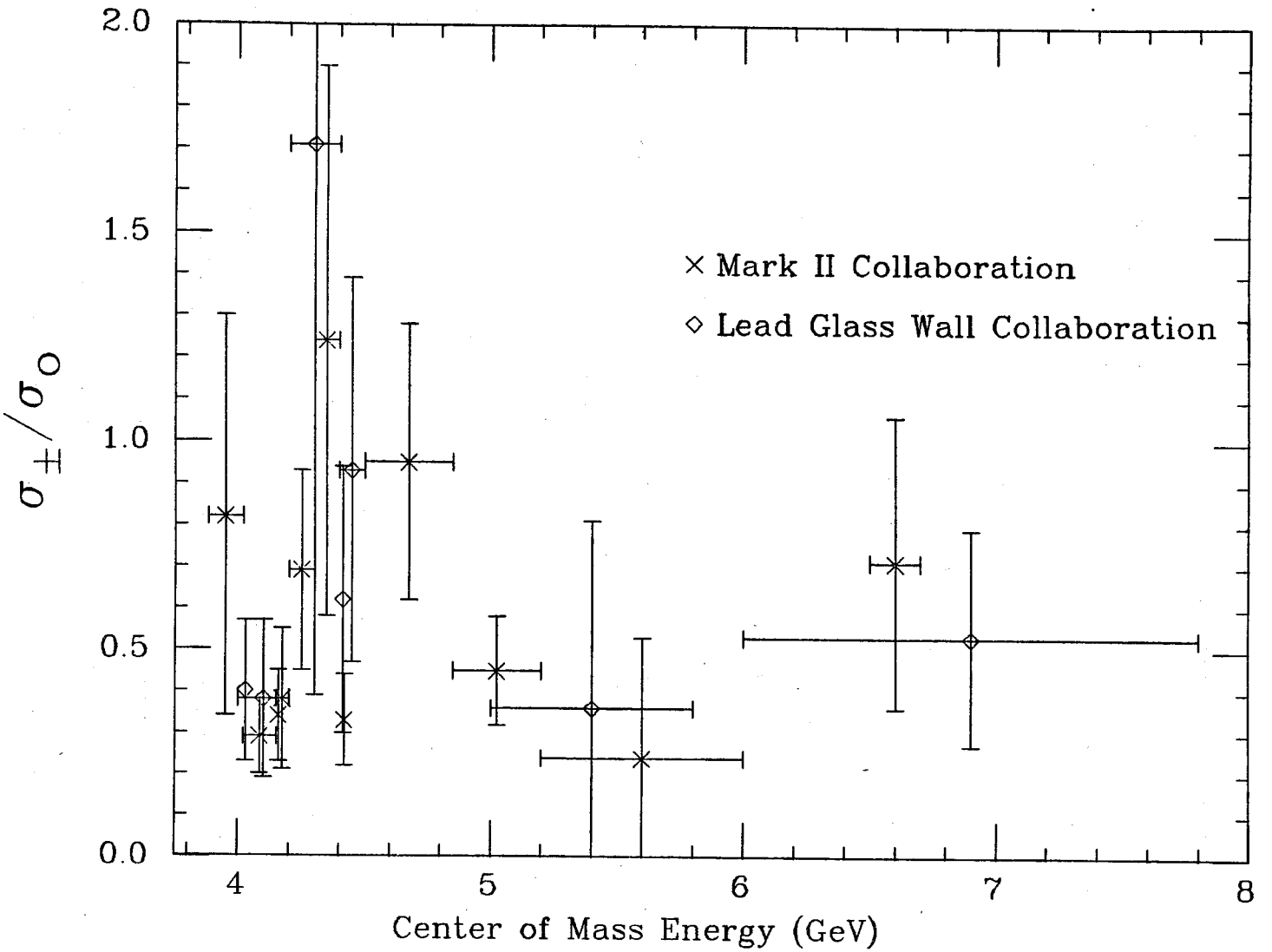

XBL 808-10911

figure 3.9

Chapter 4: D Meson Production in the Resonance Region

A topic of interest in the center of mass energy region between approximately 4 and 4.4 GeV is the relative production ratios of the three reactions:

(1) $e^+e^- \rightarrow D\bar{D}$

(2) $e^+e^- \rightarrow D^*\bar{D}$ or $\bar{D}^*D$

(3) $e^+e^- \rightarrow D^*\bar{D}^*$

Evidence that all three reactions occur at 4.16 GeV is shown in figures 4.1a and 4.1b where the effective masses recoiling against both charged and neutral D mesons are shown. The "signal" near 1.86 GeV/c^2 is due to reaction (1), the signal at and around 2.0 GeV/c^2 is from reaction (2), and the signal near 2.16 GeV/c^2 is due to reaction (3).

It is not possible in this center of mass energy region (around 4 GeV) to detect D*'s directly. The decay of a D* into a D meson and a photon or pion produces these particles at an energy too low to be detected by the Mark II detector. The pion is produced with a momentum of only 40 MeV/c so that the solenoidal magnetic field in the drift chamber prevents the pion from traversing enough drift chamber layers to be tracked. The photon produced in D* decays has an energy of only about 140 MeV in the D* rest frame. The probability of detection of a photon with an energy that low in the liquid argon shower counters is only about 15%, while the resolution error is roughly 320 MeV. This makes direct detection of D* radiative decays

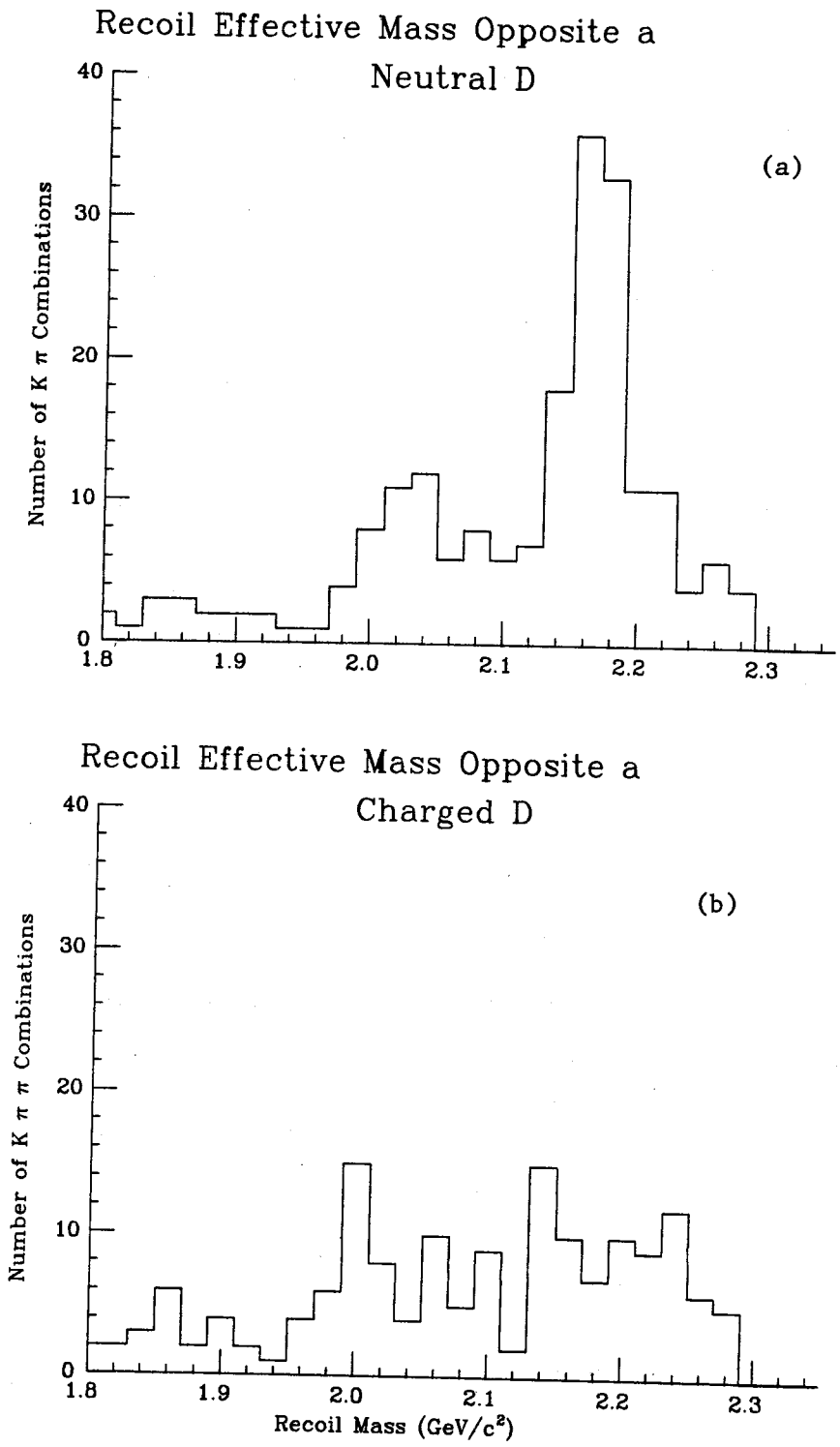
Recoil Effective Mass Opposite a
Neutral D
(a)
Number of K π Combinations
0
10
20
30
40
1.8
1.9
2.0
2.1
2.2
2.3
Recoil Effective Mass Opposite a
Charged D
(b)
Number of K π π Combinations
0
10
20
30
40
1.8
1.9
2.0
2.1
2.2
2.3
Recoil Mass (GeV/c²)
XBL 808-10906

figure 4.1

very hard to observe. Therefore, to establish quasi-two-body D* production one must detect the particles recoiling opposite the D*. The D* then shows up as a peak in effective recoil mass. To make a quantitative measurement of the relative ratios of the three reactions it is first necessary to develop an analytic framework to describe them. In the first section of this chapter, a method is developed which will aid in measuring the relative ratios of reactions (1), (2), and (3) when only a single D is detected.

4.1 The Kinematics of the Recoil Effective Mass

The recoil effective mass observed opposite a D in reaction (1) is a trivial case. The effective mass recoiling against a D meson is a delta function at the D mass convoluted with the momentum resolution of the Mark II detector. Reaction (2) contains a trivial part also; when the D* recoils against a detected D. A less straightforward event occurs when the detected D comes from the decay of a produced D* and the recoil effective mass is due to the directly produced D combined with the other products of the D* decay. This latter occurrence is always the case for reaction (3) where all detected D mesons are the result of prior D* decays.

The case where the D is produced as a result of D* decay in quasi-two-body production will now be discussed in some detail. Consider a reaction of the form

$$e^+e^- \rightarrow D^*\bar{D} \rightarrow D\bar{D}\pi.$$

The effective recoil mass observed opposite the D is

$$m^2_{\overline{D}\pi} = m^2_{\overline{D}} + m^2_{\pi} + 2(E_{\overline{D}}E_{\pi} - p_{\overline{D}}p_{\pi}\cos\theta) \tag{4.1}$$

where the variables are defined in figure 4.2. Primed (′) variables refer to the D* rest frame. Since the decay of the D* is two body, the four-momenta of the D and π are easily determined in the D* rest frame. In the lab frame they are:

$$p_{\pi}\cos\theta = \gamma p'_{\pi}\cos\theta' + \beta\gamma E_{\pi}'$$

$$E_{\pi} = \gamma E_{\pi}' + \beta\gamma p_{\pi}'\cos\theta'$$

where

$$\gamma = \frac{E_{D*}}{M_{D*}}$$

and

$$\beta = \frac{p_{D*}}{E_{D*}}$$

Using these definitions:

$$m^2_{\overline{D}\pi} = m^2_{\overline{D}} + m^2_{\pi} + 2[E_{\overline{D}}\,(E_{\pi}' - \beta p_{\pi}'\cos\theta)$$

$$+ p_{\overline{D}}(p_{\pi}'\cos\theta' - \beta E_{\pi}')]\gamma \tag{4.2}$$

Since equation 4.2 depends on $\cos\theta'$, it is useful to obtain an expression for $dN/dM^2_{\overline{D}\pi}$ in terms of $dN/d(\cos\theta')$. Using equation 4.2, the range of effective $\overline{D}\pi$ mass can be easily determined.

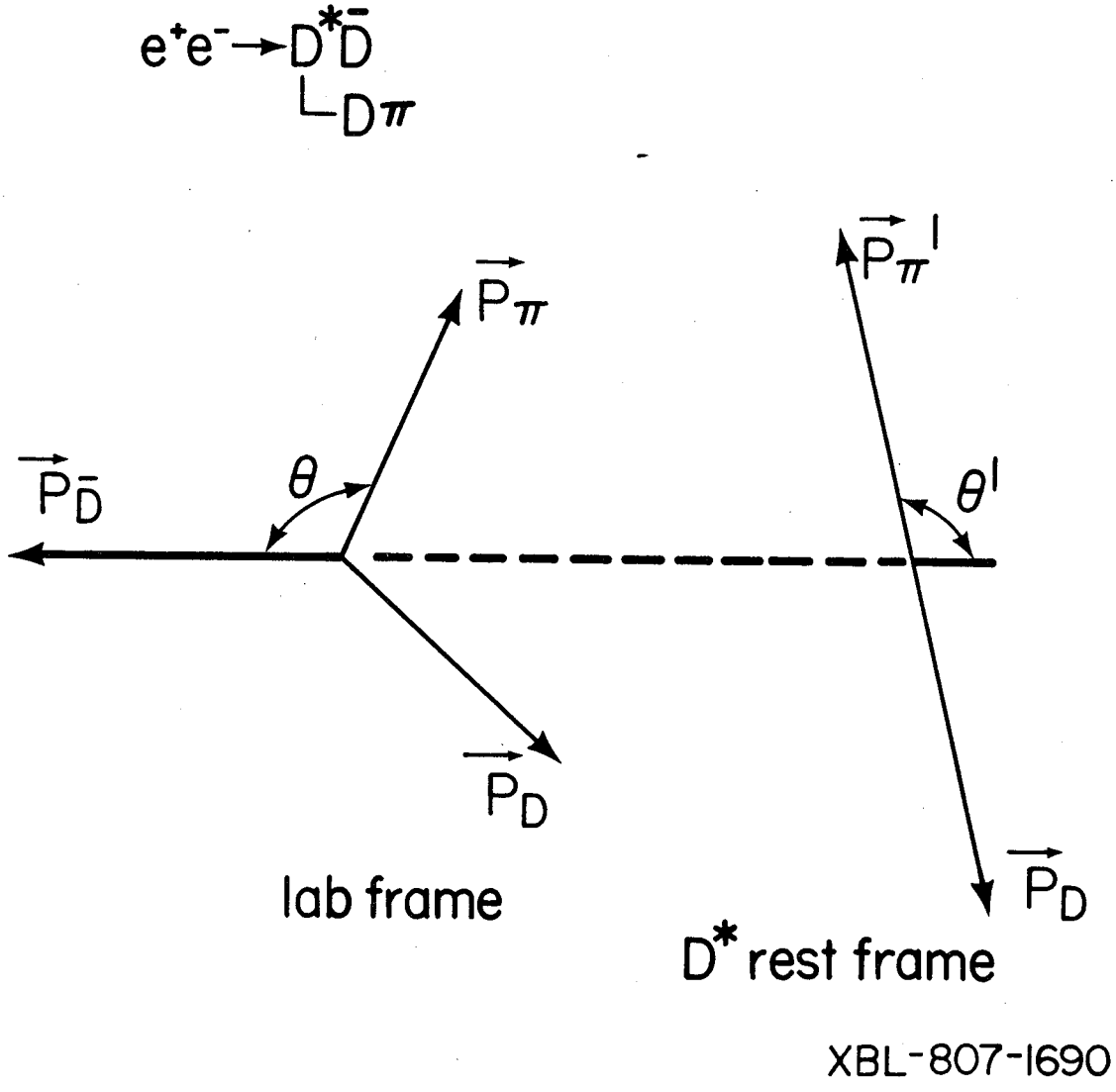
$e^+e^- \to D^*\bar{D}$
$\hookrightarrow D\pi$
$\vec{P}_\pi$
$\vec{P}_{\bar{D}}$
θ
$\vec{P}_D$
lab frame
$\vec{P}_\pi{}'$
θ'
$\vec{P}_D$
D^* rest frame
XBL-807-1690

figure 4.2

$$m^2_{\bar{D}\pi}(\max) = m^2_{\bar{D}} + m^2_{\pi} + 2\gamma p_{\pi}'(E_{\bar{D}} - p_{\bar{D}}) + 2\gamma E_{\pi}'(E_{\bar{D}} - \beta p_{\bar{D}}) \qquad (4.3)$$

$$m^2_{\bar{D}\pi}(\min) = m^2_{\bar{D}} + m^2_{\pi} - 2\gamma p_{\pi}'(E_{\bar{D}}\beta - p_{\bar{D}}) + 2\gamma E_{\pi}'(E_{\bar{D}} - \beta p_{\bar{D}}) \qquad (4.4)$$

Defining the new variables Σ and Δ as:

$$\Sigma = m^2_{\bar{D}\pi}(\max) + m^2_{\bar{D}\pi}(\min) \qquad (4.5)$$

$$\Delta = m^2_{\bar{D}\pi}(\max) - m^2_{\bar{D}\pi}(\min) \qquad (4.6)$$

gives equation 4.2 the simple form

$$m^2_{\bar{D}\pi} = \frac{(\Sigma + \Delta\cos\theta')}{2} \qquad (4.7)$$

This expression may now be used to solve for $dN/dM^2_{\bar{D}\pi}$, the recoil effective mass squared distribution observed opposite a detected D.

$$\frac{dN}{dm^2_{\bar{D}\pi}} = \frac{dN}{d(\cos\theta')}\,\frac{d(\cos\theta')}{dm^2_{\bar{D}\pi}} = \frac{2}{\Delta}\,\frac{dN}{d(\cos\theta')} \qquad (4.8)$$

Equation 4.8 shows how the observed recoil spectrum depends on the angular distribution of the decay products of the D*. This distribution must be an important ingredient in an analytic fit to the observed spectrum.

Equations 4.5 and 4.6 help in understanding the structure observed in figures 4.1a and 4.1b (the recoil mass distribution observed opposite detected neutral and charged D mesons). The peaks

at 2.0 GeV/c^2 and 2.16 GeV/c^2 are the result of reactions (2) and (3). It is the small difference between the D* mass and the D mass which causes the peaks to be so sharp. These ranges are tabulated for various modes of the D* decay in table 4.1 for a center of mass energy of 4.16 GeV. They show the recoil effective mass one would expect to observe when either reaction (2) or (3) occurs followed by D* decay into a D and either a photon or pion.

Equation 4.8 shows the need for an expression for $dN/d(\cos\theta)$. The next section considers the problem of formulating matrix elements for reactions (1), (2), and (3).

4.2 Matrix Elements for D and D* Production and Decay

In the case of $e^+e^- \rightarrow D\bar{D}$, the matrix element for the production process is

$$M_{D\bar{D}} \sim \vec{\eta} \cdot \vec{p} \tag{4.9}$$

where $\vec{\eta}$ is the virtual photon's polarization and $\vec{p}$ is the lab three-momentum of the D meson.[34] $\vec{\eta}$ obeys the relation

$$\sum_{\text{polarization}} \eta_i \eta_j = \delta_{ij} - n_i n_j \tag{4.10}$$

where $\vec{n}$ points along the beam line (chosen to be in the +z direction). In this equation, and in the rest of this section, only the directions of 3-vectors used are relevant to the development of matrix elements. Therefore, all vectors used are scaled to unit

$$e^+e^- \to D^*\bar{D} \quad \text{at 4.16 GeV}$$
$$\quad\;\; \hookrightarrow D + x$$

Recoil effective mass opposite the D

Decay mode	Minimum recoil mass (GeV)	Maximum recoil mass (GeV)
$D^{*0} \to D^0\pi^0$	2.01	2.08
$D^{*0} \to D^0\gamma$	1.93	2.14
$D^{*+} \to D^0\pi^+$	2.02	2.08
$D^{*+} \to D^+\pi^0$	2.02	2.08
$D^{*+} \to D^+\gamma$	1.93	2.14

$$e^+e^- \to D^*\bar{D}^*$$
$$\quad\;\; \hookrightarrow D + x$$

Recoil effective mass opposite the D

Decay mode	Minimum recoil mass (GeV)	Maximum recoil mass (GeV)
$D^{*0} \to D^0\pi^0$	2.14	2.19
$D^{*0} \to D^0\gamma$	2.09	2.23
$D^{*+} \to D^+\pi^0$	2.15	2.20
$D^{*+} \to D^0\pi^+$	2.15	2.19
$D^{*+} \to D^+\gamma$	2.09	2.23

Table 4.1

length.

In the case of $e^+e^- \rightarrow D^*\bar{D}$, assuming the conventional spin parity assignments for the D and D* of 0^- and 1^- respectively,[35] the production amplitude is

$$M_{D^*\bar{D}} \sim \vec{\eta}\cdot\vec{p}\times\vec{\varepsilon} \tag{4.11}$$

where $\vec{\varepsilon}$ is the D* polarization vector. $\vec{\varepsilon}$ obeys the relation

$$\sum_{pol} \varepsilon_i \varepsilon_j = \delta_{ij} \tag{4.12}$$

In the case of $e^+e^- \rightarrow D^* \bar{D}^*$, the situation is more complicated. Since the overall state must have a spin and parity of 1^-, three independent amplitudes are possible yielding a spin 0,P wave; a spin 2,P wave; and a spin 2,F wave state (a spin 1, P wave state would violate charge conjugation parity). The matrix element is

$$\begin{aligned} M_{D^*\bar{D}^*} = {} & A_1(\vec{\varepsilon}\cdot\vec{\bar{\varepsilon}})(\vec{p}\cdot\vec{\eta}) + A_2[\tfrac{1}{2}(\vec{\varepsilon}\cdot\vec{p})(\vec{\bar{\varepsilon}}\cdot\vec{\eta}) + \tfrac{1}{2}(\vec{\varepsilon}\cdot\vec{\eta})(\vec{\bar{\varepsilon}}\cdot\vec{p}) \\ & - \tfrac{1}{3}(\vec{\varepsilon}\cdot\vec{\bar{\varepsilon}})(\vec{p}\cdot\vec{\eta})] + A_3\ \{(\vec{p}\cdot\vec{\varepsilon})(\vec{p}\cdot\vec{\bar{\varepsilon}})(\vec{p}\cdot\vec{\eta}) \\ & - \tfrac{1}{5}[(\vec{\varepsilon}\cdot\vec{\bar{\varepsilon}})(\vec{p}\cdot\vec{\eta}) + (\vec{\bar{\varepsilon}}\cdot\vec{\eta})(\vec{\varepsilon}\cdot\vec{p}) + (\vec{\varepsilon}\cdot\vec{\eta})(\vec{\bar{\varepsilon}}\cdot\vec{p})]\} \end{aligned} \tag{4.13}$$

where A_1, A_2, and A_3 are the undetermined coefficients multiplying the three possible amplitudes.

In considering single particle distributions, where only the D is detected, it is necessary to formulate the joint production-decay amplitude for reactions (2) and (3). For D* decay with pion

emission, the decay amplitude is

$$M_{D^* \to D\pi} \sim \vec{\varepsilon} \cdot \vec{q} \tag{4.14}$$

where $\vec{q}$ is the D meson's three momentum in the D* rest frame. For D* decay with photon emission the amplitude is

$$M_{D^* \to D\pi} \sim \vec{\varepsilon} \cdot \vec{q} \times \vec{E} \sim \vec{\varepsilon} \cdot \vec{B} \tag{4.15}$$

where $\vec{E}$ is the photon's electric polarization vector and $\vec{B}$ is the photon's magnetic polarization vector. If the photon's polarization is unmeasured, $\vec{E}$ and $\vec{B}$ obey the relations

$$\sum_{\text{polarization}} E_i E_j = \sum_{\text{polarization}} B_i B_j = \delta_{ij} - q_i q_j$$

Equations 4.14 and 4.15 imply that in writing a joint production-decay amplitude $\vec{\varepsilon}$ may be replaced by $\vec{q}$ when a D* decays to a D and a pion. Similarly $\vec{\varepsilon}$ may be replaced by $\vec{B}$ when a D* decays to a D and a photon.

These variables now allow the calculation of $dN/d(\cos\theta')$, which is needed in equation 4.8. Consider first the case of

$$e^+e^- \to D^*\bar{D} \to D\pi\bar{D}$$

The joint production decay amplitude can be expressed using equations 4.13 and 4.10 as

$$|M|^2 \sim |\vec{n}\cdot\vec{p}\times\vec{q}|^2$$

Summing over the polarizations of the virtual photon

$$|M|^2 = \varepsilon_{ijk}\,\varepsilon_{lmn}\,(\delta_{il} - n_i n_l)p_j p_m q_k q_n$$

Since $\vec{n}$ points in the +z direction

$$|M|^2 = 1 - (\vec{p}\cdot\vec{q})^2 - (\vec{p}\times\vec{q})_z^2 \qquad (4.17)$$

Thus the relationship between the D and the D* directions of motion is dependent on the D* direction relative to the beam direction. A simple relationship does not exist for the distribution of D mesons relative to the parent D* meson's helicity axis. The situation is even uglier (as will soon be shown) for D* $\overline{D}$* production and decay. The underlying reason is that the quantum mechanical amplitude for D* $\overline{D}$* production and decay describes the entire event. Thus the D* decay and the $\overline{D}$* decay are correlated. Since the D* direction is not measured when the detected D is a result of D* decay, the D* direction relative to the beam axis is averaged over. This is equivalent to letting $\vec{n}$ be a random direction. Equation 4.17 then is

$$|M|^2 \sim 1 - (\vec{p}\cdot\vec{q})^2 \qquad (4.18)$$

The case of D* decay with the emission of a photon can be treated in a similar manner. With the aid of equations 4.11 and 4.15, the joint production-decay matrix element is:

$$|M|^2 \sim |\vec{\eta}\cdot\vec{p}\times\vec{B}|^2 \tag{4.19}$$

Summing over the virtual photon polarization and averaging over the beam direction, as before, equation 4.19 becomes

$$|M|^2 \sim [\delta_{jm}\delta_{kn} - \delta_{jn}\delta_{Km}]P_j P_m B_K B_n \tag{4.20}$$

Since the polarization of the D* decay produced photon is also unobserved, the polarization vector B can also be summed over using equation 4.15 to give

$$|M|^2 \sim 1 + (p\cdot q)^2 \tag{4.21}$$

The same technique may be used in studying reaction (3). Consider first the case of the reaction:

$$e^+e^- \rightarrow D\bar{D}\pi\pi$$

Using equations 4.13 and 4.14, the amplitude for this reaction is:

$$\begin{aligned} M_{D^*\bar{D}^*} = {} & A_1(\vec{q}\cdot\vec{\bar{q}})(\vec{p}\cdot\vec{\eta}) + A_2[\tfrac{1}{2}(\vec{q}\cdot\vec{p})(\vec{\bar{q}}\cdot\vec{\eta}) + \tfrac{1}{2}(\vec{q}\cdot\vec{\eta})(\vec{\bar{q}}\cdot\vec{p}) \\ & - \tfrac{1}{3}(\vec{q}\cdot\vec{\bar{q}})(\vec{p}\cdot\vec{\eta})] + A_3\{(\vec{p}\cdot\vec{q})(\vec{p}\cdot\vec{\bar{q}})(\vec{p}\cdot\vec{\eta}) \\ & - \tfrac{1}{5}[(\vec{q}\cdot\vec{\bar{q}})(\vec{p}\cdot\vec{\eta}) + (\vec{\bar{q}}\cdot\vec{\eta})(\vec{q}\cdot\vec{p}) + (\vec{q}\cdot\vec{\eta})(\vec{\bar{q}}\cdot\vec{p})]\} \end{aligned} \tag{4.22}$$

Since the data relevant to this analysis is at a center of mass energy near 4.16 GeV, the F wave amplitude is assumed to be small relative to the two P wave amplitudes. The coefficient A_3 will be

taken as zero for the rest of this analysis. Equation 4.22 is rewritten as

$$M_{D^*\bar{D}^*} = \lambda_1(\vec{q}\cdot\vec{\bar{q}})(\vec{p}\cdot\vec{\eta}) + \lambda_2[(\vec{q}\cdot\vec{p})(\vec{\bar{q}}\cdot\vec{\eta}) + (\vec{q}\cdot\vec{\eta})(\vec{\bar{q}}\cdot\vec{p})] \tag{4.23}$$

where

$$\lambda_1 = A_1 - \frac{A_2}{3} \tag{4.24}$$

and

$$\lambda_2 = \frac{A_2}{2} \tag{4.25}$$

The square of the magnitude of the matrix element becomes:

$$\begin{aligned}|M_{D^*\bar{D}^*}|^2 = {} & |\lambda_1|^2(\vec{q}\cdot\vec{\bar{q}})^2(\vec{p}\cdot\vec{\eta})^2 + |\lambda_2|^2\{(\vec{q}\cdot\vec{p})^2(\vec{\bar{q}}\cdot\vec{\eta})^2 + (\vec{q}\cdot\vec{\eta})^2(\vec{\bar{q}}\cdot\vec{\eta})^2 \\ & + 2(\vec{q}\cdot\vec{p})(\vec{\bar{q}}\cdot\vec{\eta})(\vec{q}\cdot\vec{\eta})(\vec{\bar{q}}\cdot\vec{p})\} + 2\mathrm{Re}\lambda_1\lambda_2^*\{(\vec{q}\cdot\vec{\bar{q}})(\vec{p}\cdot\vec{\eta})(\vec{q}\cdot\vec{p})(\vec{\bar{q}}\cdot\vec{\eta}) \\ & + (\vec{q}\cdot\vec{\bar{q}})(\vec{p}\cdot\vec{\eta})(\vec{q}\cdot\vec{\eta})(\vec{\bar{q}}\cdot\vec{p})\}\end{aligned} \tag{4.26}$$

As before, averaging over everything but the angle between the D* momentum vector and the momentum vector of its decay produced D gives

$$|M_{D^*\bar{D}^*}|^2 = \frac{1}{9}|\lambda_1|^2 + \frac{1}{9}|\lambda_2|^2 + \frac{1}{9}\{5|\lambda_1|^2 + 4\mathrm{Re}\lambda_1\lambda_2^*\}(\vec{q}\cdot\vec{p})^2 \tag{4.27}$$

Equation 4.27 becomes

$$\frac{dN}{d\cos\theta'} = \text{constant} \times (1 + \alpha\cos^2\theta') \tag{4.28}$$

where

$$\alpha = \frac{5|\lambda_2|^2 + 4\mathrm{Re}\lambda_1\lambda_2^*}{|\lambda_1|^2 + |\lambda_2|^2} \tag{4.29}$$

Assuming that λ_1 and λ_2 are relatively real, equation 4.29 is:

$$\alpha = \frac{4R + 5R^2}{1 + R^2} \tag{4.30}$$

where $R = \lambda_1/\lambda_2$. In a similar fashion, the reaction

$$e^+e^- \rightarrow D\bar{D}^* \rightarrow D\bar{D}\gamma\gamma$$

can be treated. Using equations 4.22, 4.13, and 4.12, the amplitude for the above reaction becomes:

$$|M_{D^*\bar{D}^*}|^2 = \frac{1}{9}\{4|\lambda_1|^2 + |\lambda_2|^2[4 + 22[1 - (\vec{q}\cdot\vec{p})^2]]$$

$$+ 8\mathrm{Re}\lambda_1\lambda_2^*[1 - (\vec{q}\cdot\vec{p})^2]\} \tag{4.31}$$

Equation 4.31 can be used to derive the angular distribution of the D relative to the D* direction in the same form as before where α now has the value

$$\alpha = -\frac{11|\lambda_2|^2 + 4\mathrm{Re}\lambda_1\lambda_2^*}{2|\lambda_1|^2 + 13|\lambda_2|^2 + 4\mathrm{Re}\lambda_1\lambda_2^*} \tag{4.32}$$

Keeping the definition of R as before and making the same assumptions

about the phase equality of λ_1 and λ_2:

$$\alpha = -\frac{4R + 11R^2}{4 + 4R + 13R^2} \tag{4.33}$$

The remaining case occurs when

$$e^+e^- \rightarrow D^*\bar{D}^* \rightarrow D\bar{D}\pi\gamma$$

and the detected D arises from either pion or photon emission in the decay of a D*. First consider the D which arises in D* radiative decay. From equation 4.26

$$|M_{D^*\bar{D}^*}|^2 = \frac{1}{9}\{2|\lambda_1|^2 + |\lambda_2|^2\{2 + 5(1 - [\vec{q}\cdot\vec{p}]^2)\}$$

$$+ 2\mathrm{Re}\lambda_1\lambda_2^*[1 - (\vec{q}\cdot\vec{p})^2]\} \tag{4.34}$$

For this case

$$\alpha = -\frac{2R + 5R^2}{2 + 2R + 7R^2} \tag{4.35}$$

Last, detecting the D produced through D* pion emission is described by the expression

$$|M_{D^*\bar{D}^*}|^2 = \frac{2}{9}[|\lambda_1|^2 + |\lambda_2|^2(1 + 5(\vec{q}\cdot\vec{p})^2) + 2\mathrm{Re}\lambda_1\lambda_2^*(\vec{q}\cdot\vec{p})^2]$$

so that

$$\alpha = \frac{5R^2+2R}{1+R} \tag{4.36}$$

To summarize, an expression has been derived which describes the angular distribution of a D meson relative to the helicity axis of the D* from which it decayed. This angular distribution depends on whether the decay is through pion or photon emission, on the decay mode of the undetected $\overline{D}$* also produced in the event, and on the ratio of the squares of the spin 2 to spin 0, P wave amplitudes. These effects manifest themselves through the recoil effective mass distribution opposite a detected D according to equation 4.8.

4.3 Derivation of the Fitting Function

The preceding section showed how the angular distribution of a D relative to its parent D*'s helicity axis was always of the form

$$\frac{dN}{d\cos\theta'} \sim 1 + \alpha\cos^2\theta'$$

Since α can be determined by direct calculation from symmetry principles only for the reaction

$$e^+e^- \rightarrow D^*\overline{D} \rightarrow (D\pi)\overline{D} \quad \text{or} \quad (D\gamma)\overline{D}$$

α must be a free parameter of the fit to the recoil mass spectrum for

$$e^+e^- \rightarrow D^*\overline{D}, \quad D^* \rightarrow D + x$$

In the preceding section it was shown that the observed value of α is

not necessarily the same for charged and neutral D* decays since the observed α is dependent on the branching fractions to the various D* decay modes as well as on the production and decay dynamics.

The functional form chosen to parameterize the angular distribution is

$$\frac{dN}{d\cos\theta'} = \frac{3}{2(3+\alpha)}\,(1 + \alpha\cos^2\theta')$$

with restricted to the range: $-1 \leq \alpha \leq \infty$. The normalization was chosen so that

$$\int_{-1}^{1} \frac{dN}{d\cos\theta'}\, d\cos\theta' = 1$$

From equation 4.7

$$\frac{dN}{dM_R^2} = \frac{3}{\Delta(3+\alpha)}\,(1 + \alpha\cos^2\theta') \qquad (4.37)$$

where M_R is the effective recoil mass opposite a detected D. Since

$$\cos\theta' = \frac{1}{\Delta}(2M_R^2 - \Sigma)$$

it follows that

$$\frac{dN}{du} = \frac{3}{\Delta(3+\alpha)}\,\{1 + \frac{\alpha}{\Delta^2}(2u - \Sigma)^2\} \qquad (4.38)$$

where, for convenience the variable u has been defined as $u = M_R^2$. While equation 4.38 describes the produced spectrum in recoil effec-

tive mass squared, the observed spectrum is substantially different due to momentum resolution and due to momentum dependence in the D detection efficiency. (This is the same momentum dependent detection efficiency discussed in chapter 3).

To compensate for the effects of detection efficiency, the observed spectrum was corrected for efficiency using the parameterizations shown in figures 3.1a and 3.2a. This allows one to fit the produced spectrum. The uncertainties due to momentum resolution were accounted for by convoluting equation 4.38 with an appropriate resolution function. Non-relativistically:

$$u = E_{cm}^2 + m_D^2 - 2E_{cm}m_D - \frac{E_{cm}}{m_D}P_P^2 \qquad (4.39)$$

where P_P is the produced momentum of the detected D. Assuming that the detected D momentum $|P_d|$ is distributed normally around the produced momentum:

$$\sigma_u = \frac{2E_{cm}}{m_D} P_d \sigma_P$$

where σ_P is the resolution on the D momentum. This momentum resolution, determined from monte carlo methods, is shown for both neutral and charged D's in figures 4.3a and 4.3b.

Returning to equation 4.38, let u' be the square of the observed recoil mass, so that

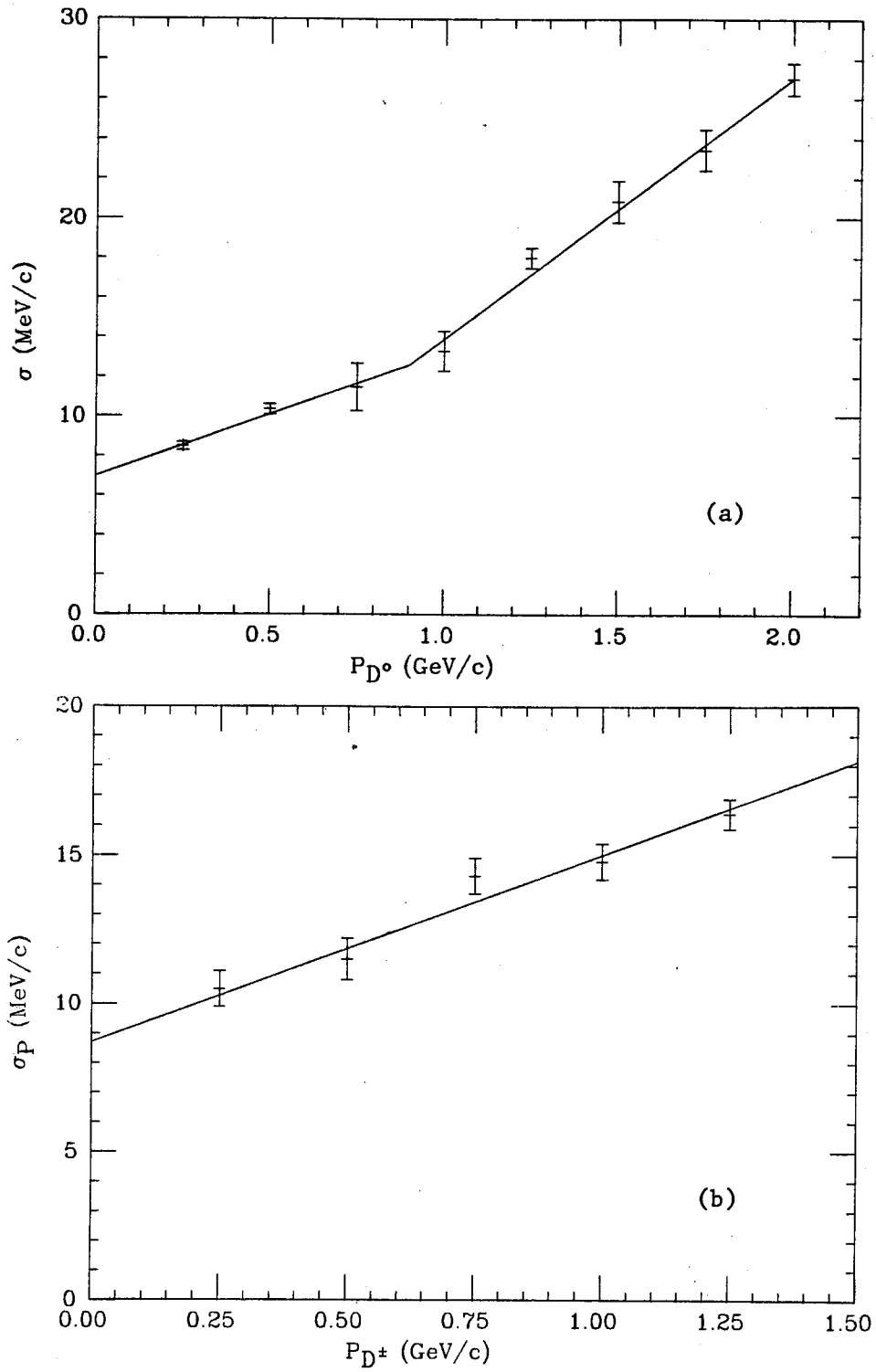

XBL 808-10909

figure 4.3
(a)- momentum resolution of neutral D meson.
(b)- momentum resolution of charged D meson.

$$\frac{dN}{du'} = \frac{1}{\sqrt{2\pi}\sigma_u} \int_{u_{min}}^{u_{max}} du \left[\exp - \frac{(u - u')^2}{2\sigma_u^2}\right]$$

$$\frac{3}{\Delta(3 + \alpha)} \left[1 + \frac{\alpha}{\Delta^2}(2u - \Sigma)^2\right] \tag{4.40}$$

After considerable algebra, and neglecting terms of order σ_u^2, the intrepid reader may derive the expression

$$\frac{dN}{du'} = [\mathrm{erf}(V_{max}) - \mathrm{erf}(V_{min})][1 + \frac{\alpha}{\Delta^2}(2u' - \Sigma)^2] \frac{3}{2\Delta(3 + \alpha)}$$

$$+ [\exp(-V_{min}^2) - \exp(-V_{max})^2] \frac{(2u - \Sigma)6\sqrt{2}\sigma_u \alpha}{(3 + \alpha)\Delta^3\sqrt{\pi}} \tag{4.41}$$

where

$$V_{min} = \frac{u_{min} - u'}{\sqrt{2}\sigma_u}$$

$$Vmax = \frac{u_{max} - u'}{\sqrt{2}\sigma_u}$$

$$\mathrm{erf}(x) = \frac{2}{\sqrt{\pi}} \int_0^x dy e^{-y^2}$$

To test the validity of the numerous approximations made in deriving this function, a monte carlo model was constructed which explicitly generated the amplitudes for D and D* production described by equations 4.8, 4.10, 4.12, and the decay amplitudes from equations 4.13 and 4.14. The effective recoil mass distribution, its fit using equation 4.41, and the distributions for the subreactions arising

from the various possible D* decay modes, are shown in figure 4.4.

The individual subreactions which are sources of D's are shown in figure 4.4 as the lines underneath the uppermost one. The uppermost line is the sum of these individual reactions. The form of the fitting function used to describe the D^0 recoil spectrum is

$$\frac{dN_0}{dM_R^2} = \frac{L\Delta M_R^2}{\varepsilon_{K\pi}(M_R^2)B_{D^0\to K\pi}} \{2\sigma_{D^0\bar{D}^0} C_0^0 + \sigma_{D^{*0}\bar{D}^0+\bar{D}^{*0}D^0} [C_2^0 + B_{D^{*0}\to D^0\pi^0} C_1^0$$

$$+ B_{D^{*0}\to D^0\gamma} C_4^0 + B_{D^{*+}\to D^0\pi^+} C_3^0] + 2\sigma_{D^{*0}\bar{D}^0} [B_{D^{*0}\to D^0\pi^0} C_5^0 + B_{D^{*0}\to D^0} C_7^0$$

$$+ B_{D^{*+}\to D^0\pi^+} C_6^0] \} + A_0^0 + A_1^0(M_{R,0}^2 - M_R^2) + A_2^0(M_{R,0}^2 - M_R^2) \qquad (4.42)$$

For charged D production, the form of the fitting function is

$$\frac{dN^+}{dM_R^2} = \frac{L\Delta M_R^2}{\varepsilon_{K\pi\pi}(M_R^2)B_{D^+\to K\pi\pi}} \{2\sigma_{D^+D^-} C_0^+ + \sigma_{D^{*+}D^-+D^{*-}D^+} [B_{D^{*+}\to D^+\gamma} C_4^+$$

$$+ B_{D^{*+}\to D^+\pi^0} C_1^+ + C_2^+] + 2\sigma_{D^{*+}D^{*-}} [B_{D^{*+}\to D^+\gamma} C_7^+ + B_{D^{*+}\to D^+\pi^0} C_5^+]\}$$

$$+ A_0^+ + A_1^+(M_{R,0}^2 - M_R^{2)} + A_2^+(M_{R,0}^2 - M_R^2) \qquad (4.43)$$

where the A_i^j coefficients describe a quadratic background expanded about $M_{R,0}^2$ which is the lowest data bin on each histogram. The C_i^j are the theoretical distributions given by equation 4.41 for the "reflected" spectra (that is, detected D's which are the result of a D* decay), and also for the direct spectra (which are the trivial cases of delta functions convoluted with the detector resolution).

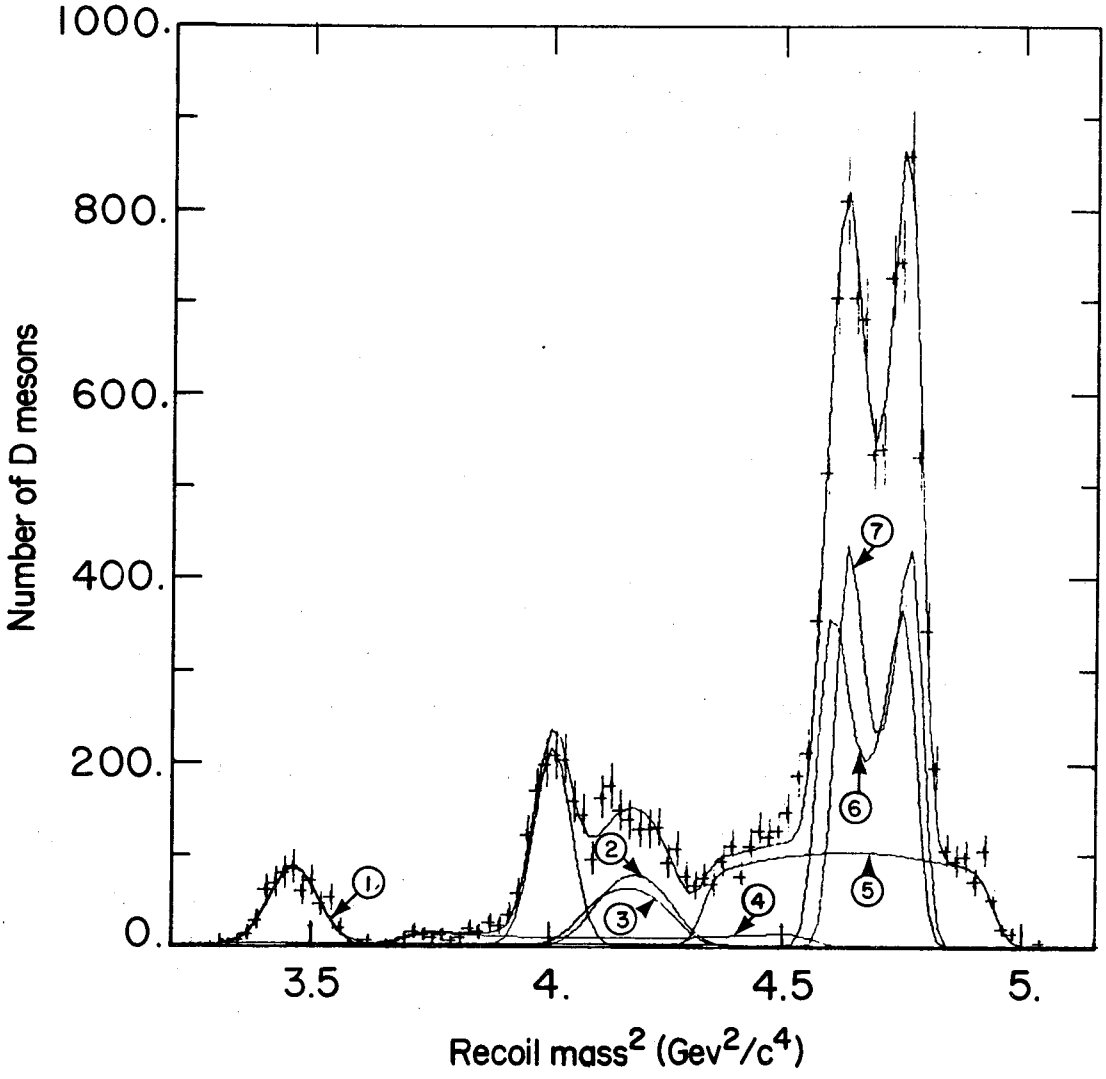

XBL 808-10935

figure 4.4

(1)- $e^+e^- \to D\bar{D}$
(2)- $e^+e^- \to D^{*+}D^-$, $D^{*+} \to D^0\pi^+$
(3)- $e^+e^- \to D^{*0}\bar{D}^0$, $D^{*0} \to D^0\pi^+$
(4)- e^+e^- $D^{*0}\bar{D}^0$, $D^{*0} \to D^0\gamma$
(5)- $e^+e^- \to D^{*0}\bar{D}^{*0}$, $D^{*0} \to D^0\gamma$
(6)- $e^+e^- \to D^{*0}\bar{D}^{*0}$, $D^{*0} \to D^0\pi^0$
(7)- $e^+e^- \to D^{*+}D^{*-}$, $D^{*+} \to D^0\pi^+$

These variables are summarized in table 4.2.

4.4 Results of the Fit

The theoretical distributions given by equations 4.42 and 4.43 have several parameters in common under the assumption of isospin symmetry:

$$\sigma_{D^0\bar{D}^0} = \sigma_{D^+D^-}(P_{D^0}/P_{D^+})^3$$

$$\sigma_{D^{*0}\bar{D}^0} = \sigma_{D^{*+}D^-}(P_{\bar{D}^0}/P_{D^-})^3$$

$$\sigma_{D^{*0}\bar{D}^{*0}} = \sigma_{D^{*+}D^{*-}}(P_{\bar{D}^{*0}}/P_{D^{*-}})^3$$

The p^3 factor corrects for the angular momentum and phase space effects in the production of charged and neutral D's and D*'s. This is necessary because the charged D's and D*'s are slightly more massive than the neutral ones. Also, the branching fraction for a D^{*+} to decay to a D^0 is related to the other D^{*+} branching fractions through

$$B_{D^{*+}\to D^0\pi^+} + B_{D^{*+}\to D^+\pi^0} + B_{D^{*+}\to D^+\gamma} = 1$$

There is therefore some commonality between the charged and neutral D recoil mass spectra with regard to D* branching fractions.

To increase the statistical power of the fitting, a simultaneous chi-square minimization was done to eight different data sets

Definitions of Variables Appearing in Equations 4.42 and 4.43

Variable	Meaning
L	Integrated luminosity of data sample
$\varepsilon_{K\pi}(M_R^2)$	Detection efficiency for $D^0 \to K\pi$, which is momentum dependent and therefore depends on the effective recoil mass^2 M_R^2.
ΔM_R^2	Bin width of histogram in dN/dM_R^2
C_0^0	Distribution in dN/dM_R^2 for $D^0\bar{D}^0$ production
C_1^0	Distribution in dN/dM_R^2 for $e^+e^- \to D^{*0}\bar{D}^0$, $D^{*0} \to D^0\pi^0$ and the D^0 is detected
C_2^0	Distribution in dN/dM_R^2 for $e^+e^- \to D^{*0}\bar{D}^0$ and the $\bar{D}^0$ is detected
C_3^0	Distribution in dN/dM_R^2 for $e^+e^- \to D^{*+}\bar{D}$, $D^{*+} \to D^0\pi^+$ and the $\bar{D}^0$ is detected
C_4^0	Distribution in dN/dM_R^2 for $e^+e^- \to D^{*0}\bar{D}^0$, $D^{*0} \to D^0\gamma$ and the D^0 is detected
C_5^0	Distribution in dN/dM_R^2 for $e^+e^- \to D^{*0}\bar{D}^{*0}$, $D^{*0} \to D^0\pi^0$
C_6^0	Distribution in dN/dM_R^2 for $e^+e^- \to D^{*+}D^{*-}$, $D^{*+} \to D^0\pi^+$
C_7^0	Distribution in dN/dM_R^2 for $e^+e^- \to D^{*0}\bar{D}^{*0}$, $D^{*0} \to D^0\gamma$
C_0^+	Distribution in dN/dM_R^2 for $e^+e^- \to D^+D^-$
C_1^+	Distribution in dN/dM_R^2 for $e^+e^- \to D^{*+}D^-$, $D^{*+} \to D^+\pi^0$ with the D^+ detected
C_2^+	Distribution in dN/dM_R^2 for $e^+e^- \to D^{*+}D^-$, D^- detected
C_4^+	Distribution in dN/dM_R^2 for $e^+e^- \to D^{*+}D^-$, $D^{*+} \to D^+\gamma$ with the D^+ detected
C_5^+	Distribution in dN/dM_R^2 for $e^+e^- \to D^{*+}D^{*-}$, $D^{*+} \to D^+\pi^0$, D^+ detected
C_7^+	Distribution in dN/dM_R^2 for $e^+e^- \to D^{*+}D^{*-}$, $D^{*+} \to D^+\gamma$, D^+ detected
$\varepsilon_{K\pi\pi}(M_R^2)$	Detection efficiency for $D^\pm \to K^\mp\pi^\pm\pi^\pm$
$B_{D^0\to\pi}$	Branching fraction for $D^0 \to K^-\pi^+$ as determined by Mark II, $0.028 \pm .006$
$B_{D^+\to K\pi\pi}$	Branching fraction for $D^+ \to K^-\pi^+\pi^+$ as determined by Mark II, $0.051 \pm .011$
$B_{D^*\to x}$	Branching fraction for D^* decay to state x

Table 4.2

consisting of the charged and neutral recoil mass spectra in the energy regions of 3.88 to 4.02 GeV, 4.02 to 4.15 GeV, 4.16 GeV, and 4.16 to 4.3 GeV using the CERN minimization routine MINUIT.[36]

One problem with the strategy of using all eight data sets was that only the 4.16 GeV data were taken at a fixed center of mass energy. The other data were all taken in a mode where the center of mass energy was evenly distributed over a range of roughly 140 MeV. Since the effective recoil mass distribution for "reflected" D's (D's not produced directly) depends on the center of mass energy, the reflected distribution moves as the center of mass energy changes. The fitting function given in equation 4.41 holds true only for fixed center of mass energy data, thus the uncertainty introduced in neglecting energy spread must be taken into account. To estimate this error, a monte carlo which simulated reactions (1), (2), and (3) was used to produce a distribution in dN/dM^2_{recoil}. The monte carlo generated distribution was then fit to a theoretical distribution using a center of mass energy 43 MeV too high (the root mean square error on the center of mass energy for data coming from the variable center of mass energy region). The additional uncertainty is included in the results.

The fitting was done in two ways. The first method assumed that the angular distribution of a decay produced D relative to its parent D*'s helicity axis was isotropic. The second method allowed for an angular dependence in $\cos^2\theta$ as discussed earlier. The assumption was made that this angular distribution (which was shown to depend on the undetermined ratio of the spin 2 to spin 0,P wave amplitudes) was

slowly varying. Thus the same angular dependencies were assumed for all four energy regions. The results of the fitting are shown in figures 4.5 and 4.6 and summarized in table 4.3.

As a check of the fitting results, the pair production cross sections for D production derived using the inclusive approach of chapter 3 were compared with the analysis done in this chapter. The comparison is shown in table 4.4. While the method of chapter 3 and that used in this chapter are not completely independent, the fact that the agreement between the two methods is rather good gives one some confidence in the signal and background parameterizations used in the theoretical expression for dN/dM_R^2. The fact that the results of fitting to a non-isotropic angular distribution are almost identical to the results of the isotropic fit indicates that results obtained are relatively insensitive to α.

4.5 Interpretation of the Results

It was suggested soon after the discovery of the D that the relative ratios of reactions (1), (2), and (3) could be described by simply counting the number of spin states available to each mode.[37] This argument predicts the relative ratios for production of reactions (1), (2), and (3) as

$$\sigma_{D\bar{D}} : \sigma_{D^*\bar{D}} : \sigma_{D^*\bar{D}^*} = P^3_{D\bar{D}} : 4P^3_{D^*\bar{D}} : 7P^3_{D^*\bar{D}^*}$$

At a center of mass energy of 4.16 GeV, this argument predicts the ratio

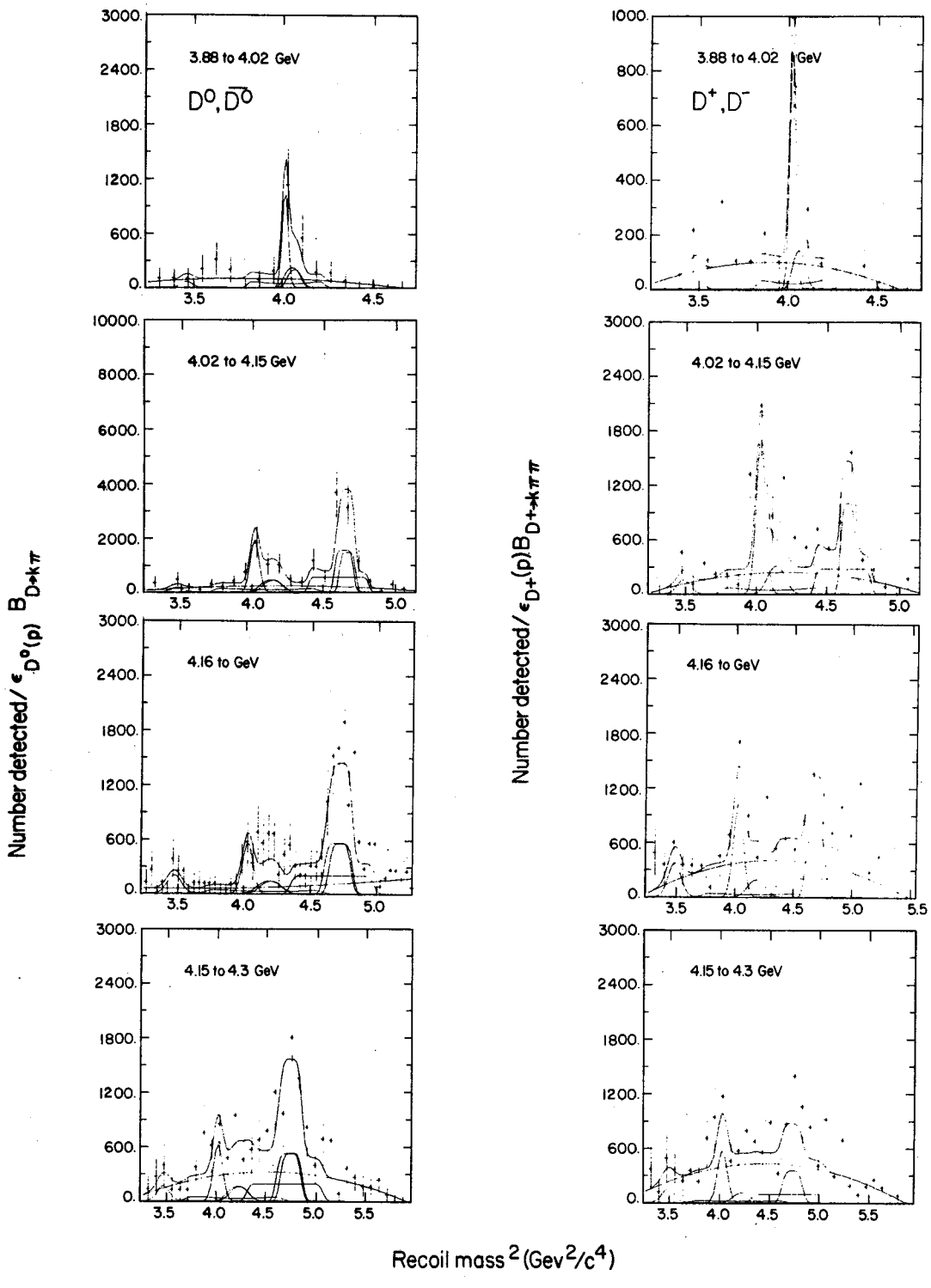

XBL 808-11112

figure 4.5

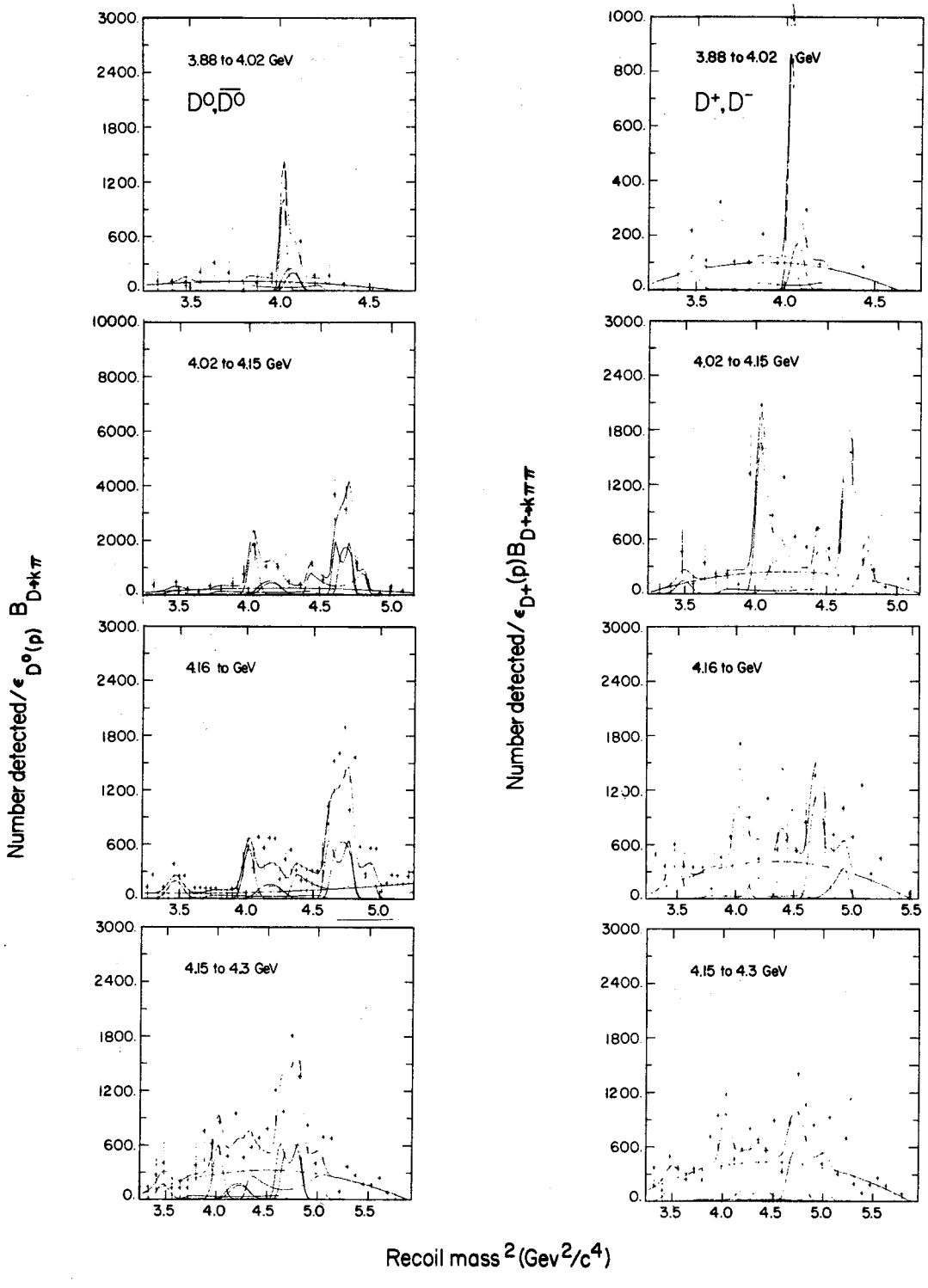

XBL 808-11113

figure 4.6

Table 4.3 Fit Results

Cross Section (nb)	Energy Region 3.88 - 4.02 GeV	4.02 - 4.15 GeV	4.16 GeV	4.15 - 4.3 GeV	
$\sigma_{D\bar{D}}$	$0.2 \pm {}^{0.3}_{0.2}$	0.3 ± 0.3	0.5 ± 0.2	0.3 ± 0.3	Isotropic Fit
$\sigma_{D^*\bar{D}}$	3.0 ± 0.8	4.3 ± 0.7	2.3 ± 0.5	1.8 ± 0.6	
$\sigma_{D^*\bar{D}^*}$	--	6.3 ± 0.9	4.9 ± 0.7	3.4 ± 0.7	
$\sigma_{D\bar{D}}$	$0.2 \pm {}^{0.3}_{0.2}$	$0.2 \pm {}^{0.3}_{0.2}$	0.5 ± 0.3	0.3 ± 0.3	Anisotropic Fit
$\sigma_{D^*\bar{D}}$	2.9 ± 0.8	4.2 ± 0.8	2.3 ± 0.6	1.8 ± 0.6	
$\sigma_{D^*\bar{D}^*}$	--	6.6 ± 1.3	4.9 ± 0.8	3.6 ± 0.9	

Branching Ratios

Mode	Isotropic Fit	Anisotropic Fit	Mark I Result
$D^{*0} \to D^0\pi^0$	$.47 \pm .09$	$.53 \pm .12$	$.55 \pm .15$
$D^{*0} \to D^0\gamma$	$.53 \pm .09$	$.47 \pm .12$	$.45 \pm .15$
$D^{*+} \to D^0\pi^+$	$.44 \pm .07$	$.44 \pm .10$	$.60 \pm .15$
$D^{*+} \to D^+\pi^0$	$.28 \pm .07$	$.34 \pm .07$	--
$D^{*+} \to D^+\gamma$	$.28 \pm .10$	$.22 \pm .12$	--

D Production Cross Section

Energy Region (GeV)	Recoil Method (nb)	Inclusive Method (nb)
3.88 - 4.02	3.2 ± 0.8	5.4 ± 1.5
4.02 - 4.15	10.9 ± 1.2	10.5 ± 1.1
4.16	7.7 ± 0.9	7.1 ± 1.6
4.15 - 4.30	5.5 ± 1.0	5.6 ± 1.0

Table 4.4

$$1.0 : 2.2 : 1.4$$

The experimentally observed ratio[19]

$$1\pm.6 : 4.6\pm1.2 : 9.8\pm1.6$$

is in gross disagreement with this prediction. This indicates the presence of dynamical effects in the D production mechanism.

One way to introduce dynamical considerations is through the potential model formalism of Eichten et al.[29] A spin and flavor independent potential is postulated as

$$V(r)=-k/r+r/a^2$$

This potential has a coulomb term, in analogy with positronium, and a confining term which accounts for the absence of free quarks. Wave functions and energy levels may be determined by solving the Schroedinger equation using the above potential to describe the binding of a c and a $\bar{c}$ quark. Identifying the states (in the notation $n^{2s+1}L_J$) 1^3S_1, 2^3S_1, 2^3P as the psi, psi′, and center of gravity of the χ states allows one to calculate the parameters k, a, and m_c (the mass of the charmed quark) and thus completely determine the wave functions of the quarks in the $c\bar{c}$ state.

These wave functions can be used to calculate R_D under the assumptions:

(1) Production of charm is mediated by those charmonium states which couple to the photon

(2) the basic production process is quasi-two-body, one of reactions (1), (2), and (3) occurs, and

(3) the decay product state vectors, for the sake of simplicity, can be completely described non-relativistically (including the light u or d quarks as well as the c quark).

The amplitude

$$< D_1(p_1), D_2(p_2) \mid H_{interaction} \mid \psi(n) >$$

with D_i as a D or D*, is an oscillating but decreasing function of momentum and is shown in figure 4.7 for the decay amplitude

$$< D_1(p_1), D_2(p_2) \mid H_{interaction} \mid 3^3S_1 >$$

Thus, the momentum of the decay products affects their relative abundances. The arrows shown indicate that at 4.16 GeV center of mass, the amplitude for $D^*\bar{D}^*$ production is considerably larger than that for D*D or $D\bar{D}$ production. The relative ratios of reactions (1), (2), and (3) should change as a function of energy, and $D\ \bar{D}$ production should vanish at 4.03 GeV due to the zero at 0.9 GeV/c in the decay amplitude.

Figure 4.8 compares the ratios of reactions (1), (2), and (3) predicted by the model with the results given in table 4.3 for the isotropic fit. The relative abundances are in qualitative agreement with this model. $D\bar{D}$ production is suppressed at all energies and $D^*\bar{D}^*$ production appears to be the source of the majority of detected D's over the entire center of mass energy range examined. While the model predicts more $D^*\bar{D}^*$ production just above 4 GeV than is observed, there is agreement between the model and the $D^*\bar{D}^*$ results between 4.15 GeV and 4.3 GeV. Agreement between the model and the observed ratios of $D\bar{D}$ and $D^*\bar{D}$ production is excellent in all four

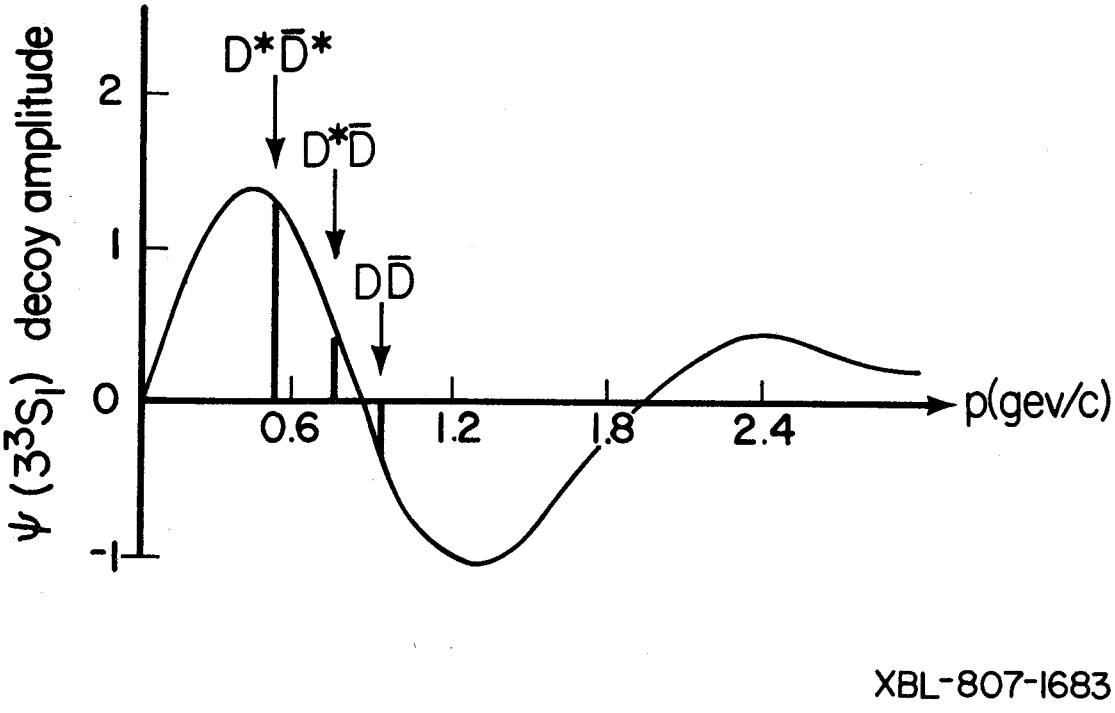

figure 4.7

(adapted from ref. 29. Used with the author's permission)

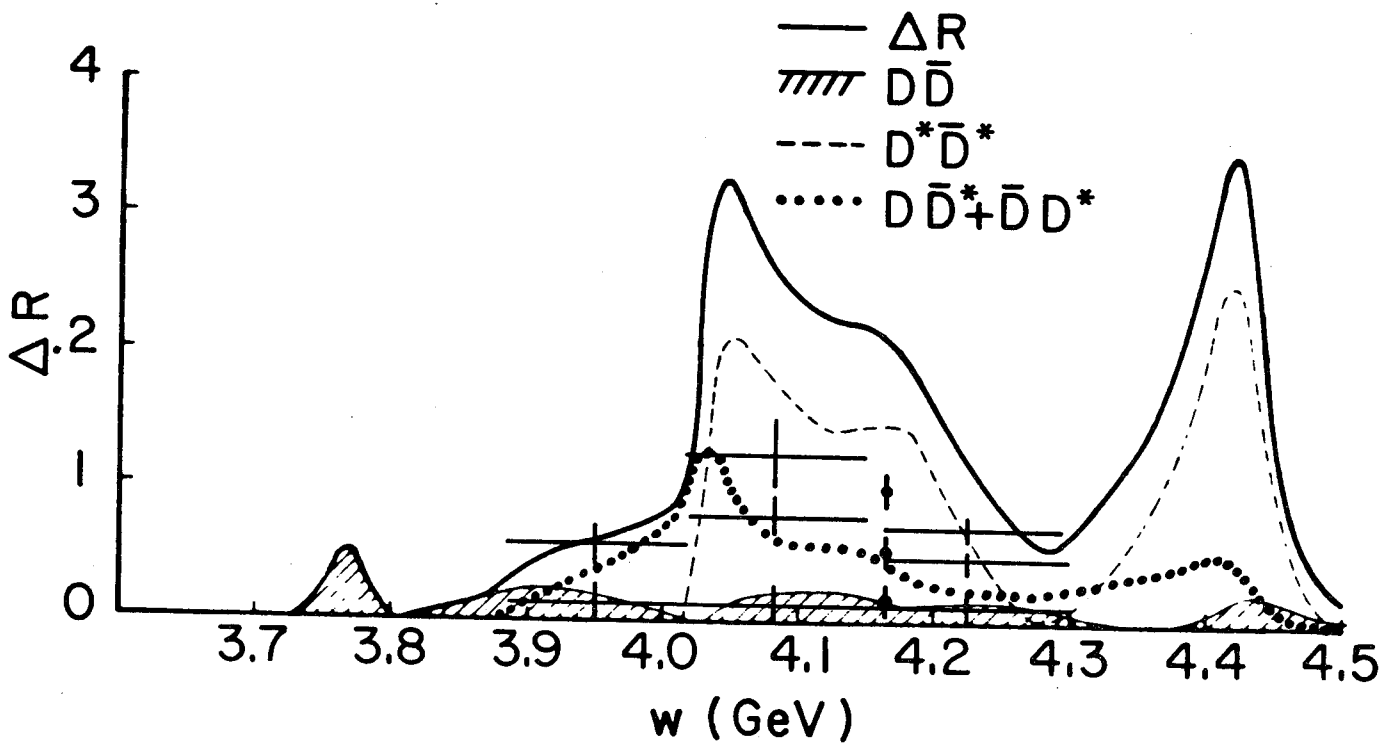

XBL808- 1760

figure 4.8

energy regions.

The branching ratios for D* decays which have been determined are in good agreement with the previously reported Mark I results.[19] It is interesting to compare some of the measured branching ratios with what one might expect to find theoretically. The ratio of the widths

$$\frac{\Gamma(D^{*+} \rightarrow \pi^0 D^+}{\Gamma(D^{*+} \rightarrow \pi^+ D^0}$$

is easily calculable if the decay proceeds through a strong interaction and therefore conserves isospin. Using Clebsch-Gordan coefficients along with P wave angular momentum and phase space corrections

$$\frac{\Gamma(D^{*+} \rightarrow \pi^0 D^+)}{\Gamma(D^{*+} \rightarrow \pi^+ D^0)} = \frac{1}{2}\left(\frac{P_{\pi^0}}{P_{\pi^+}}\right)^3 = 0.46$$

Experimentally, the isotropic fit gives a value for the ratio of 0.64 ± .18, while the anisotropic fit gives 0.77 + .24. Both of these results, although high, agree with the theoretical prediction within the quoted errors.

The radiative decays of the charged and neutral D* have been predicted theoretically. If the radiative decay of the D* is a hyperfine transition involving the spin-flip of the light quark, one might expect the radiative width to depend on the magnetic moment of the u and d quarks. (The c quark is neglected because of its much larger mass). Thus a simple estimate of the ratio of the charged to

neutral D* radiative branching fractions is

$$\frac{\Gamma(D^{*+} \rightarrow D^{+}\gamma)}{\Gamma(D^{*0} \rightarrow D^{0}\gamma)} = \left(\frac{e_d}{e_u}\right)^2 = \frac{1}{4}$$

Experimentally, the isotropic fit gives a result of $0.53 \pm .25$. The result for the anisotropic is $0.47 \pm .28$. Both results are about one standard deviation higher than the simple estimate made above, yet they are approximately consistent with this prediction within experimental uncertainty. More sophisticated theoretical estimates, which take into account the quark wave function inside the D*.[38] or make use of SU(4) symmetry,[39] predict a ratio of only about 0.05. The Mark II results are in disagreement with these predictions by roughly two standard deviations.

Chapter 5 D Production at a Center of Mass Energy of 5.2 GeV

Substantial D production persists at center of mass energies above the (roughly 4.0 GeV to 4.4 GeV) resonance region. Figures 5.1a and 5.1b show the charged $K\pi$ invariant mass and $K\pi\pi$ invariant mass combinations observed at a center of mass energy of 5.2 GeV. Note the large combinatoric background underneath the signal, particularly in the case of the charged D meson. Figures 5.2a and 5.2b show the effective recoil masses formed by taking all events with $K\pi$ or $K\pi\pi$ masses between 1.82 GeV/c^2 and 1.90 GeV/c^2 and fixing the mass of the combination equal to the D mass (using 1.863 GeV/c^2 as the neutral D mass and 1.868 GeV/c^2 as the charged D mass). It is apparent that the production mode at this higher energy is very different from that observed in the resonance region. The structure observed in the recoil spectrum at 4.16 GeV, a result of the quasi-two-body production of D's at that energy, is not clearly evident at 5.2 GeV. (While it is difficult to tell, from figures 5.2a and 5.2b, that there are no $D^*\bar{D}^*$ events, it is obvious that there is little or no $D\bar{D}$ or $D^*\bar{D}$ production). Evidently the production mechanism involves more than two initially produced particles. In this chapter, the production mechanism for D's at this higher energy is examined in detail.

5.1 The Multiplicity Observed Opposite a Detected D

If the production mechanism for D mesons at 5.2 GeV is of the form

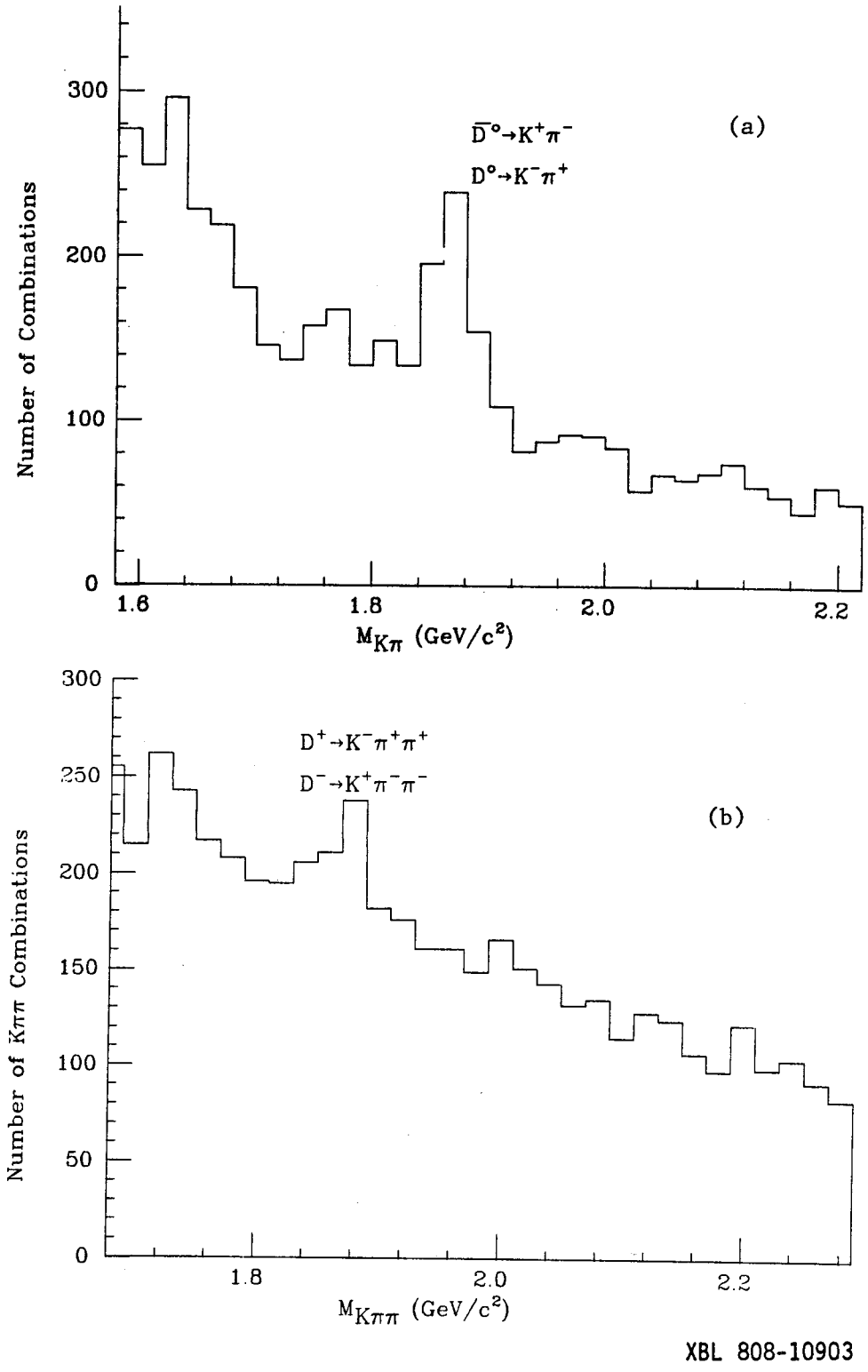
300
200
100
0
Number of Combinations
$\bar{D}^{o} \to K^{+}\pi^{-}$
$D^{o} \to K^{-}\pi^{+}$
(a)
1.6
1.8
2.0
2.2
$M_{K\pi}$ (GeV/c^2)
300
250
200
150
100
50
0
Number of $K\pi\pi$ Combinations
$D^{+} \to K^{-}\pi^{+}\pi^{+}$
$D^{-} \to K^{+}\pi^{-}\pi^{-}$
(b)
1.8
2.0
2.2
$M_{K\pi\pi}$ (GeV/c^2)
XBL 808-10903

figure 5.1

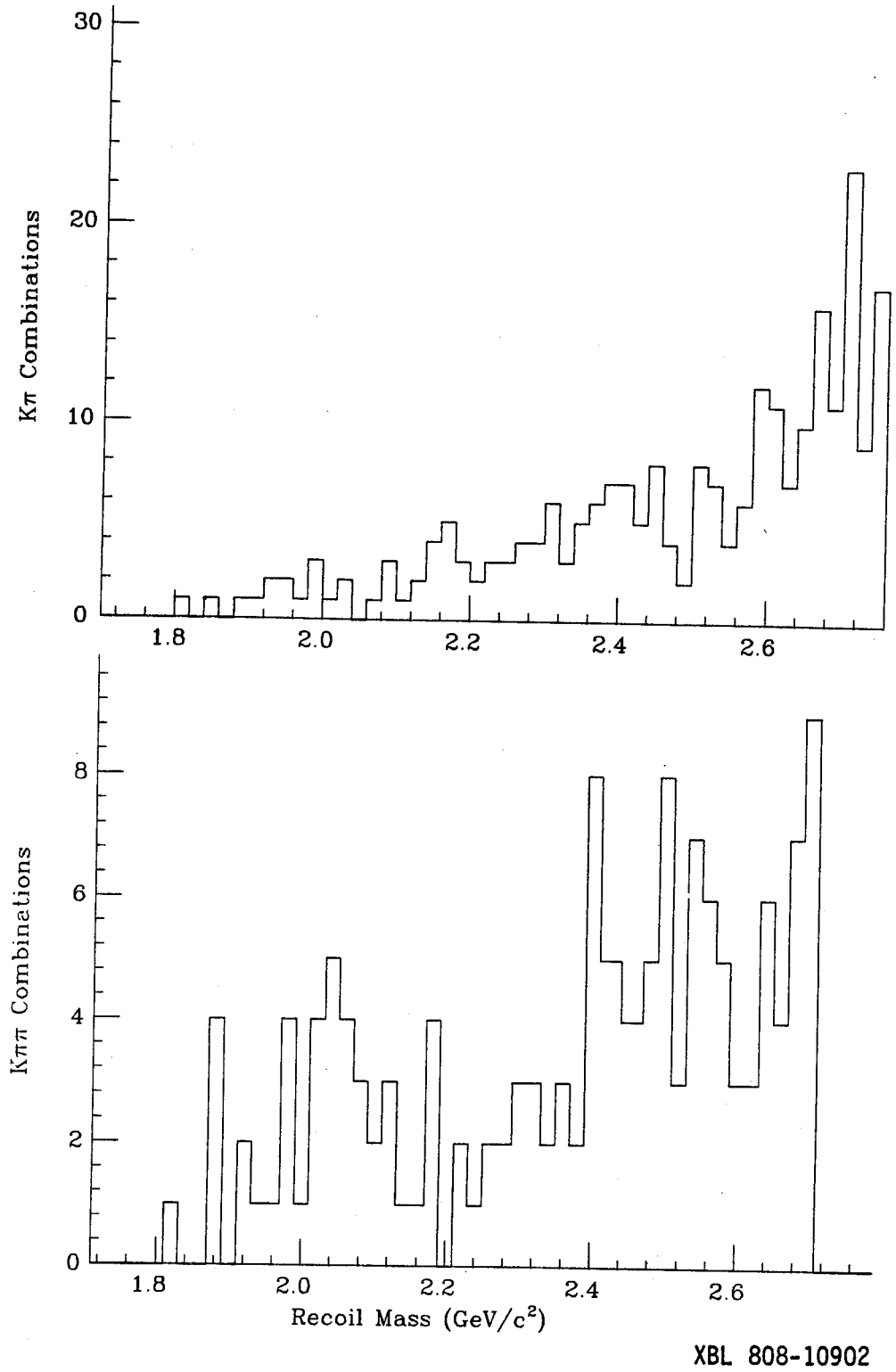

figure 5.2
(a)- recoil opposite $K^{\pm}\pi^{\mp}$
(b)- recoil opposite $K^{\mp}\pi^{\pm}\pi^{\pm}$

$$e^+e^- \rightarrow D\bar{D} + n\pi$$

where the D indicates either a D or a D*, and n is some small positive integer, then the additional pions produced contribute to the total charged multiplicity of the event. The charged particle multiplicity has already been determined[17] at a center of mass energy of 3.772 GeV for events that are purely

$$e^+e^- \rightarrow D\,\bar{D}$$

If an increase is observed in the mean charged particle multiplicity, that is evidence that additional pions are produced in association with the D's. The poor signal to noise ratio observed in figures 5.1a and 5.1b mandates a background subtraction to determine the multiplicity.

The method used was to select events with $K\pi$ invariant masses in the region $1.82\ \mathrm{GeV/c^2} < M_{K^\pm\pi^\pm} < 1.90\ \mathrm{GeV/c^2}$, and count the number of additional charged particle tracks in the event falling within the cuts described in chapter 2. Also, an equal number of events were selected where $1.65\ \mathrm{GeV/c^2} < M_{K^\pm\pi^\mp} < 1.69\ \mathrm{GeV/c^2}$ or $2.03\ \mathrm{GeV/c^2} < M_{K^\pm\pi^\mp} < 2.07\ \mathrm{GeV/c^2}$, and the number of additional charged tracks in these events were also counted. The same procedure was used for charged D's where the selection was made on $M_{K^\mp\pi^\pm\pi^\pm}$. The multiplicity distribution of the events in the sidebands in invariant mass was then subtracted from the distribution due to the events in the signal region.

The background subtracted observed multiplicities for the charged and neutral D's are shown in figure 5.3a. The observed multiplicity must now be transformed into the produced multiplicity using the following method.

5.2 The Unfold Method

To determine the charged particle multiplicity produced opposite a detected D meson it is necessary to manipulate the observed multiplicity in a manner referred to as "unfolding." This technique will yield the true number of charged prongs produced opposite the detected D meson given the detected number of charged prongs. The following variables are needed to do the calculation:

D_i = the number of charged particles detected opposite a detected D.

P_i = the number of events with i charged particles produced opposite the detected D.

Q_{ij} = the probability of observing i charged tracks opposite a D when j tracks are actually produced.

These three variables are related by the expression:

$$D_i = \sum_{j=j_{min}} Q_{ij} P_j .$$

The lower limit of the summation is chosen so that charge is conserved. For instance, if a D^+ is detected, the produced multiplicity opposite it must be odd. Therefore j_{min} is chosen to be the least odd number greater than or equal to 1. (Since the number of D's

distribution of charged tracks
opposite a D

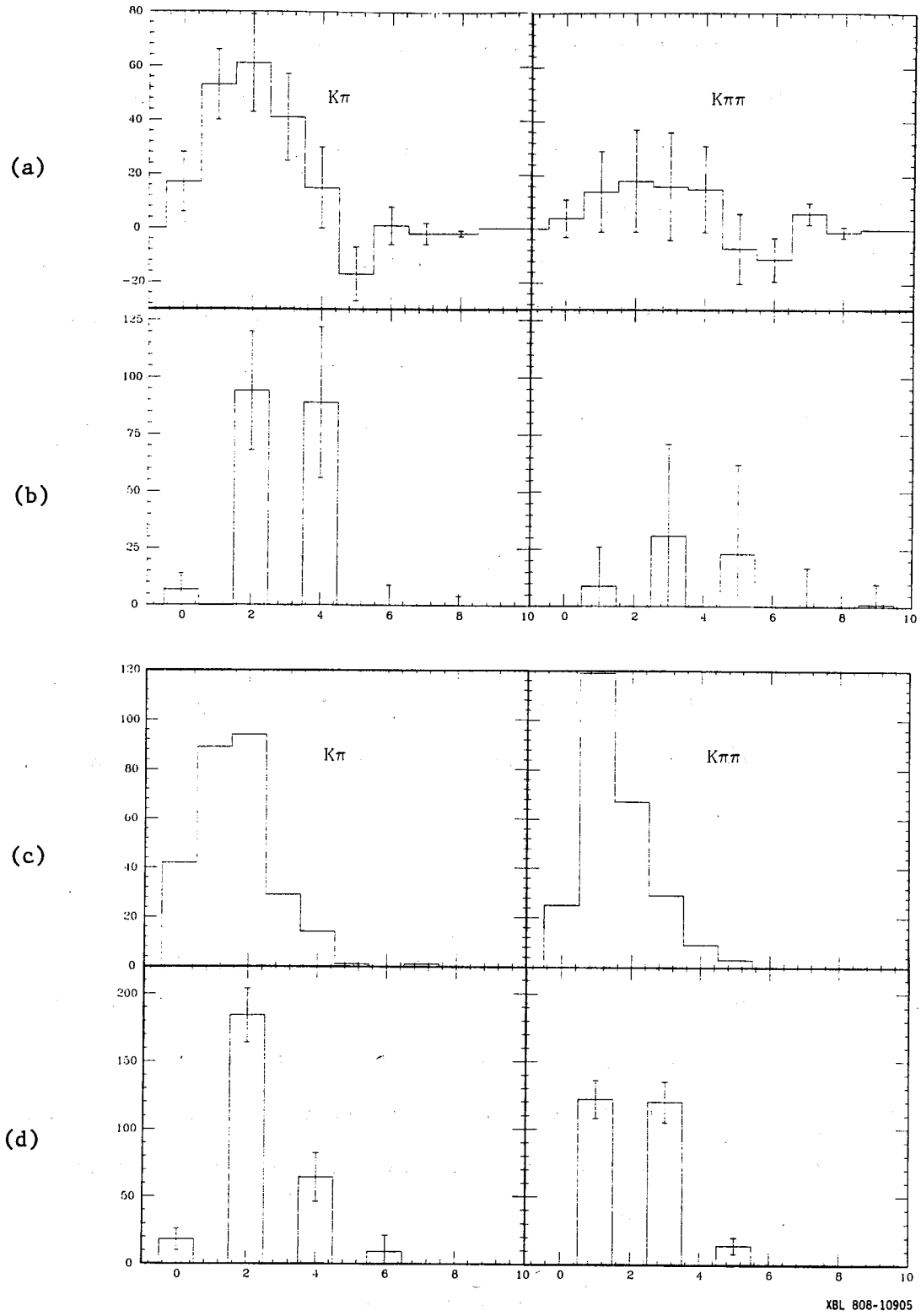

figure 5.3
(a)- observed mult. at 5.2 GeV
(b)- produced mult. at 5.2 GeV

(c)- observed mult. at 3.77 GeV
(d)- produced mult. at 3.77 GeV

detected has a substantial statistical error due to the large background subtraction, small effects such as photon conversions, which cause the detection of more charged tracks than were produced in the D decay, may be safely neglected).

The system of equations is overconstrained due to the requirement of charge conservation since D_i can be non-zero for any value of i while P_i must be zero for either even or odd i, depending on the charge of the detected D meson. P_j is obtained by χ^2 minimization

$$P_j = \sum_{k=1} \left(\sum_{i=1} \frac{Q_{ij} Q_{ik}}{\sigma_i^2} \right)^{-1} \sum_{m=1} \frac{D_m Q_{mk}}{\sigma_m^2} \tag{5.1}$$

where $\sigma_i^2 = D_i$.

Since the tracks are produced isotropically in $\cos\theta$ at a center of mass energy of 5.2 GeV, a reasonable simplification is to choose a binomial expression for Q_{ij}:

$$Q_{ij} = \frac{j!}{(j-i)!/i!} e^i (1-e)^j$$

Here e is the detection probability per charged track. This form for Q_{ij} assumes that solid angle coverage is the primary factor in determining Q_{ij}. No subtraction for the trigger efficiency was necessary since the detected D meson had already triggered the detector. A monte carlo simulation of

$$e^+e^- \rightarrow D\bar{D} + n\ \pi\text{'s}$$

was then done using charged and neutral D's and setting n equal to

two and three. The D's were allowed to decay using a statistical isospin model[40] In addition, photons were allowed to convert. The distribution of detected prongs for a given produced multiplicity was fit to the binomial expression for Q_{ij} with the constraint that P_i be greater than or equal to 0 for all i. The binomial approximation was found to give a good description of the monte carlo produced charged particle multiplicities. The result of the fit was that $e = 0.68 \pm 0.06$, where only those tracks having an absolute value of $\cos\theta$ less than 0.75 were counted as being detected.

The data used to determine Q_{ij} and the results of fitting Q_{ij} to a binomial distribution are listed in tables 5.1 and 5.2. Once Q_{ij} was determined, the observed multiplicities were transformed into the produced multiplicities using equation 5.1. The produced charged multiplicity distribution opposite a D meson is shown in figure 5.3b.

For comparison, the bottom portion (figures 5.3c and 5.3d) of the figure shows similar data taken at 3.772 GeV.[17] The comparison suggests that at 5.2 GeV additional pions are produced in association with D's. However, comparison of the unfolded multiplicity at 5.2 GeV with that observed at 3.77 GeV gives a χ^2 which indicates that this is not a statistically definitive test of whether or not D production is quasi-two-body at the higher center of mass energy. A more sensitive determination of the particle multiplicity is discussed in the next section.

5.3 The z Distribution of D's at 5.2 GeV

In this section, the energy distribution of D's produced at 5.2

Produced Number of Tracks

Detected Number of Tracks	4	6	8	10
0	.01	0	0	0
1	.06	.01	0	0
2	.31	.06	.02	.01
3	.38	.19	.07	.04
4	.24	.32	.16	.08
5		.28	.25	.14
6		.13	.27	.21
7			.18	.25
8			.05	.18
9				.08
10				.02

Monte Carlo $e^+e^- \to D^0\bar{D}^0\pi^+\pi^-\pi^0$

Produced Number of Tracks

Detected Number of Tracks	4	6	8	10
0	.01	0	0	0
1	.08	.01	0	0
2	.23	.06	.01	0
3	.44	.19	.05	.01
4	.25	.30	.15	.05
5		.30	.25	.16
6		.14	.28	.19
7			.20	.23
8			.05	.24
9				.09
10				.02

Monte Carlo $e^+e^- \to D^+D^-\pi^+\pi^-$

Table 5.1

Fit of Produced-Detected Matrix

to a Binomial Distribution in ε

Number of Generated Tracks	Monte Carlo Model	
	$D^+D^-\pi^+\pi^-$	$D^0\bar{D}^0\pi^+\pi^-\pi^0$
4	.71 ± .07	.69 ± .09
6	.71 ± .05	.70 ± .05
8	.69 ± .05	.68 ± .05
10	.68 ± .05	.66 ± .06
12	.68 ± .10	.63 ± .10

Average $\varepsilon = \bar{\varepsilon} = 0.68 \pm .06$

Table 5.2

GeV is described. Recall that in the resonance region data (see chapter 4), D production was entirely quasi-two-body. Thus the energy spectrum of the D's observed at those center of mass energies was populated only at those energies allowed by $D\bar{D}$, $D^*\bar{D}$, and $D^*\bar{D}^*$ production. At 5.2 GeV, the energy distribution was measured to see what could be learned about the production mechanism.

The energy distribution was investigated in the variable z, the ratio of the D meson's energy to D_{max} (the maximum possible energy the D can have. Thus, D's range in z from $2M_D/E_{cm}$ to 1 (where M_D is the D mass and E_{cm} is the center of mass energy). Rather than investigating dN/dz, the number of D's produced in a particular region of z, the data were used to determine the quantity $Sd\sigma/dz$, the fraction of the inclusive D cross section produced in a particular range of z multiplied by the square of the center of mass energy. The usefulness of this quantity with regard to scaling will be discussed in section 5.4.

The technique used to determine $Sd\sigma/dz$ was exactly that described in chapter 3 to measure R. Briefly, for neutral D's, the invariant mass of all oppositely charged $K\pi$ combinations was plotted versus the z of the $K\pi$ system. The data within the same z bin (of 0.05 width) were then fit by ^{2} minimization to the sum of a Gaussian of fixed width and center plus a quadratic background term. Since these data were obtained at 5.2 GeV, the kinematic limits imposed by the D mass are that $0.72 < z < 1.0$. The same technique was used for charged D's where the $k^{\mp}\pi^{+}\pi^{\pm}$ system was used. The individual fits are shown in figures 5.4 and 5.5 for neutral and charged D's

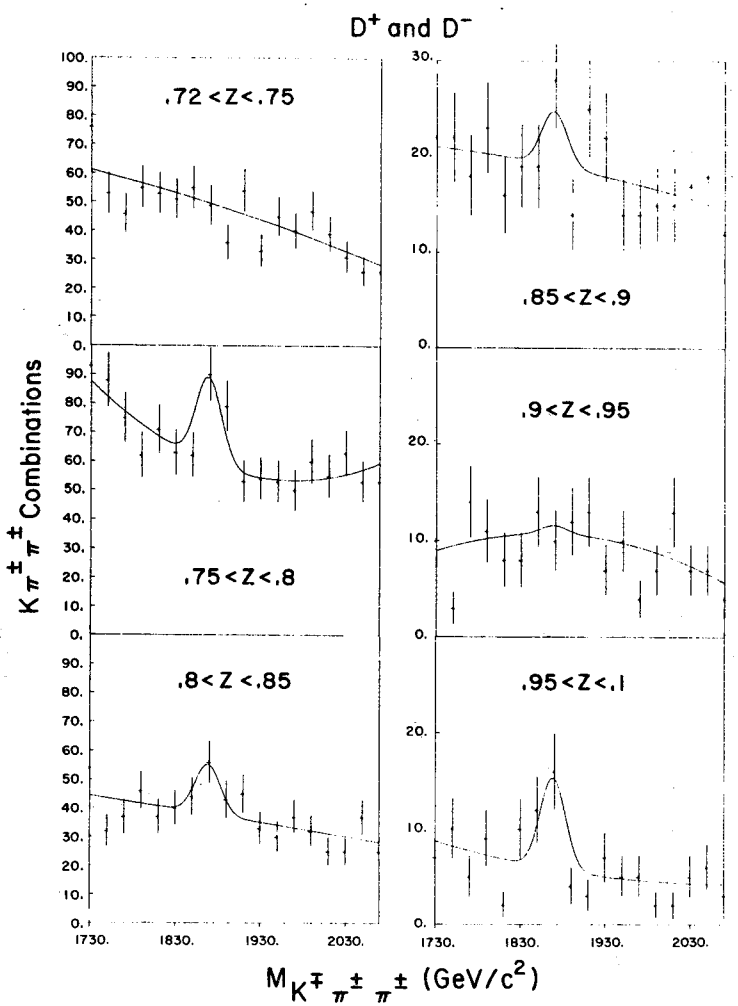

figure 5.5

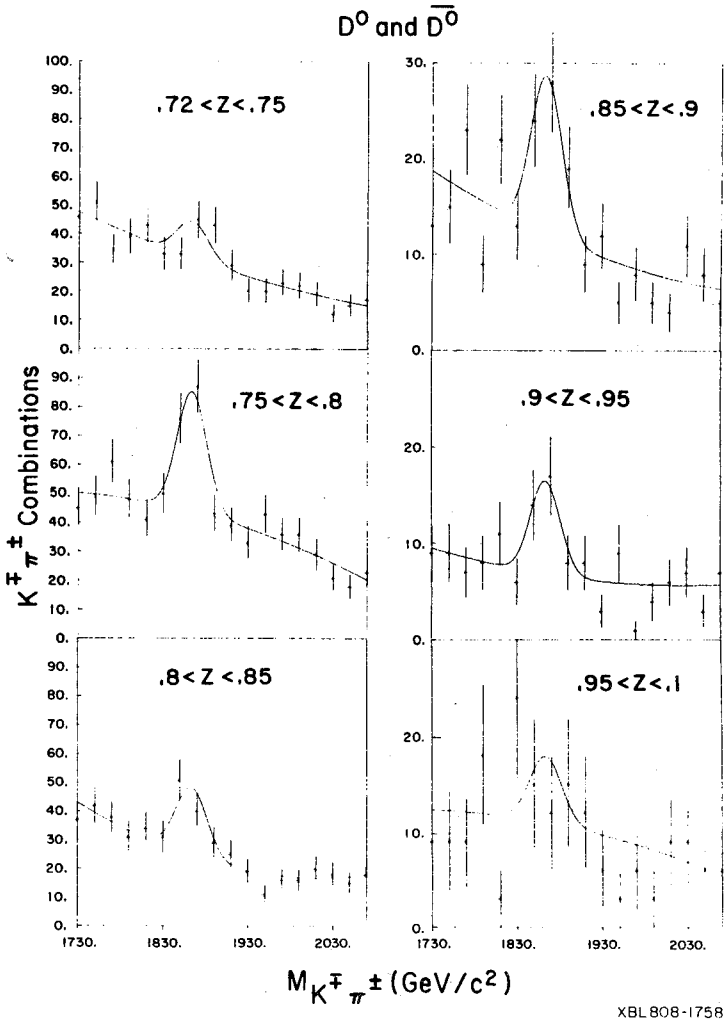

figure 5.4

respectively. The results of the fits are summarized as $S d\sigma/dz$ in figures 5.6a and 5.6b. It is immediately apparent that quasi-two-body D production is not the dominant production mechanism at 5.2 GeV. It is somewhat surprising, however, that there appears to be a larger fraction of charged than neutral quasi-two-body production. Assuming that all D's with a z greater than 0.93 are the result of quasi-two-body production (0.93 would be the z value of a D produced in the reaction

$$e^+e^- \rightarrow D^*\bar{D}^*$$
$$\hookrightarrow D\pi \;)$$

it was determined that $20\pm9\%$ of charged D production was quasi-two-body, while only $9\pm5\%$ of the neutral D production occurred this way. However, this may be just a statistical fluctuation of the large background present underneath the charged D signal in $K\pi\pi$ invariant mass.

Figures 5.6a and 5.6b also rule out the process

$$e^+e^- \rightarrow D\bar{D}\pi$$

as a dominate production mode if the produced particles are distributed according to phase space. Figure 5.7 shows the monte carlo generated phase space distribution for the above process. The shapes of the data and the monte carlo are extremely incompatible. Figure 5.7 shows monte carlo generated events of the type

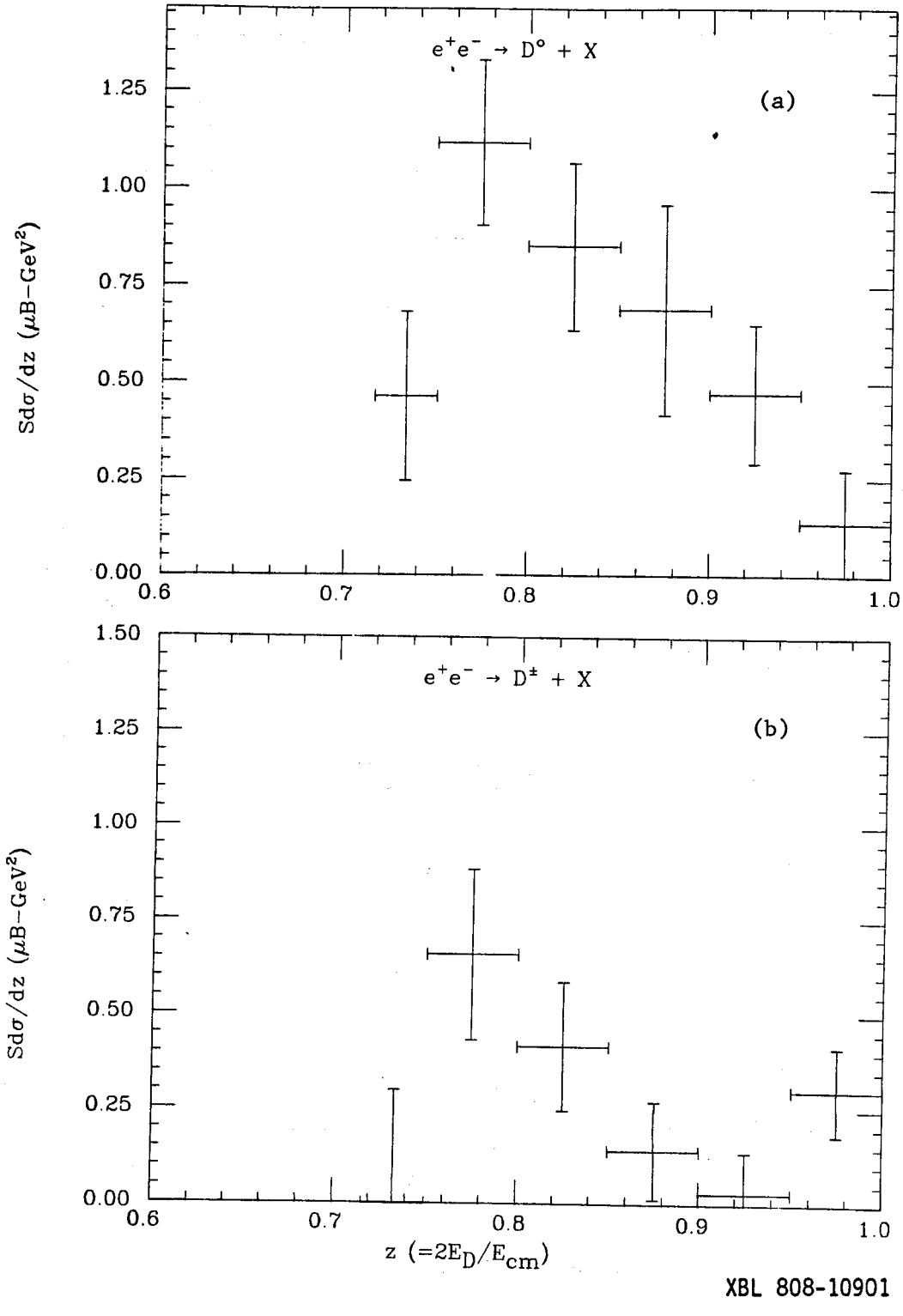
e+e- → D° + X
(a)
1.25
1.00
0.75
0.50
0.25
0.00
0.6
0.7
0.8
0.9
1.0
Sdσ/dz (μB-GeV²)
1.50
e+e- → D± + X
(b)
1.25
1.00
0.75
0.50
0.25
0.00
0.6
0.7
0.8
0.9
1.0
Sdσ/dz (μB-GeV²)
z (=2E_D/E_cm)
XBL 808-10901

figure 5.6

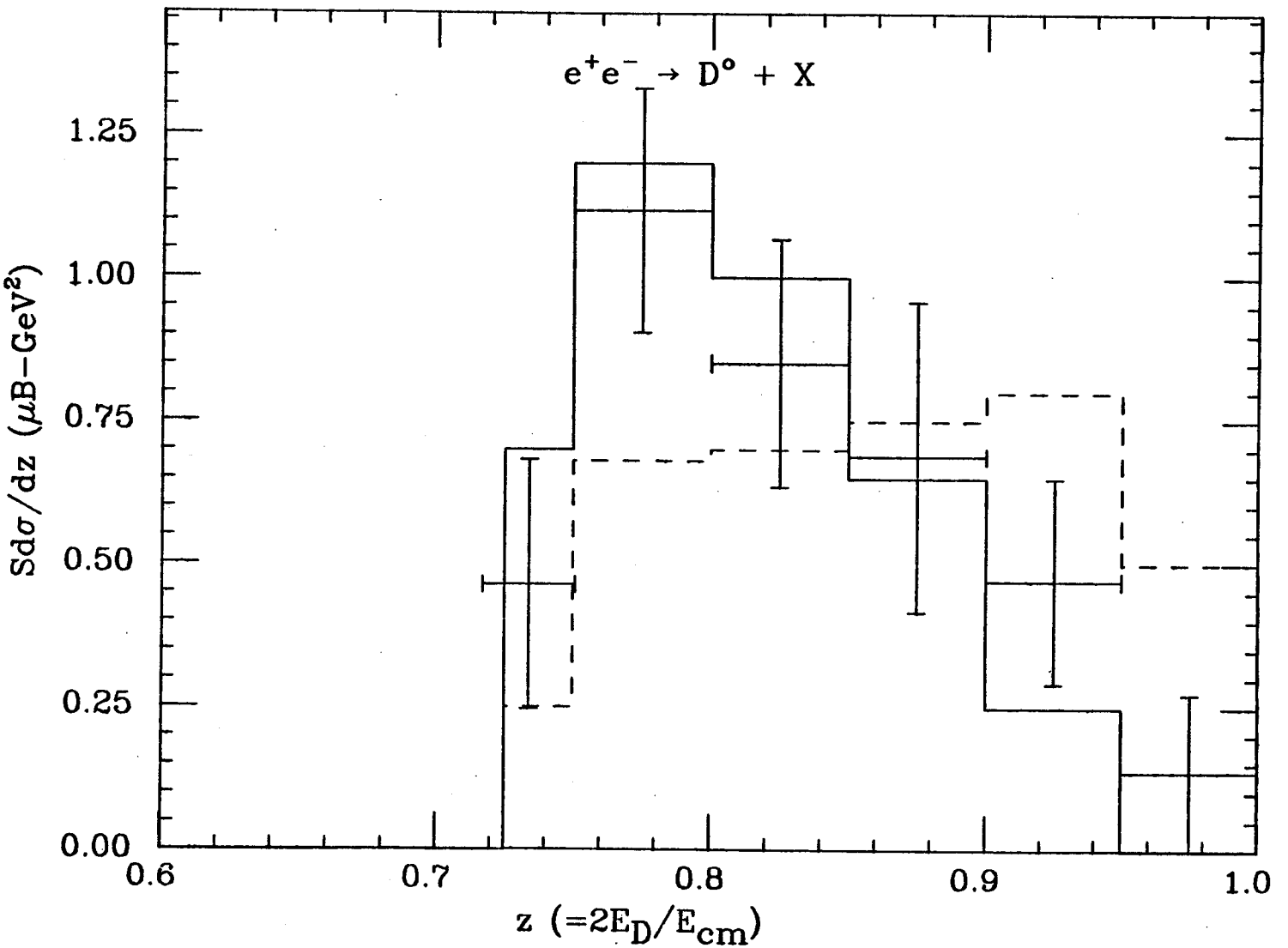

figure 5.7
The dotted line is the prediction of $D\bar{D}\pi$ phase space. The solid line is the prediction of $D\bar{D}\pi\pi$ phase space.

XBL 808-10912

$$e^+e^- \longrightarrow D\bar{D}\pi\bar{\pi}$$

where the D's and π's are distributed according to phase space. The comparison between this distribution and the data is much better, indicating that

$$e^+e^- \longrightarrow D\bar{D} + n\pi\text{'s}$$

with n the average number of additional pions produced and approximately equal to 2, is probably the dominant mode of production.

5.4 The Relationship of the z Distribution of D Mesons at 5.2 GeV to Pion and Kaon Production at Higher Energies

The mechanism through which quarks fragment into hadrons manifests itself in the energy distribution of the hadrons produced by the fragmenting quark. The variable z ($= 2E_D/E_{cm}$) is interpreted as the fraction of the quark's energy given to the hadron.

The quark's decay properties are described by the function $D_i^h(z)$, which is the probability that a quark of type i will fragment into a hadron of type h, carrying a fraction z of the quark's energy. Within this formalism the inclusive differential cross section for D^0 production is

$$S\frac{d\sigma}{dz}(e^+e^- \rightarrow D + X) = \frac{4\alpha^2}{3} e_c^2 D_c^D(z)$$

where $e_c = 2/3$ is the charge of the charmed quark.[41]

It is tempting to parameterize $Sd\sigma/dz$ in terms of one of the

standard suggested forms for $D_i^h(z)$;[42] however these forms are derived for a kinematic region were the mass of the charmed quark should be small relative to the total center of mass energy. In that center of mass energy region, the quantity $Sd\sigma/dz$ should be independent of S and depend on z only. The fact that the Mark II data are at an energy where the charmed quark mass is a substantial fraction of the total center of mass energy makes a comparison of data with theory ambiguous. With due warning as to the validity of the parameterization of $D_c^D(z)$ at this energy as a function of z only, the sum of the charged and neutral D data (excluding the lowest z bin) were fit to the functional form

$$Sd\sigma/dz = A(1-z)^n$$

with the result that $A = 6\pm4$ and $n = 0.9\pm0.4$. The value of n obtained is in agreement with the previous analysis of Piccolo et al.[20] who obtained a value for n of $0.6 \pm .3$ using D mesons produced at 7.8 GeV.

For comparison, the data from figure 5.6a is shown on the same figure as inclusive pion and kaon data in figure 5.8.[43] Apart from the lowest and highest z bins of the D^0 spectrum, the slope of the inclusive D^0 data appears to have approximately the same value as that observed for the pions and kaons.

5.5 The Associated Production of Charmed Mesons and Charmed Baryons

The possibility was investigated that charmed mesons and charmed

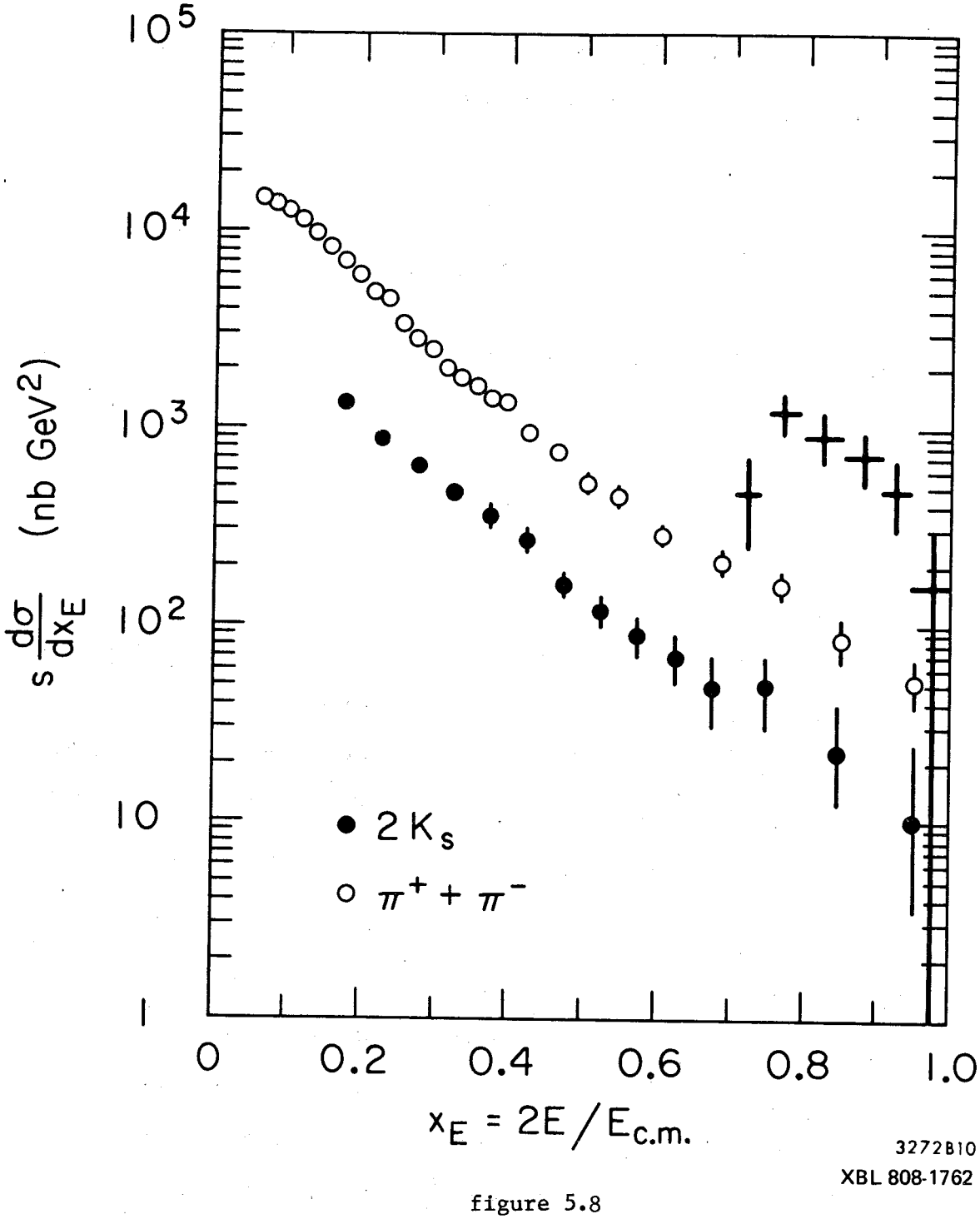

figure 5.8

Comparison of inclusive spectra of charged pions, neutral kaons and neutral D mesons.

baryons may be produced in the same event. At 5.2 GeV, the production must occur in one of two modes:

$$(1) \qquad e^+e^- \rightarrow \Lambda_c \, \bar{D}^0 \, \bar{p}$$

$$(2) \qquad e^+e^- \rightarrow \Lambda_c \, D^- \, \bar{n}$$

Observing a D meson and a proton in the same event at 5.2 GeV would prove the existence of reactions (1) and/or (2), as the threshold for

$$e^+e^- \dashrightarrow p\bar{p}D\bar{D}$$

is about 5.6 GeV.

Two alternate methods were used in an attempt to detect reactions (1) and (2). The first method required the detection of a D and the direct proton, while the second method required the detection of the D and the proton coming from the decay of the charmed baryon.

To employ the first method, the effective mass recoiling against the $\bar{D}^0 \, \bar{p}$ system (or its charge conjugate) was calculated. Only 13 events were seen where a TOF identified proton or anti-proton was found in the same event as a $K\pi$ or $K\pi\pi\pi$ invariant mass combination between 1.82 GeV/c^2 and 1.90 GeV/ c^2 (out of 2140 possible). Of these 13 events , none were observed with a missing mass within 200 MeV/c^2 of the Λ_c mass (2.284 GeV/c^2).[22] If just one event had been found, the cross section for the process would be 0.16 nb. An upper limit for this cross section was calculated using Poisson statistics at the 90% confidence level:

$$\sum_{n=n_0+1} p_m(n) = 0.9$$

where m is the mean number of events expected and n_0 is the number of events observed (=0). Therefore:

$$\sum_{n=n_0+1} p_m(n) = 1 - p_m(0) = 1 - e^{-m} = 0.9$$

which gives a value for m of 2.3. This method indicates that the cross section for associated production of a charmed baryon and a D meson is less than 0.4 nb. at the 90% confidence level.

In the second method for determining the existence of associated D meson and charmed baryon production, events were counted which contained a proton and a $\bar{D}$ or the charge conjugate state of an antiproton and a D. The D was observed through the decay $D \rightarrow K^{\mp}\pi^{\pm}$ or $K^{\mp}\pi^{+}\pi^{\mp}\pi^{+}$ for neutral D's and $D \rightarrow K^{\mp}\pi^{+}\pi^{+}$ for charged D's. Events were labeled as having a D if the invariant mass of the K meson and the pions was greater than 1.82 GeV/c^2 and less than 1.90 GeV/c^2. A background subtraction was made using invariant mass combinations between either 1.65 GeV/c^2 and 1.69 GeV/c^2 or between 2.03 GeV/c^2 and 2.07 GeV/c^2. Events in both the signal and sideband regions of invariant mass were required to have a proton or antiproton (depending on whether a D or $\bar{D}$ was detected) which came from the primary vertex. This selection eliminated protons arising from background sources such as interactions with the residual gas in the beam line or interactions with the vacuum pipe wall.

The analysis found 16 events in the signal region and 17 events

in the sideband regions. Here also, no evidence was found for associated production after background subtraction. This indicated that all proton production was consistent with coming from the background underneath the D signal.

To determine an upper limit on the production cross section, a monte carlo was used to generate events where

$$e^+e^- \rightarrow \Lambda_c^+ \bar{D}^0 \bar{p}, \quad \Lambda_c^+ \rightarrow K^+\pi^-$$

or

$$e^+e^- \rightarrow \Lambda_c^+ \bar{D}^0 \bar{p}, \quad \Lambda_c^+ \rightarrow K^+\pi^-\pi^+\pi^-$$

or

$$e^+e^- \rightarrow \Lambda_c^+ \bar{D} \bar{n}, \quad \Lambda_c^+ \rightarrow K^+\pi^-\pi^-$$

The efficiency for detection of the D alone in such events is given in table 5.3. Since the proton arising from the charmed baryon decay lost energy as it traversed the beam pipe and pipe counter, its detection efficiency was strongly momentum dependent. Below 250 MeV/c the proton was absorbed in the beam pipe or pipe counter and was never visible in the drift chamber. Since the momentum distribution of protons coming from charmed baryon decay was not known, a monte carlo was used to estimate the efficiency for detection using

D Meson Detection Efficiency for Monte Carlo

Events Where $e^+e^- \rightarrow \Lambda_c \bar{D} \bar{p}$

D Decay Mode	Detection Efficiency
$K^{\pm}\pi^{\mp}$	$.40 \pm .01$
$K^{\pm}\pi^{\mp}\pi^{\mp}$	$.22 \pm .01$
$K^{\pm}\pi^{\mp}\pi^{\pm}\pi^{\mp}$	$.08 \pm .01$

Table 5.3

three modes chosen as being representative of charmed baryon decays. Table 5.4 gives these three modes and their effect on the detection efficiency of the proton. If one associated production event had been found, the cross section for this occurrence would be

$$\sigma = \left\{ L(\varepsilon_{K\pi} B_{K\pi} + \varepsilon_{K\pi\pi} B_{K\pi\pi} + \varepsilon_{K\pi\pi\pi} B_{K\pi\pi\pi}) \frac{f_p}{2} \right\}^{-1}$$

where ε_p = detection efficiency of the proton arising from the $_c$ decay

f_p = fraction of $_c$ decays producing protons (estimated as 0.61)[44]

$\varepsilon_{Kn\pi}$ = detection efficiency of the D decay indicated

$B_{Kn\pi}$ = branching fraction for the indicated D decay mode.

The factor of 1/2 comes about because the states $\Lambda_c \bar{D}^0 \bar{p}$ and $\Lambda_c \bar{n} D^-$ are assumed to be produced with equal likelihood. Using table 5.4, the most conservative detection efficiency for the proton (0.49) gives a cross section for the detection of just one real event as 0.05 nb. Since no evidence for such events was found, at the 90% confidence level the cross section is estimated as being less than 0.4 nb, the same limit as obtained from the first method.

These results are comparable to that obtained by measuring the effective recoil mass distribution opposite a Λ_c 22 Approximately 20% of the Λ_c events observed by the Mark II have recoil masses above the D + nucleon threshold. The production cross section obtained by assuming that all of these events are due to production in association with a D meson is 0.34±.08. At the 90% confidence level this

Detection Efficiency of a Proton Coming from

Λ_c Decay in Events where $e^+e^- \rightarrow \Lambda_c\bar{D}$ nucleon

Λ_c Decay Mode	Production Detection Efficiency
$pK\pi$	.65 ± .02
$pK\pi\pi^0$	.49 ± .01
$p\bar{K}^0$	.74 ± .02

Table 5.4

assumption gives an upper limit on associated production of 0.5 nb. in agreement with the limit obtained by the methods described in this chapter.

Chapter 6 Summary and Conclusions

The D meson production cross section has been measured at center of mass energies between 3.88 GeV and 7.4 GeV. The quantity R_D ($[\sigma_{D^+D^-} + \sigma_{D^0+\bar{D}^0}]/2\sigma_{\mu^+\mu^-}$) was shown to explain the structure in R ($\sigma_{hadronic}/\sigma_{\mu^+\mu^-}$) observed near 4 GeV. By adding the value of R measured below 3 GeV to R_D, good agreement at all center of mass energies was found between R_D and the R values reported by the Mark II, DASP, and PLUTO collaborations. The DELCO measurement of R_c (the part of R due to charm quark production) is also in agreement with R_D.

The energy dependences of the quasi-two-body production cross sections $\sigma_{D\bar{D}}$, $\sigma_{D^*\bar{D}}$, and $\sigma_{D^*\bar{D}^*}$ were measured between 3.88 GeV and 4.3 GeV. The cross sections were obtained by fitting the experimentally observed recoil effective mass distribution opposite a D to a theoretical expression which describes quasi-two-body production. The fit was done in two ways. Each fit determined the branching fractions for charged and neutral D* decay into a D and either a photon or a pion.

Both methods gave results in good agreement with the potential model of Eichten et al.,[29] especially for the energy dependences of $\sigma_{D\bar{D}}$ and $\sigma_{D^*\bar{D}}$. $\sigma_{D^*\bar{D}^*}$ and $\sigma_{D^*\bar{D}}$ were found to peak at just above 4 GeV and decrease with increasing energy up to 4.3 GeV. The sum of the three quasi-two-body cross sections was also found to be in good

agreement with the cross section determined from inclusive measurements and used in calculating R_D.

Branching fractions for D* decay were found to be in good agreement with the results of the Mark I experiment. The branching fraction for $D^{*0} \rightarrow D^0\pi^0$ was measured to be (averaging the isotropic and anisotropic fits) $0.49 \pm .10$, in agreement with the Mark I result of $0.55 \pm .15$. The branching ratio for $D^{*+} \rightarrow D^0\pi^+$ was measured to be $0.44 \pm .07$, in approximate agreement with the Mark I result of $0.60 \pm .15$. In addition, the previously unreported branching fraction for $D^* \rightarrow D^+\pi^0$ was determined to be $0.31 \pm .07$. Therefore the D^{*+} radiative decay branching ratio is $0.25 \pm .10$.

Some evidence was found that there are more charged tracks produced in events which contain a D at 5.2 GeV than at 3.77 GeV (where D production is entirely $D\bar{D}$). This suggests a reaction of the form $e^+e^- \rightarrow D\bar{D} + n\pi$'s. The quantity $Sd\sigma/dz$ was measured at 5.2 GeV and found to support the hypothesis that additional pions are produced in association with D's. The measured distribution agrees well with what one would observe in the reaction $e^+e^- \rightarrow D\bar{D}\pi\pi$, where the D's and π's are distributed according to phase space. The measured distribution also excludes the reaction $e^+e^- \rightarrow D\bar{D}\pi$ in a phase space distribution as the dominant production mode. Quasi-two-body production was found to be a very small fraction of the total cross section at 5.2 GeV. Less than $20 \pm 9\%$ of the charged D production, and less than $9 \pm 5\%$ of the neutral D production occurred in this way.

A fit of $Sd\sigma/dz$ to the function $A(1-z)^n$ gave $A = 4 \pm 3$ and $n = 0.9 \pm 0.4$. The value for n is in agreement with similar values

obtained in fitting the K_s and charged pion distributions at large z.

No evidence was found for the existence of associated charmed baryon and D meson production at 5.2 GeV. The production cross section for associated production was determined to be less than 0.4 nb. at the 90% confidence level.

REFERENCES

1. Applequist, Lane, and Barnett, Ann. Rev. Nucl. Sci. 28, 387 [1978].

2. Goldhaber and Wiss, LBL-10652, March [1980], submitted to Ann. Rev. of Nucl. and Part. Sci.

3. J. D. Bjorken and S. L. Glashow, Phys. Lett. 11, 225 [1965].

4. S. Okubo, Phys. Lett. 5, 165 [1963]; G. Zweig, CERN TH401, CERN TH412, CERN, Geneva, Switzerland; J. Iizuka, Suppl. Prog. Theor. Phys. 21, 37 [1966].

5. S. L. Glashow, J. Iliopoulos, and L. Maiani, Phys. Rev. D2, 1285 [1970].

6. M. K. Gaillard, B. W. Lee, and J. Rosner, Rev. Mod. Phys. 47, 277 [1975].

7. G. Goldhaber et al., Phys. Rev. Lett. 37, 255 [1976]; I. Peruzzi et al., Phys. Rev. Lett. 37, 569 [1976].

8. G. J. Feldman et al., Phys. Lett. 69B, 5013 [1977].

9. H. K. Nguyen et al., Phys. Rev. Lett. 39, 262 [1977].

10. I. Peruzzi et al., Phys. Rev. Lett. 39, 1301 [1977].

11. T. Applequist and H. Politzer, Phys. Rev. Lett. 34, 43 [1975], Phys. Rev. D12, 1404 [1975]; also A. Dekujula and S. L. Glashow, Phys. Rev. Lett. 34, 46 [1975].

12. J. E. Wiss, Ph.D. thesis, LBL-6725 [1977].

13. W. Davies-White et al., Nucl. Instrum. Methods, 160, 227 [1979].

14. G. S. Abrams et al., IEEE Trans. Nucl. Sci. NS-25, 309 [1978]; and G. S. Abrams et al., IEEE Trans. Nucl. Sci. NS-27, 59 [1980].

15. C. A. Blocker, Ph.D. thesis LBL-10801 [1980].

16. M. Breidenbach, SLAC-PUB-2032 [1977] and SLAC-PUB-2033 [1977].

17. R. Schindler, SLAC-PUB-219, Ph.D. thesis, [1979].

18. G. Trilling and D. Johnson, LBL Internal Memo TG-301 [1978].

19. The first evidence that counting spin states gave an erroneous prediction was observed by G. Goldhaber et al., Phys. Lett. 69B, 503 [1977].

20. M. Piccolo et al., Phys. Lett. 86B, 220 [1979], P. A. Rapidis et al., Phys. Lett. 84B, 507 [1979].

21. P. A. Rapidis et al., Phys. Lett. 84B, 507 [1979]; J. L. Siegrist, Ph.D. thesis, SLAC-225 [1979].

22. G. S. Abrams et al., Phys. Rev. Lett. 44, 10 [1980].

23. J. L. Siegrist, SLAC-225 p. 127 [1979].

24. Experimentally, the Mark II result is that charmed baryon production contributes only about one third of a unit to R (see ref. 22).

25. Burmester et al., Phys. Lett. 66B, 395 [1977].

26. Brandelik et al., Phys. Lett. 76B, 361 [1978].

27. J. Kirkby, SLAC Summer Institute 1978, SLAC-215, p.313.

28. Eichten et al., Phys. Rev. D, 21, 203 [1980]; Kogerler and Chaichan, Annals of Physics 124, 61 [1980]; E. Eichten, Phys. Rev. Lett. 37, 477 [1976]; and K. Gottfried, CLNS-376 [Nov. 1977], presented at the 1977 Symposium on Lepton and Photon Interactions at High Energies, Hamburg.

29. Eichten et al., Phys. Rev. D, 21, 203 [1980].

30. See Quigg and Rosner, Phys. Lett. 71B, 153 [1977] for a

discussion of logarithmic potentials; also Machacek and Tomozawa, Ann. Phys. (NY) 110, 407 [1978]).

31. K. D. Lane and E. Eichten, Phys. Rev. Lett 37, 477 [1976]; E. Eichten in "Weak and Electromagnetic Interactions at High Energies," proceedings of the NATO Advanced Study Institute, Cargese, 1975, edited by M. Levy, J.-L. Basderant, D. Speiser, and R. Gastmans, (Plenum, NY, 1976), Part A.

32. M. K. Gaillard, B. W. Lee, and J. L. Rosner, Rev. Mod. Phys. 42, 277 [1973], A. DeRujula, H. Georgi, and S. L. Glashow, Phys. Rev. Lett. 37, 398 [1976]; B. W. Lee, C. Quigg, and J. L. Rosner, Phys. Rev. D 15, 157 [1977].

33. P. Rapidis, Ph.D. thesis, SLAC-220 [1979].

34. R. Cahn, LBL-10692 (April 1980), submitted to Phys. Rev. D.; the assistance of Philippe DeForcrand in checking the calculations is gratefully acknowledged.

35. Wiss, J. E. et al., Phys. Rev. Lett. 37, 1531 [1976].

36. P. James and M. Roos, CERN D506, D516, [1974].

37. F. E. Close, Phys. Lett. 65, 55 [1976].

38. S. Ono, Phys. Rev. Lett. 37, 655 [1976].

39. A. Bohm and R. B. Teese, Phys. Rev. Lett. 38, 629 [1977].

40. J. L. Rosner J. L., Orbis Scientiae (1977), Coral Gables, and Phys. Rev. D 17, 239 [1978]; see also Schindler, ref. 17, for a description of the monte carlo which implemented the statistical isospin model.

41. R. Field and R. Feynman, Phys. Rev. D15, 2590 [1977].

42. L. Sehgal and P. Zerwas, Nucl. Phys. B108, 483 [1976], A.

Seiden, Phys. Lett. 68B, 157 [1977]; H. Gronan et al., Nucl. Phys. B123, 47 [1977]; R. Field and R. Feynman, Nucl. Phys. B136, 1 [1978]; S. Ellis et al., Nucl. Phys. B108, 93 [1976]; V. Kartvelishvili et al., Phys. Lett. 78B, 615 [1978].

43. V. Luth et al., Phys. Lett. 70B, 120 [1977]; G. Hanson et al., Phys. Rev. Lett., 35, 1609 [1975]; G. Hanson in Proceedings of the XVIII Int. Conf. on High Energy Physics, Tbilisi, U.S.S.R., [1976], p. B1.

44. This assumption is based on an isospin statistical model due to Gary Feldman. See also Peshkin and Rosner, Nucl. Phys. B122, 144 (1977).